ORNL/TM-5613

Prestressed Concrete Reactor Vessel Thermal Cylinder Model Study

J. P. Callahan
D. A. Canonico
M. Richardson
J. M. Corum
W. G. Dodge
G. C. Robinson
G. D. Whitman

MASTER

OAK RIDGE NATIONAL LABORATORY

OPERATED BY UNION CARBIDE CORPORATION FOR THE ENERGY RESEARCH AND DEVELOPMENT ADMINISTRATION

DISCLAIMER

This report was prepared as an account of work sponsored by an agency of the United States Government. Neither the United States Government nor any agency Thereof, nor any of their employees, makes any warranty, express or implied, or assumes any legal liability or responsibility for the accuracy, completeness, or usefulness of any information, apparatus, product, or process disclosed, or represents that its use would not infringe privately owned rights. Reference herein to any specific commercial product, process, or service by trade name, trademark, manufacturer, or otherwise does not necessarily constitute or imply its endorsement, recommendation, or favoring by the United States Government or any agency thereof. The views and opinions of authors expressed herein do not necessarily state or reflect those of the United States Government or any agency thereof.

DISCLAIMER

Portions of this document may be illegible in electronic image products. Images are produced from the best available original document.
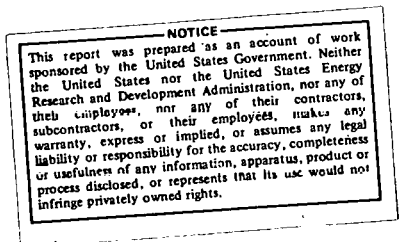
HTGR BASE TECHNOLOGY PROGRAM

Prestressed Concrete Nuclear Pressure
Vessel Development (189a. No. 01331)

PRESTRESSED CONCRETE REACTOR VESSEL
THERMAL CYLINDER MODEL STUDY

J. P. Callahan   J. M. Corum
D. A. Canonico   W. G. Dodge
M. Richardson   G. C. Robinson
        G. D. Whitman

MASTER

THIS PAGE

WAS INTENTIONALLY

LEFT BLANK

CONTENTS

ACKNOWLEDGMENTS

PRESTRESSED CONCRETE REACTOR VESSEL
THERMAL CYLINDER MODEL STUDY

J. P. Callahan   J. M. Corum
D. A. Canonico   W. G. Dodge
M. Richardson   G. C. Robinson
G. D. Whitman

ABSTRACT

The thermal cylinder experiment was designed both to pro-
vide information for evaluating the capability of analytical
methods to predict the time-dependent stress-strain behavior
of a 1/6-scale model of the barrel section of a single-cavity
prestressed concrete reactor vessel and to demonstrate the
structural behavior under design and off-design thermal con-
ditions. The model was a thick-walled cylinder having a height
of 1.22 m, a thickness of 0.46 m, and an outer diameter of 2.06
m. It was prestressed both axially and circumferentially and
subjected to 4.83 MPa internal pressure together with a thermal
crossfall imposed by heating the inner surface to 338.8 K and
cooling the outer surface to 297.1 K. Since the model was de-
signed to study the behavior of the barrel section of a massive
concrete structure, all exposed surfaces were sealed to prevent
loss of moisture, and the ends of the cylinder were insulated
to prevent heat flow in the axial direction.

The experiment utilized information developed from previous
studies of concrete materials properties, triaxial creep, in-
strumentation, analysis methods, and structural models. The
initial 460 days of testing were divided into time periods that
simulated prestressing, heatup, reactor operation, and shutdown.
At the conclusion of the simulated operating period, the model
was repressurized and subjected to localized heating at 505.4 K
for 84 days to produce an off-design hot-spot condition.

Postmortem examinations revealed corrosion of axial pre-
stressing tendons, with a number of tendons having failed. The
corrosion was apparently caused by the development of an environ-
ment in the tendon ducts that was unique to this experiment.

Comparisons of experimental data with calculated values ob-
tained using the SAFE-CRACK finite-element computer program
showed that the program was capable of predicting time-dependent
behavior in a vessel subjected to normal operating conditions,
but that it was unable to accurately predict the behavior during
off-design hot-spot heating. Readings made using a neutron and
gamma-ray backscattering moisture probe showed little, if any,
migration of moisture in the concrete cross section. Destruc-
tive examination indicated that the model maintained its basic
structural integrity during localized hot-spot heating.

1. INTRODUCTION

Prestressed concrete reactor vessels (PCRVs) are unique with respect
to concrete technology primarily because of the elevated operating tempera-
tures employed. In the ORNL Prestressed Concrete Reactor Vessel Research
and Development Program,[1] analytical methods have been developed and basic
test data obtained for time-dependent deformation behavior of concrete.
By incorporating these data into an appropriate analysis, predictions of
time-dependent behavior of PCRVs can be made. Thus far, however, there
have been limited means for assessing the accuracy of such analytical pre-
dictions. The thermal cylinder test is designed to provide the kind of
information needed to make such an assessment.

The thermal cylinder is an approximately 1/6-scale model of the middle,
or barrel, section of the cylindrical portion of a prestressed concrete
reactor vessel, as shown in Fig. 1.1, which was subjected to the simulated
in-service operating conditions shown diagrammatically in Fig. 1.2. The
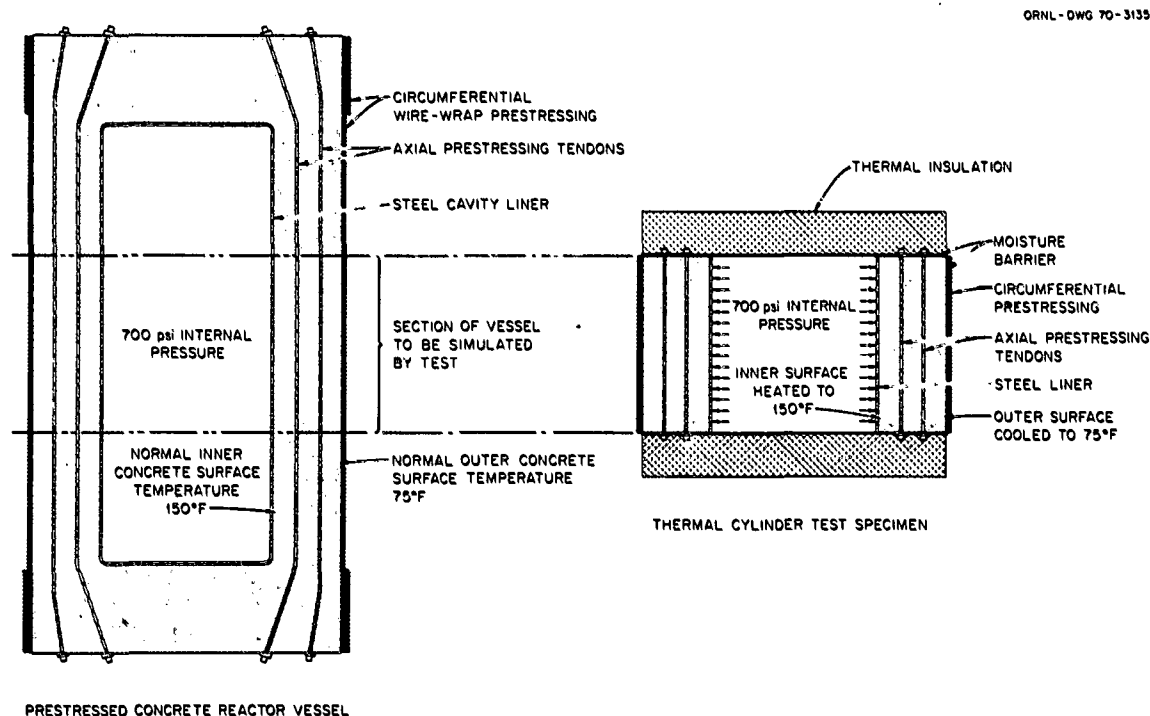
Fig. 1.1. Relationship of thermal cylinder test model to prestressed
concrete reactor vessel [1 psi = 6895 Pa; K = 273.15 + 5/9 (°F − 32)].
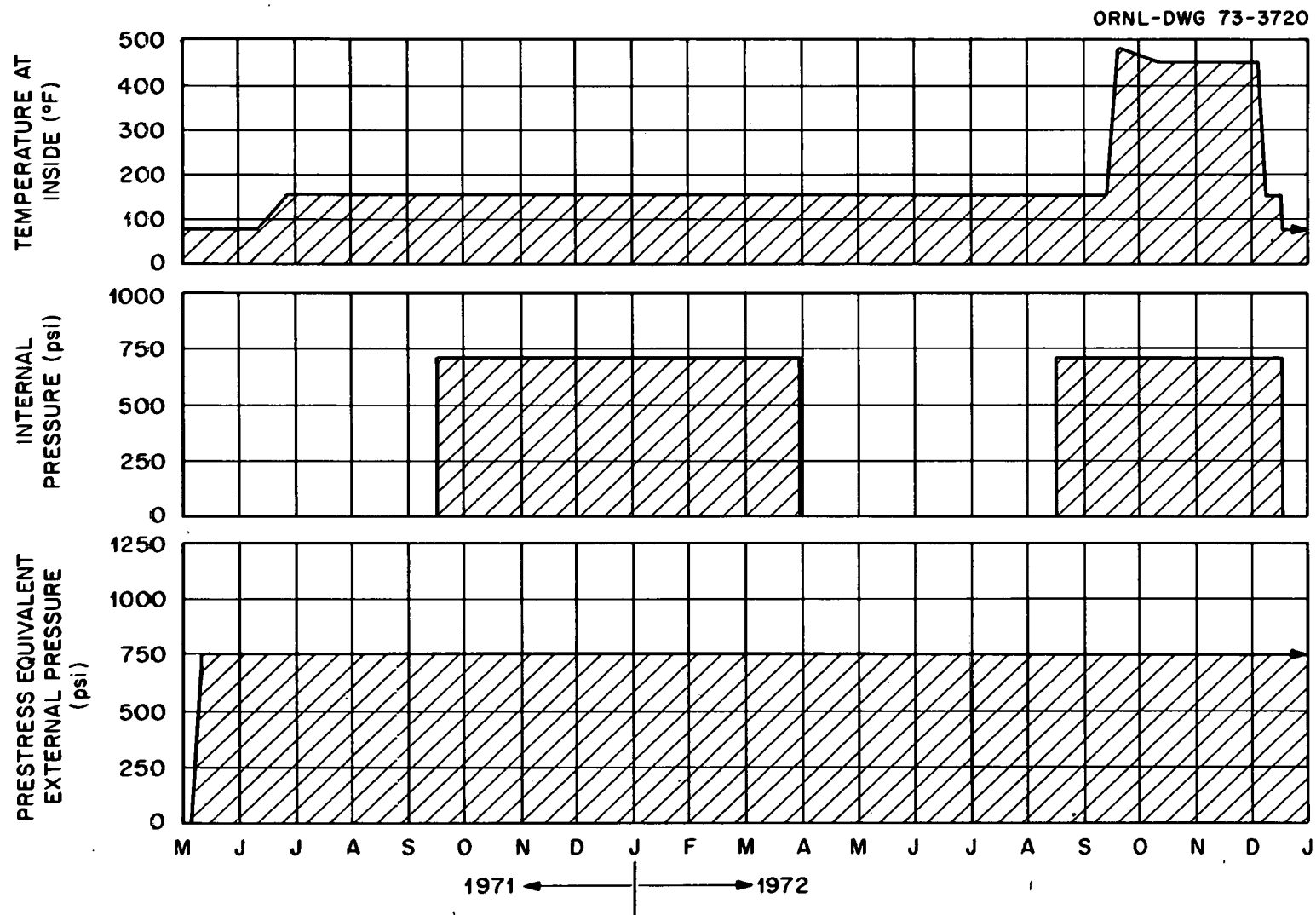
Fig. 1.2. Temperature and loading history of the thermal cylinder
[1 psi = 6895 Pa; K = 273.15 + 5/9 (°F − 32)].

test structure, described in detail in Refs. 2 and 3, is a thick-walled cylinder having a height of 1.22 m, a thickness of 0.46 m, and an outer diameter of 2.06 m.

The prestressing arrangement is shown in Fig. 1.3. There were 52 axial tendons arranged in two rows of 26 tendons each. The S.E.E. anchor system was used with the axial tendons. A unique arrangement was employed for the circumferential prestressing; monostrand tendons were wrapped around the outer surface of the cylinder and posttensioned by jacking them outwardly, as shown in Fig. 1.3. The axial and circumferential tendons
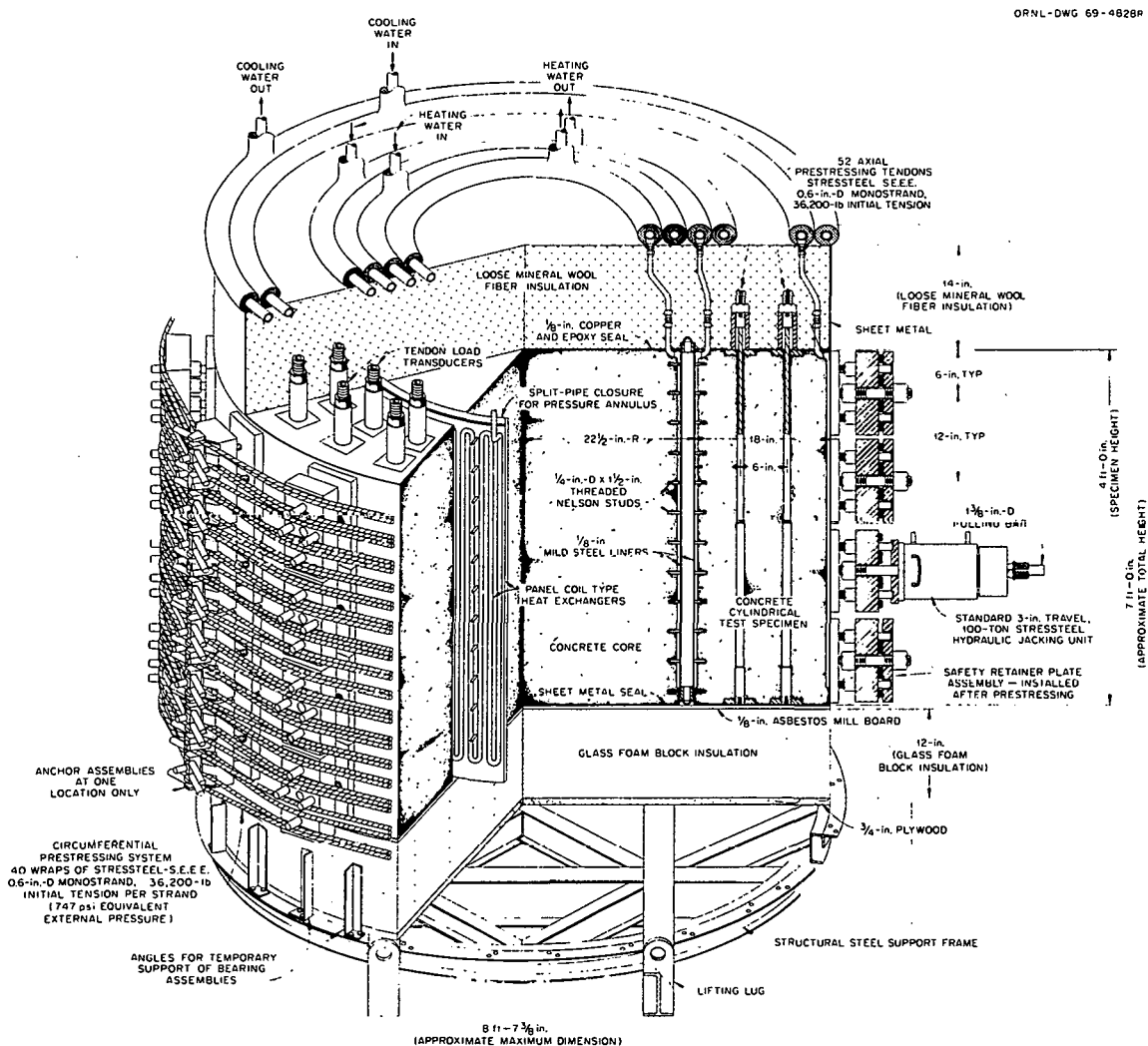
Fig. 1.3. Isometric drawing of the thermal cylinder test structure (1 in. = 25.4 mm; 1 ft = 0.305 m). Initial tension per strand is 0.161 MN (36,200 lb), equivalent to 5.15-MPa (747-psi) external pressure.

consisted of seven-wire strands manufactured in accordance with ASTM A416. LOK-STRESS strand was specified to reduce relaxation losses. The strand had a nominal diameter of 1.54 cm, a breaking strength of 24,500 kg, and a nominal steel area of 1.39 cm^2. The approximate modulus of elasticity was 193 GPa.

All surfaces of the model were sealed to prevent any moisture loss, and the ends were insulated thermally to limit heat flow to the radial direction. The model was prestressed (in practice, it was actually post-tensioned) axially and circumferentially, and a 4.83-MPa internal pressure was applied through a pressurizing annulus, as shown in Fig. 1.3. The inner cavity of the cylinder contained a concrete core, which provided the inner support for the relatively thin pressurizing annulus. Since pressurization of the annulus induced a purely biaxial stress state in the core, the behavior of this region, as well as the outer test ring, provided basic information on the behavior of both the concrete and the instrumentation. The model was highly instrumented, and, in addition to providing experimental data on structural behavior, it also provided an opportunity to evelute instrument performance under conditions simulating PCRV design and off-design conditions.

A thermal gradient was imposed by heating the inner surface of the cylinder to 338.7 K and cooling the outer surface to 279.0 K to represent normal PCRV operation. During a subsequent period, a narrow circumferential band on the inner surface of the test section was heated to 505.4 K and maintained at that temperature for a period of 84 days. This second phase of the test simulated an off-design hot-spot condition in which the cooling and/or the insulation is assumed to have failed in an operating nuclear reactor.

The overall study was divided into the following phases:

1. instrumentation calibration,
2. assembly and casting of model and companion specimens,
3. model testing,
4. analytical studies,
5. comparison of experimental and analytical results,
6. postmortem studies

Each phase is discussed in the following sections.

2. INSTRUMENTATION

2.1 Stress and Strain Gages

Complete data sets were recorded during each experimental event, using the 155 gages listed in Table 2.1. The instrumentation consisted of embedment gages cast directly into the concrete and more conventional types of resistance strain gages attached to the liner and prestressing tendons. The radial positions of the various embedment gages are shown in Fig. 2.1. Generally, the initial letter of the gage designations used in the figure and listed in Table 2.1 indicates the quadrant of the model in which the gage is located (A, B, C, or D), and this is followed by one or two letters or a letter and a number designating the gage type. The first number of the three-number series that follows the letters indicates relative radial position from the inside of the test section; the last number indicates the orientation (i.e., 1 = axial, 2 = radial, and 3 = circumferential); and the middle number is used to further identify individual sensors. Information on the operability of the gages before the hot-spot test and at the end of the experiment is also provided in Table 2.1.

A total of 12 of the 52 axial prestressing tendons were instrumented with bonded electrical resistance strain gages and load-calibrated in a tensile testing machine. In addition, 12 load cells that were designed and fabricated for use with the instrumented axial tendons were load-calibrated in compression. The locations of the instrumented tendons on the model are shown in Fig. 2.2 relative to A, B, C, and D quadrants. This combination of instrumented tendons and load transducers was used to determine the relationship between the initial stress developed during posttensioning of the tendons and the actual load transferred to the structure. In addition, it provided a means for monitoring possible creep and stress relaxation of the tendons. Strains in the circumferential tendons were monitored using strain gages that were bonded to 8 of the 16 circumferential tendons shown in Fig. 2.2. In the case of the circumferential tendons, no practical way was found to include load cells.

Table 2.1. Thermal cylinder instrumentation

Type of gage	Cylinder quadrant	Gage No.	Orientation	Status before hot-spot test	Final status
		Embedment strain gages			
Single-filament resistance	A	EB-131	Axial	Operative	Operative
	A	EB-231	Axial	Operative	Operative
	A	EB-351	Axial	Operative	Operative
	A	EB-132	Radial	Inoperative	Inoperative
	A	EB-232	Radial	Operative	Operative
	A	EB-352	Radial	Operative	Operative
	A	EB-133	Circumferential	Inoperative	Inoperative
	A	EB-233	Circumferential	Operative	Operative
	A	EB-353	Circumferential	Operative	Inoperative
	B	EB-151	Axial	Operative	Operative
	B	EB-251	Axial	Operative	Operative
	B	EB-351	Axial	Operative	Operative
	B	EB-152	Radial	Operative	Operative
	B	EB-252	Radial	Operative	Operative
	B	EB-153	Circumferential	Operative	Inoperative
	B	EB-253	Circumferential	Operative	Operative
	B	EB-353	Circumferential	Operative	Operative
	C	EB-151	Axial	Operative	Operative
	C	EB-241	Axial	Operative	Operative
	C	EB-341	Axial	Operative	Operative
	C	EB-152	Radial	Operative	Inoperative
	C	EB-242	Radial	Inoperative	Inoperative
	C	EB-342	Radial	Operative	Operative
	C	EB-153	Circumferential	Operative	Inoperative
	C	EB-243	Circumferential	Operative	Operative
	C	EB-343	Circumferential	Operative	Operative
	C (core)	EB-141	Axial	Operative	Inoperative
	C (core)	EB-251	Axial	Operative	Inoperative
	C (core)	EB-341	Axial	Operative	Inoperative
	C (core)	EB-342	Radial	Operative	Inoperative
	C (core)	EB-143	Circumferential	Operative	Inoperative
	C (core)	EB-253	Circumferential	Operative	Inoperative
	D	EB-151	Axial	Operative	Operative
	D	EB-251	Axial	Operative	Operative
	D	EB-341	Axial	Operative	Operative
	D	EB-152	Radial	Operative	Operative
	D	EB-252	Radial	Inoperative	Inoperative
	D	EB-342	Radial	Operative	Operative
	D	EB-153	Circumferential	Operative	Inoperative
	D	EB-253	Circumferential	Operative	Operative
	D	EB-343	Circumferential	Operative	Operative
	D (hot spot)	HS-1-13-1	Axial	Inoperative	Inoperative
	D (hot spot)	HS-2-10-1	Axial	Inoperative	Inoperative
	D (hot spot)	HS-1-12-2	Radial	Operative	Operative
	D (hot spot)	HS-2-11-2	Radial	Inoperative	Inoperative
	D (hot spot)	HS-1-15-3	Circumferential	Operative	Operative
	D (hot spot)	HS-2-11-3	Circumferential	Inoperative	Inoperative
Vibrating wire (type A)	B	D6-101	Axial	Inoperative	Inoperative
	B	D6-102	Radial	Inoperative	Inoperative
	B	D9-103	Circumferential	Inoperative	Inoperative
	C	D9-101	Axial	Inoperative	Inoperative
	C	D9-201	Axial	Operative	Operative
	C	D9-301	Axial	Inoperative[a]	Inoperative
	C	D9-401	Axial	Inoperative[a]	Inoperative
	C	D9-102	Radial	Inoperative	Inoperative

Table 2.1 (continued)

Type of gage	Cylinder quadrant		Gage No.	Orientation	Status before hot-spot test	Final status
		Embedment strain gages (continued)				
Vibrating wire (type A)	C		D6-202	Radial	Operative	Inoperative
(continued)	C	·	D6-302	Radial	Operative	Operative
	C		D6-402	Radial	Operative	Operative
	C		D9-103	Circumferential	Inoperative	Inoperative
	C		D9-203	Circumferential	Inoperative	Inoperative
	C		D9-303	Circumferential	Operative	O;-rative
	C		D9-403	Circumferential	Inoperative[a]	Inoperative
	D		D9-101	Axial	Inoperative	Inoperative
	D	·	D9-201	Axial	Inoperative	Inoperative
	D		D9-301	Axial	Operative[a]	Operative
	D		D9-401	Axial	Inoperative[a]	Inoperative
	D		D6-102	Radial	Inoperative[a]	Inoperative
	D		D6-202	Radial	Inoperative[a]	Inoperative
	D	·	D6-302	Radial	Inoperative[a]	Inoperative
	D		D6-402	Radial	Inoperative[a]	Inoperative
	D		D9-103	Circumferential	Inoperative	Inoperative
	D		D9-203	Circumferential	Inoperative[a]	Inoperative
	D		D9-303	Circumferential	Inoperative[a]	Inoperative
	D		D9-403	Circumferential	Operative	Operative
Vibrating wire (type B)	A		P-101	Axial	Operative	Inoperative
	A		P-201	Axial	Operative	Operative
	A		P-301	Axial	Operative	Operative
	A		P-102	Radial	Operative	Inoperative
	A		P-202	Radial	Operative	Operative
	A		P-302	Radial	Operative	Operative
	A		P-103	Circumferential	Inoperative	Inoperative
	A		P-203	Circumferential	Operative	Operative
	A		P-303	Circumferential	Operative	Operative
Vibrating wire (type C)	G		GGA-202	Radial	Inoperative	Inoperative
Wound-wire resistance	C		K-301	Axial	Operative	Operative
	C		K-302	Radial	Operative	Operative
	C		K-303	Circumferential	Inoperative[a]	Inoperative
	C (core)		K-101	Axial	Operative	Operative
	C (core)		K-102	Radial	Operative	Operative
	C (core)		K-103	Circumferential	Operative	Operative
		Embedment stress cells				
Titanium resistance	C		T-141	Axial	Inoperative	Inoperative
	C		T-271	Axial	Operative	Operative
	C		T-3-15-1	Axial	Inoperative	Inoperative
	C		T-4-13-1	Axial	Inoperative[a]	Inoperative
	C		T-163	Circumferential	Operative	Operative
	C		T-253	Circumferential	Operative	Operative
	C		T-3-12-3	Circumferential	Operative	Operative
	C		T-4-11-3	Circumferential	Operative	Operative
Pressure diaphragm	A		PSC-111	Axial	Inoperative	Inoperative
	A		PSC-241	Axial	Inoperative	Inoperative
	A		PSC-341	Axial	Inoperative	Inoperative
	A		PSC-143	Circumferential	Inoperative	Inoperative
	A		PSC-253	Circumferential	Inoperative	Inoperative
	A		PSC-353	Circumferential	Inoperative	Inoperative
		Strain gages welded to B heat exchanger				
Weldable resistance	A		1	Axial	Operative	Operative
	A	·	2	Circumferential	Operative	Operative
	A		5	Axial	Operative	Operative

Table 2.1 (continued)

Type of gage	Cylinder quadrant	Gage No.	Orientation	Status before hot-spot test	Final status
Strain gages welded to B heat exchanger (continued)					
Weldable resistance (continued)	A	6	Circumferential	Inoperative	Inoperative
	B	1	Axial	Inoperative	Inoperative
	B	2	Circumferential	Inoperative	Operative
	B	5	Axial	Operative	Operative
	B	6	Circumferential	Inoperative	Inoperative
	C	1	Axial	Inoperative	Inoperative
	C	2	Circumferential	Inoperative	Operative
	C	5	Axial	Operative	Operative
	C	6	Circumferential	Operative	Operative
	D	1	Axial	Operative	Operative
	D	2	Circumferential	Operative	Operative
	D	5	Axial	Operative	Operative
	D	6	Circumferential	Operative	Operative
	D (hot spot)	HS-1	Axial	Inoperative	Inoperative
	D (hot spot)	HS-2	Circumferential	Inoperative	Inoperative
	D (hot spot)	HS-5	Axial	Operative	Operative
Strain gages bonded to axial prestressing tendons					
Bonded foil	A	CB-11A	Axial	Inoperative	Operative
	A	CB-12A	Axial	Inoperative	Operative
	B	CB-5A	Axial	Inoperative	Inoperative
	B	CB-6A	Axial	Inoperative	Operative
	C	CB-1A	Axial	Inoperative	Operative
	C	CB-2A	Axial	Operative	Operative
	C	CB-3A	Axial	Inoperative	Inoperative
	C	CB-4A	Axial	Operative	Operative
	D	CB-7A	Axial	Inoperative	Inoperative
	D	CB-8A	Axial	Operative	Operative
	D	CB-9A	Axial	Inoperative	Operative
	D	CB-10A	Axial	Operative	Operative
Load cells on axial prestressing tendons					
Stress transducer	A	TR-11	Axial	Inoperative	Operative
	A	TR-12	Axial	Operative	Operative
	B	TR-5	Axial	Inoperative	Operative
	B	TR-6	Axial	Operative	Operative
	C	TR-1	Axial	Inoperative	Inoperative
	C	TR-2	Axial	Operative	Operative
	C	TR-3	Axial	Inoperative	Operative
	C	TR-4	Axial	Operative	Operative
	D	TR-7	Axial	Operative	Operative
	D	TR-8	Axial	Operative	Operative
	D	TR-9	Axial	Operative	Operative
	D	TR-10	Axial	Operative	Operative
Strain gages bonded to circumferential prestressing tendons					
Bonded foil	B	CGA-1	Circumferential	Operative	Operative
	B	CGA-2	Circumferential	Operative	Operative
	B	CGB-1	Circumferential	Operative	Operative
	B	CGB-2	Circumferential	Operative	Operative
	B	CGC-1	Circumferential	Operative	Operative
	B	CGC-2	Circumferential	Operative	Operative
	B	CGD-1	Circumferential	Operative	Operative
	B	CGD-2	Circumferential	Operative	Operative

[a]Gages were inoperative at time of casting of cylinder.

"C" QUADRANT (TYPICAL GAGE LOCATIONS)   "A" QUADRANT   "D" QUADRANT (HOT SPOT)
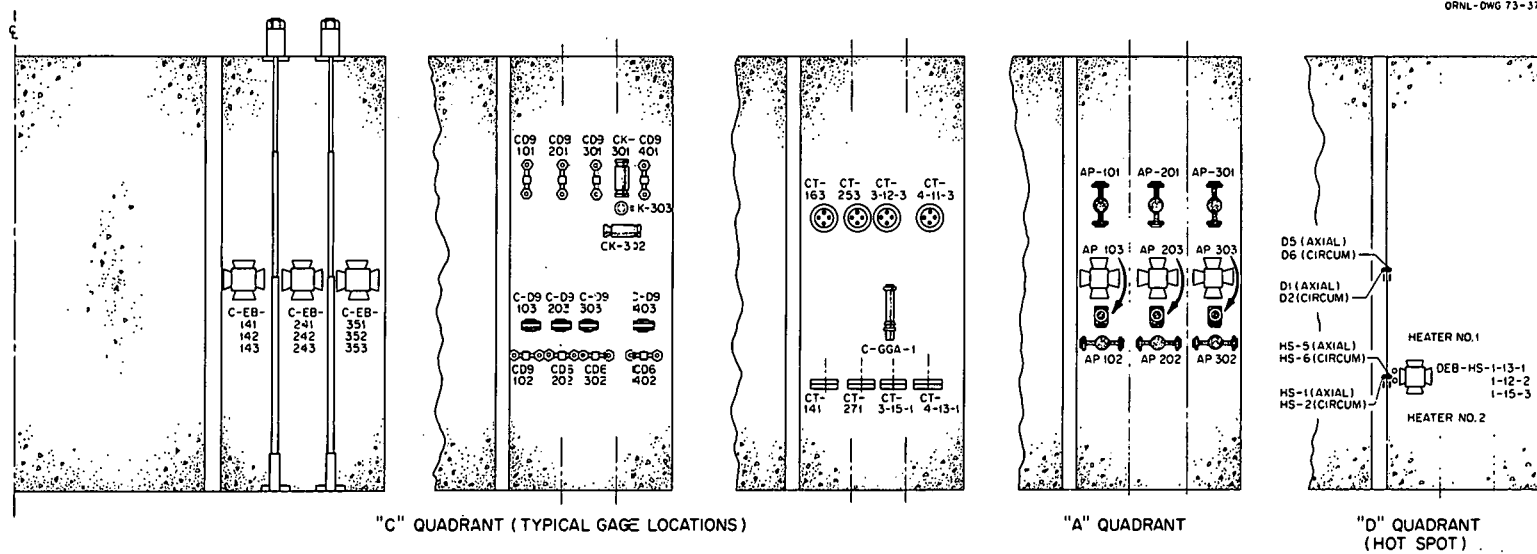
Fig. 2.1. Typical locations of each type of embedment gage.
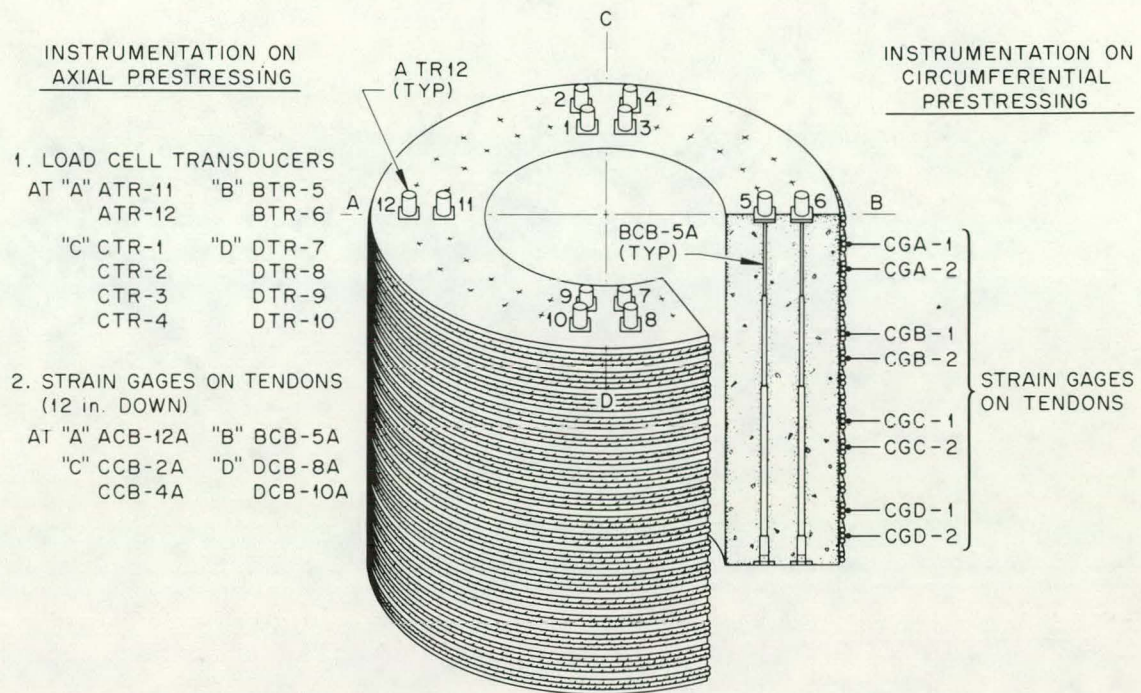
10

Fig. 2.2. Instrumentation on axial and circumferential prestressing (1 in. = 25.4 mm).

Relaxation of the stress in concrete is an important consideration in the design of a PCRV. Two types of embedment devices having a potential for measuring stress relaxation were developed at ORNL for this experiment. One device, consisting of two parallel concrete embedment strain gages, one of which has a pressure diaphragm attached, was described in Ref. 3 and is discussed further in Section 6.2. The relatively thin cylindrical cell shown in Fig. 2.3 is another device designed for measuring stress in concrete. The cell, which consists of two machined titanium disks, is shown disassembled in Fig. 2.4. The disks fit together in such a way as to continually deflect a cruciform-shaped spring steel beam instrumented with a four-arm bonded strain gage bridge. The application of an axial compressive stress to the assembled cell will further deflect the cruciform beam as monitored by the strain gages.

In order to provide a means for measuring possible variations in strain readings unrelated to existing stress conditions, the titanium disk through which the strain gage leads pass (see Fig. 2.4) houses a
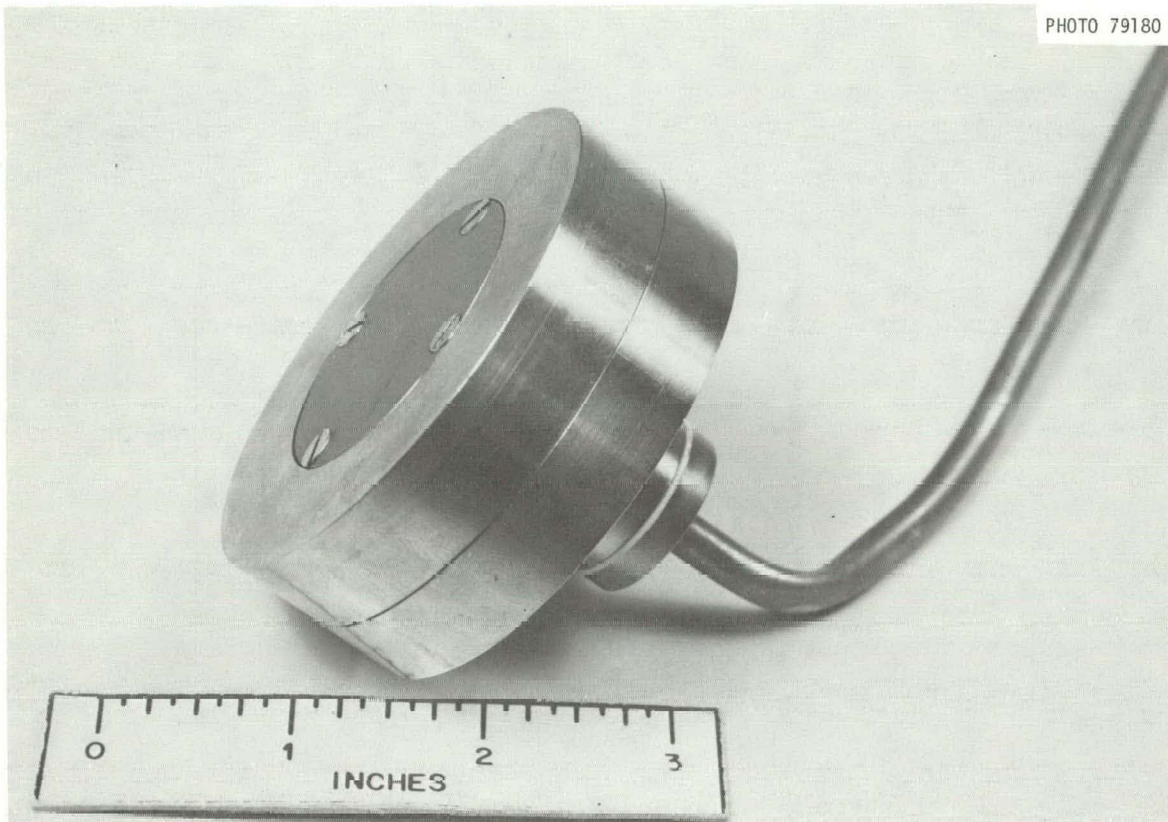
Fig. 2.3. Assembled titanium stress cell (1 in. = 25.4 mm).

miniaturized pneumatic ram. When activated, the ram deflects the cruciform
beam to a fixed reference stop that is designed to remain independent of
stress variations. Changes in successive readings of the beam gage in the
fixed deflection position can be used to determine the amount of instru-
mentation drift. Upon release of the pressure, the beam returns to its
former position.

The stress cell was fabricated of titanium in order to produce an
embedment having a coefficient of thermal expansion compatible with that
of the concrete. Thirteen titanium stress cells were load-calibrated under
uniaxial compression; nine of these were installed in the thermal cylinder,
and the remainder were installed in two 45.7- by 101.6-cm concrete
cylinders used to provide calibration of the embedded instrumentation.

A representative number of the single-filament resistance concrete
embedment strain gages were calibrated in an oil bath using specialized
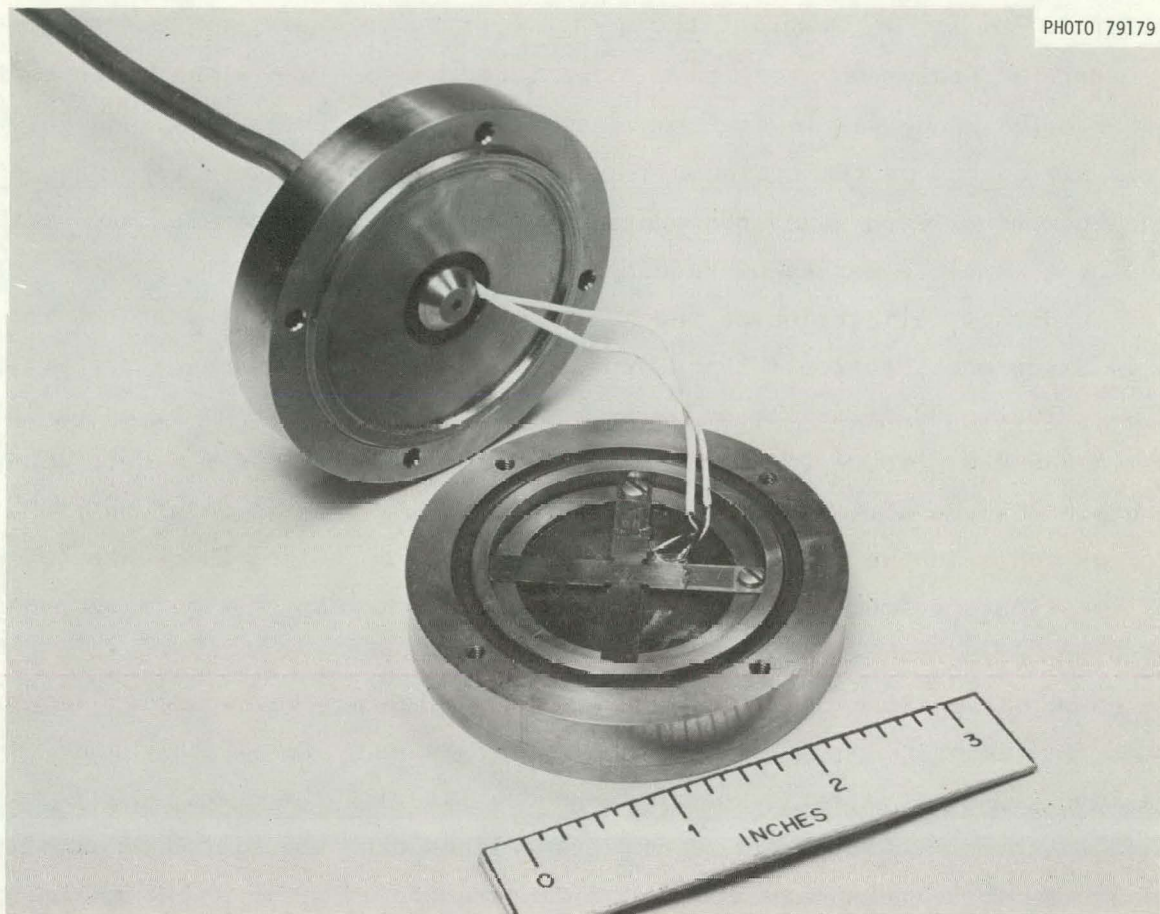equipment developed at the University of California as part of the ORNL

13

Fig. 2.4. Disassembled titanium stress cell (1 in. = 25.4 mm).

concrete program.[4] Gage calibration factors provided by the gage manufacturers were used for the remainder of the instrumentation.

The vibrating-wire gages and wire-wound resistance gages were monitored using seperate readout equipment. The remainder of the instrumentation, which also included 25 related thermocouples, was monitored with a computer-controlled data-acquisition system.

2.2 Moisture Probe

In order to provide information regarding the adequacy of the moisture seal and possible migration of moisture within the thermal cylinder, moisture readings were made, using a probe-type neutron and gamma-ray backscattering instrument. Readings were taken periodically, beginning just

prior to heatup, by lowering the moisture probe into sixteen 25.4-mm-OD thin-walled stainless steel tubes cast into the specimen along three radial lines. The probe was lowered to vertical positions 15.2, 45.7, and 76.2 cm from the bottom of the cylinder. Sets of three 1-min counts were made at each position, with standard counts being made at the beginning and at the end of a complete series of readings.

A direct calibration of the moisture probe was conducted at the Waterways Experiment Station (WES), Corps of Engineers, U.S. Army, Vicksburg, Miss. Twelve 30.5-cm-diam by 30.5-cm-long cylinders were cast, using the same concrete mixture that was used for the thermal cylinder model. Short sections of the 25.4-mm-OD stainless steel tubing used as moisture probe access tubes in the thermal cylinder model were cast into the center of each calibration specimen. The size of these specimens was chosen in accordance with recommendations made by the probe manufacturer.

The calibration procedure consisted of weighing the specimens and then taking a set of three independent 1-min probe counts immediately after casting and again after demolding (one day later). The demolded specimens were divided into four sets of three specimens each and placed in constant-environment chambers maintained at a temperature of 297.0 ± 1 K and having relative humidities of 100, 90, 80, and 70%, respectively. The specimens were removed from the chambers and weighed, and counts were made at 7, 28, 35, 42, 49, 57, 76, 87, and 112 days after casting.

3. ASSEMBLY AND CASTING

3.1 Assembly of Model

The bottom support and insulating layers of the model were assembled, as shown in Fig. 1.3, to the sheet-metal moisture seal located directly above the asbestos cement board. A temporary support superstructure was then erected on the base support framework.

Panelcoil heat exchangers served both as the walls of the pressurization annulus (heat exchangers A and B) and the outer wall of the test section (heat exchanger C) in addition to serving as the major part of the concrete formwork. An array of Nelson-type studs were attached to the surfaces of the two interior Panelcoils (A and B) to ensure that a good bond developed between the heat exchangers and the concrete. The B Panelcoil, which formed the inner surface of the test section, was also instrumented with 20 weldable strain gages and 5 thermocouples. The pressurization annulus was fabricated by welding the top of bottom tori to the A and B Panelcoils. The leads for instrumentation located inside the annulus passed through seals located in the upper torus. The resistance heater for the hot-spot test was attached at the lower third point of the B heat exchanger. After leak testing, the assembled annulus was positioned inside the structural formwork and welded to the bottom moisture seal. Assembly of the upper support formwork was then completed, and the axial prestressing and moisture tubes were installed.

The single-filament-type concrete embedment strain gages, which are relatively delicate, were precast in the form of three-gage rosettes for protection against breakage. It was also necessary, for the same reason, to precast the ten pressure stress cell components consisting of individual single-filament-type strain gages attached to pressure diaphragms. The concrete embedment instrumentation was positioned along the four gaged sections shown in Fig. 2.1, which were located 90° apart around the model. Three of the gaged sections can be seen in Fig. 3.1, which is a view of the mold assembly with the outer heat exchanger removed. Figure 3.2 shows a closeup of one gaged section. As shown in the figure, the gages were supported by clamps attached to tubes housing the longitudinal
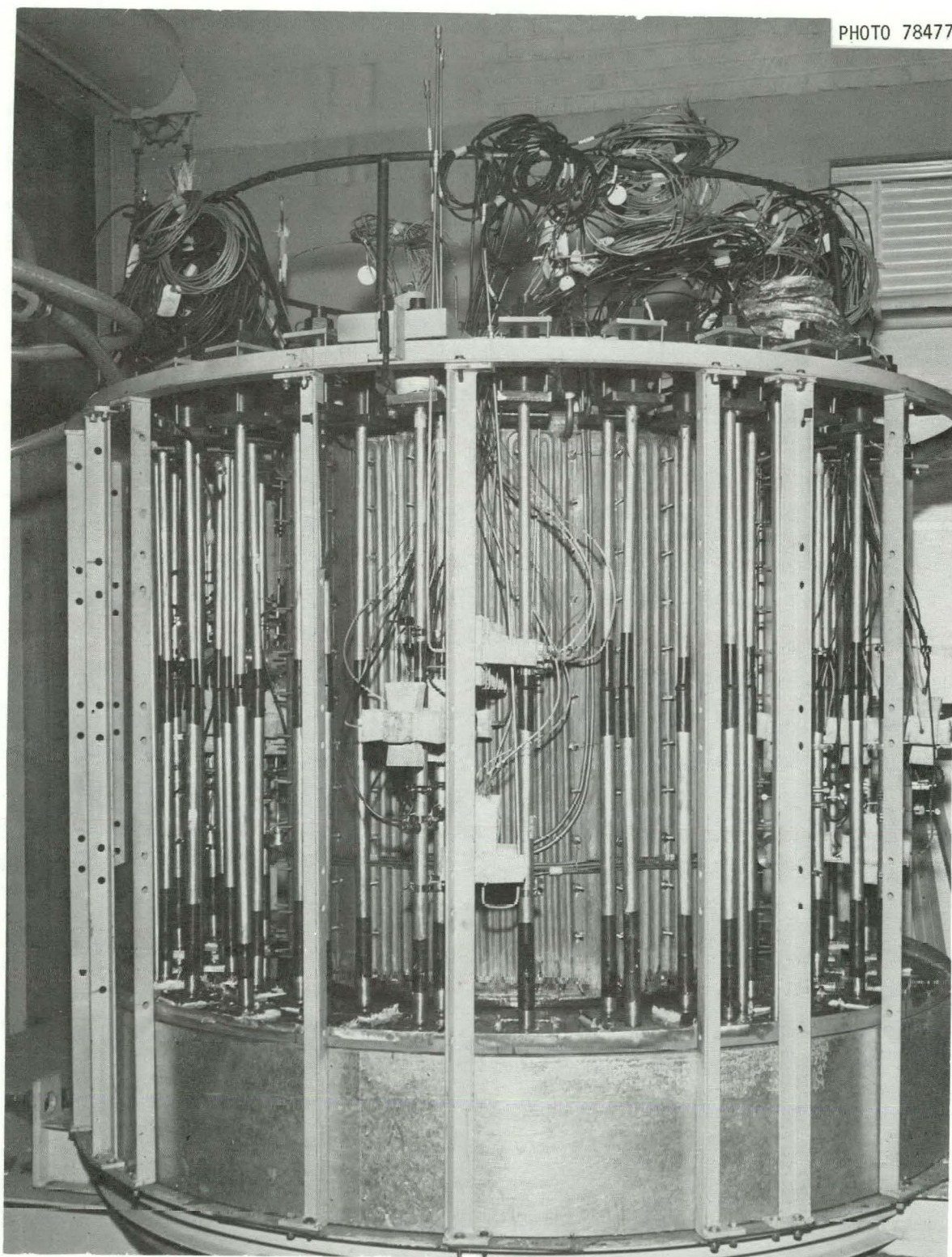
Fig. 3.1. Partially assembled mold with outer heat exchanger removed.
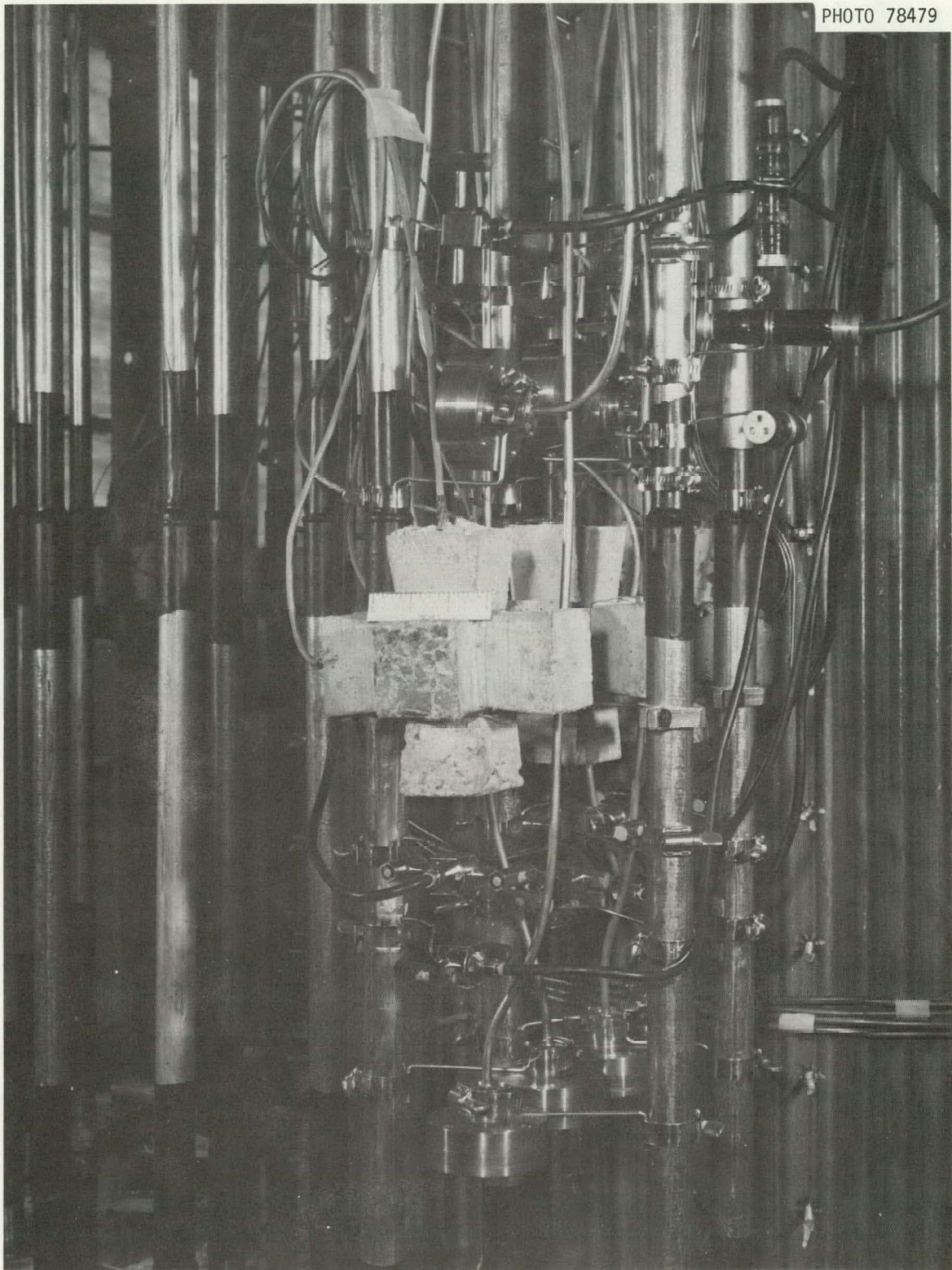
PHOTO 78479

Fig. 3.2. Close-up of instrumentation at one of four gaged sections.

prestressing. Shown in Fig. 3.2 from bottom to top are axial titanium stress cells; type A vibrating-wire strain gages; precast single-filament strain gage rosettes; and circumferential titanium stress cells, to the right of which are unbonded resistance strain gages. Axially oriented type A gages are shown at the top.

After the embedment instrumentation was installed, the outer heat exchanger was positioned and welded to the bottom moisture seal.

3.2   Temperature- and Pressure-Control Systems

The temperature-control system consisted of two water-circulation loops — one for heating and one for cooling. The two loops were essentially the same except for inclusion of a water heater in the heating system. The hot-water loop supplied both interior heat exchangers (A and B Panelcoils) from a common supply but at different flow rates; the cold-water system supplied the outer heat exchanger (C Panelcoil). Each loop was equipped with an extra pump to provide emergency backup and to allow for maintenance during periods of continuous operation. The assembled system and control instrumentation are shown in Fig. 3.3.

The annulus pressurization system consisted of four nitrogen bottles connected by a manifold to an oil expansion tank, which was in turn connected to the annulus of the model. During pressurization, the annulus and connecting line were filled with synthetic high-temperature hydraulic fluid to the level of the oil expansion tank. The applied pressure was controlled by the gas manifold pressure regulators.

3.3   Casting of Model and Companion Specimens

In addition to the thermal cylinder model, two 0.46-m-diam by 1.02-m-long cylindrical molds were fabricated and assembled. These specimens contained representative instrumentation of every type used in the thermal cylinder.

The assembled model and molds were transported on a flatbed trailer, as shown in Fig. 3.4, to the casting site at WES in Vicksburg, Miss. In the figure, which shows the concrete placing operation in progress, part of the plastic and wooden protective covering has been removed.
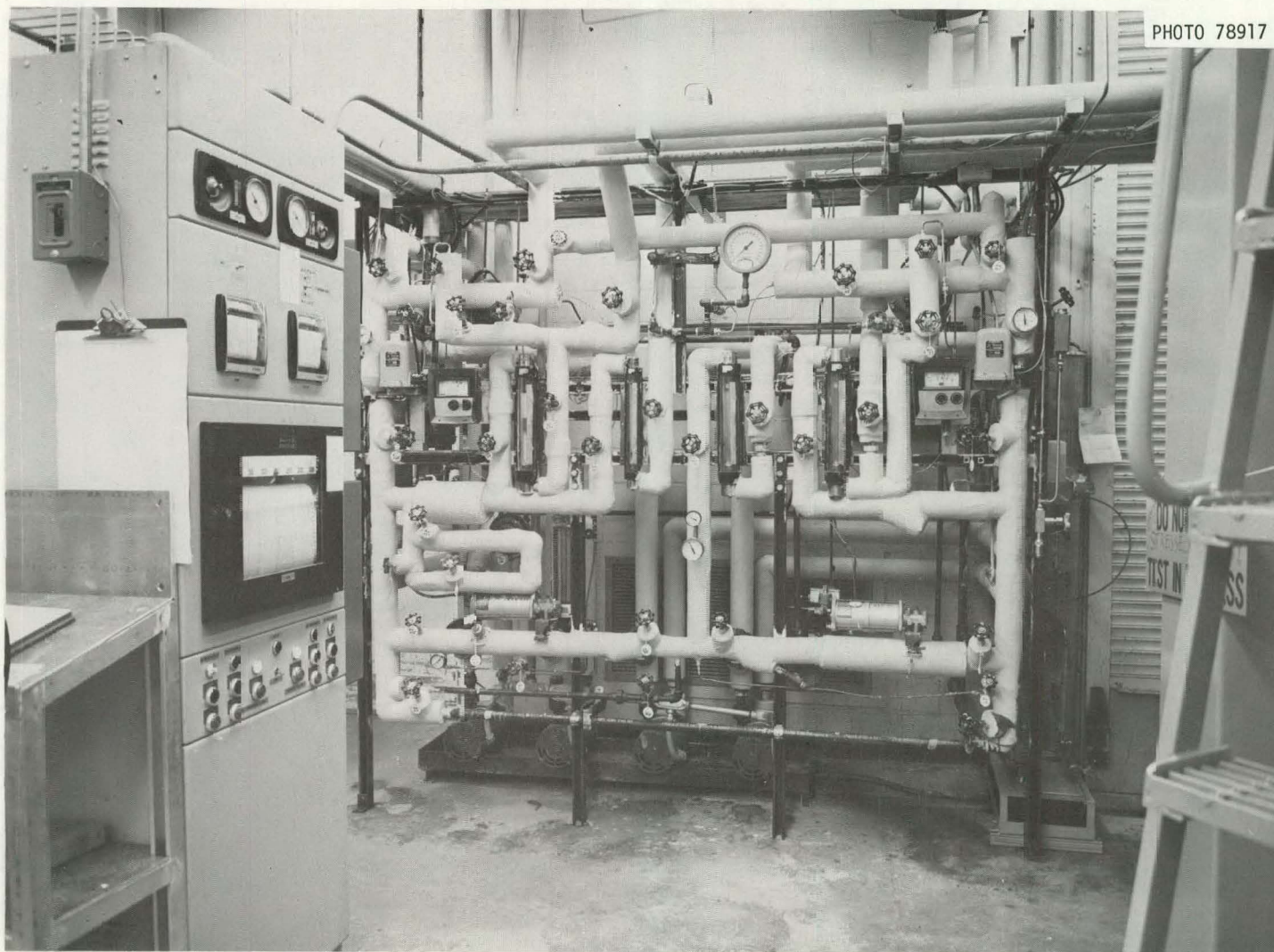
PHOTO 78917

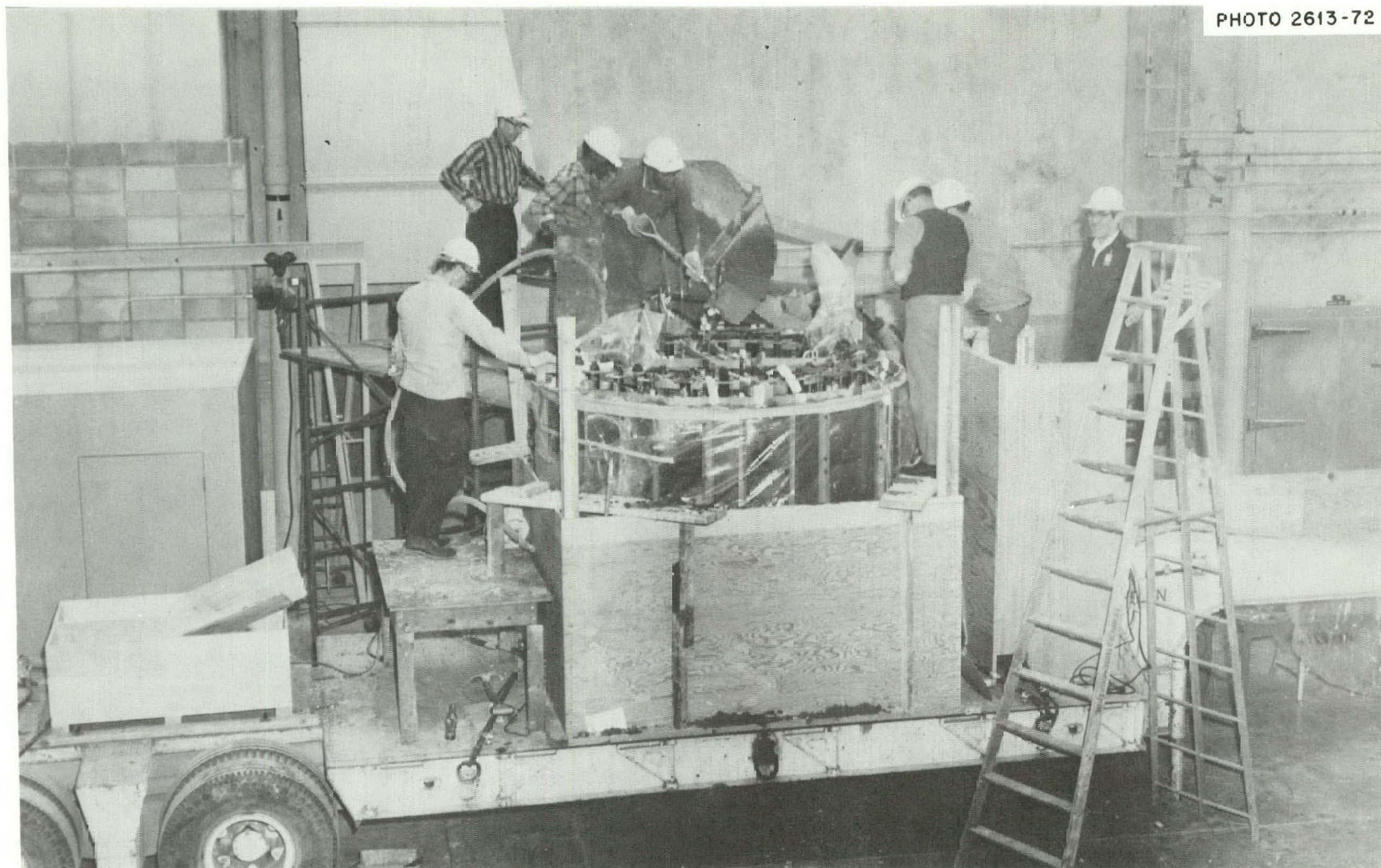Fig. 3.3. Temperature control system.

PHOTO 2613-72

Fig. 3.4. Casting operation, showing placing of concrete into thermal cylinder mold.

The thermal cylinder, two 0.46- by 1.02-m cylinders, and forty 0.15- by 0.30-m standard compression specimens were cast, using fourteen 0.38-m^3 batches of the concrete mixture described in Table 3.1. This is the same concrete mixture used in the ORNL concrete program basic studies.

Upon completion of the finishing operation, the exposed concrete was covered with wet burlap to prevent overnight drying. The following day all exposed concrete was sealed using a combination of epoxy and copper sheeting.

After an initial 14-day curing period at WES, the trailer was returned to ORNL, where the specimens were prepared for testing. The water-circulation manifolds and related piping were installed, and the temperature-control system was set a 297 K. With the exception of the vibrating-wire resistance strain gages and control thermocouples, the instrumentation was connnected to a 520-channel data-acquisition system.

Table 3.1. Thermal cylinder model concrete mixture

Materials

    Cement   Type 2 portland cement
    Aggregate
      Type   Carter limestone
      Nominal maximum size, cm (in.)   1.9 (0.75)
      Gradation   In accordance with ASTM designation C33-67

Mixture proportions [for 0.76-m^3 (1-yd^3) batch]

Material/SSD^a weight, kg (lb)   Portland cement/309.1 (681.5)
     Fine aggregate/626.6 (1381.5)
     Coarse aggregate/809.4 (1784.4)
     Water/176.9 (389.9)

Water-to-cement ratio,^{b} m^3/sk (gal/sk) 18.2×10^{-3} (4.8)

Actual cement factor,^{b} sk/m^3 (sk/yd^3)   9.48 (7.25)

Compressive strength, MPa (psi)   41.37 (6000) ± 10% at 28 days

^{a}SSD = saturated surface dry.
^{b}1 sk = 42.64 kg (1 U.S. sk = 94 lb).

4. TESTING

4.1 Concrete Strength Tests

Seven of the standard compression specimens were tested at WES. The remainder of the 0.15- by 30-m standard cylinders were transported in wet sawdust along with the thermal cylinder to ORNL, where compression tests were conducted at concrete ages of 28, 90, and 180 days. The results of these tests, together with the results of tests conducted at WES, are summarized in Table 4.1. The significant differences between 28-day compressive strengths of specimens tested at the two locations can be attributed to the 1 1/2 days of air drying required at WES for application of bonded strain gages. These differences are not seen when comparing ORNL 28-day strengths with WES trial batch results, where in both cases drying did not occur. A typical stress-strain curve and a plot of axial strain vs lateral strain are shown in Figs. 4.1 and 4.2, respectively.

Table 4.1. Summary of thermal cylinder
unconfined compression test results

Days from casting	Number of specimens	Compressive strength [MPa (psi)]	Modulus of elasticity [GPa (10^6 psi)]	Poisson's ratio	Cure[a]	Test site
			Trial batch mixture			
28	10	46.8 (6790)			Wet	WES
			Thermal cylinder concrete			
7	3	34.4 (4993)			Wet	WES
28	4	51.0 (7390)	31.0 (4.5)	0.26	Wet	WES
28	3	46.3 (6721)	31.7 (4.6)		Wet	ORNL
90	6	60.8 (8819)	35.9 (5.2)	0.28	Dry	ORNL
90	6	60.7 (8804)	37.9 (5.5)	0.31	Wet	ORNL
180	4	62.7 (9100)	37.2 (5.4)	0.28	Wet	ORNL
180	3	62.8 (9115)	37.9 (5.5)	0.26	Dry	ORNL

[a]Wet — moist cured to time of testing; dry — moist cured for 28 days and air dried to time of testing.
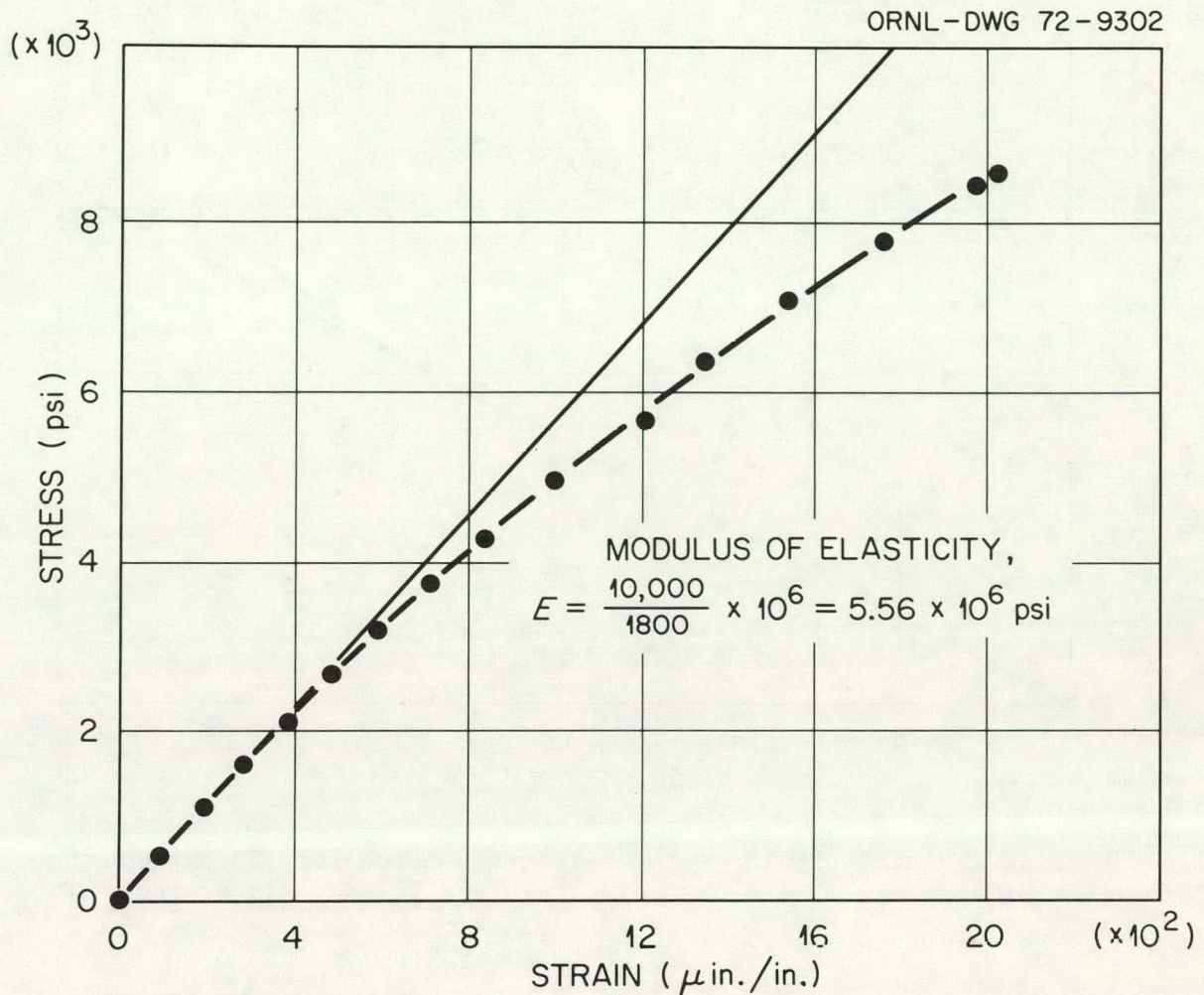
Fig. 4.1. Axial stress-strain curve for 180-day compression test of specimen 13 (28-day moist cure and 152-day air drying). (1 psi = 6895 Pa.)

4.2 Posttensioning of Model

The thermal cylinder circumferential prestressing system was assembled after the specimen was installed at the ORNL test site. Posttensioning took place at a concrete age of 90 days. The circumferential tendons were stressed using seven 0.89-MN (100-ton) rams; six 0.27-MN (30-ton) rams were used to stress the axial tendons. The rams are shown positioned for post-tensioning in Fig. 4.3. Each tendon was initially stressed to the half-load level, using a predetermined loading schedule. The schedule was then repeated, with the stress in each tendon being increased to the design
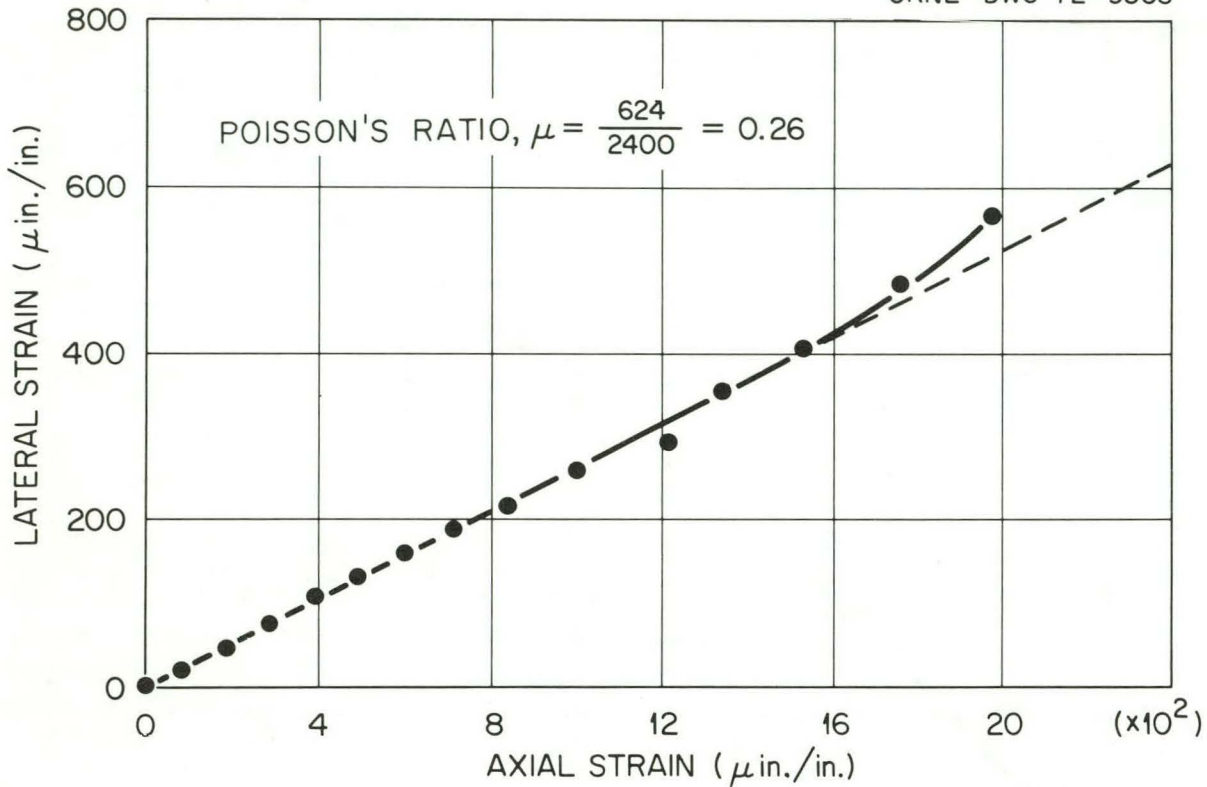
Fig. 4.2. Axial strain vs lateral strain curve for 180-day compression test of specimen 13 (28-day moist cure and 152-day air drying).

level. After the problems associated with localized crushing of the top moisture seal were solved, good agreement was seen between the loading applied to longitudinal tendons and the final loadings as indicated by the tendon transducers. Good agreement was also seen between the measured circumferential tendon strain and design values.

After posttensioning, the remaining phases of assembly, which consisted of installation of the upper insulation and moisture tube extensions and filling of the pressurizing annulus with hydraulic fluid, were completed. The completed model is shown in Fig. 4.4.

4.3 Simulated Vessel Operation

The scheduled heating phase of the experiment was initiated at a concrete age of 130 days. While the temperature of the outer heat exchanger
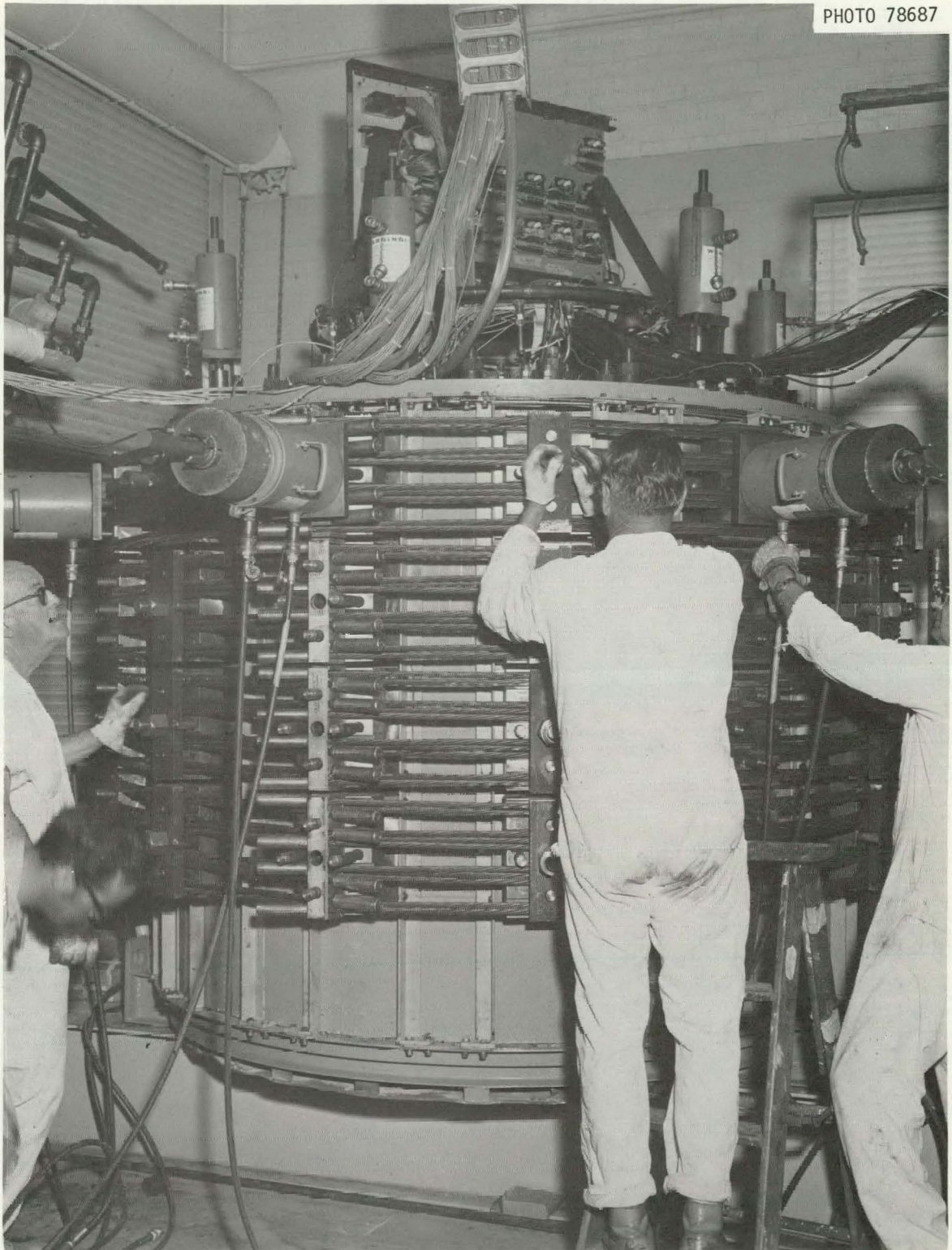
PHOTO 78687

Fig. 4.3. Posttensioning operation, showing longitudinal and circumferential rams in position.
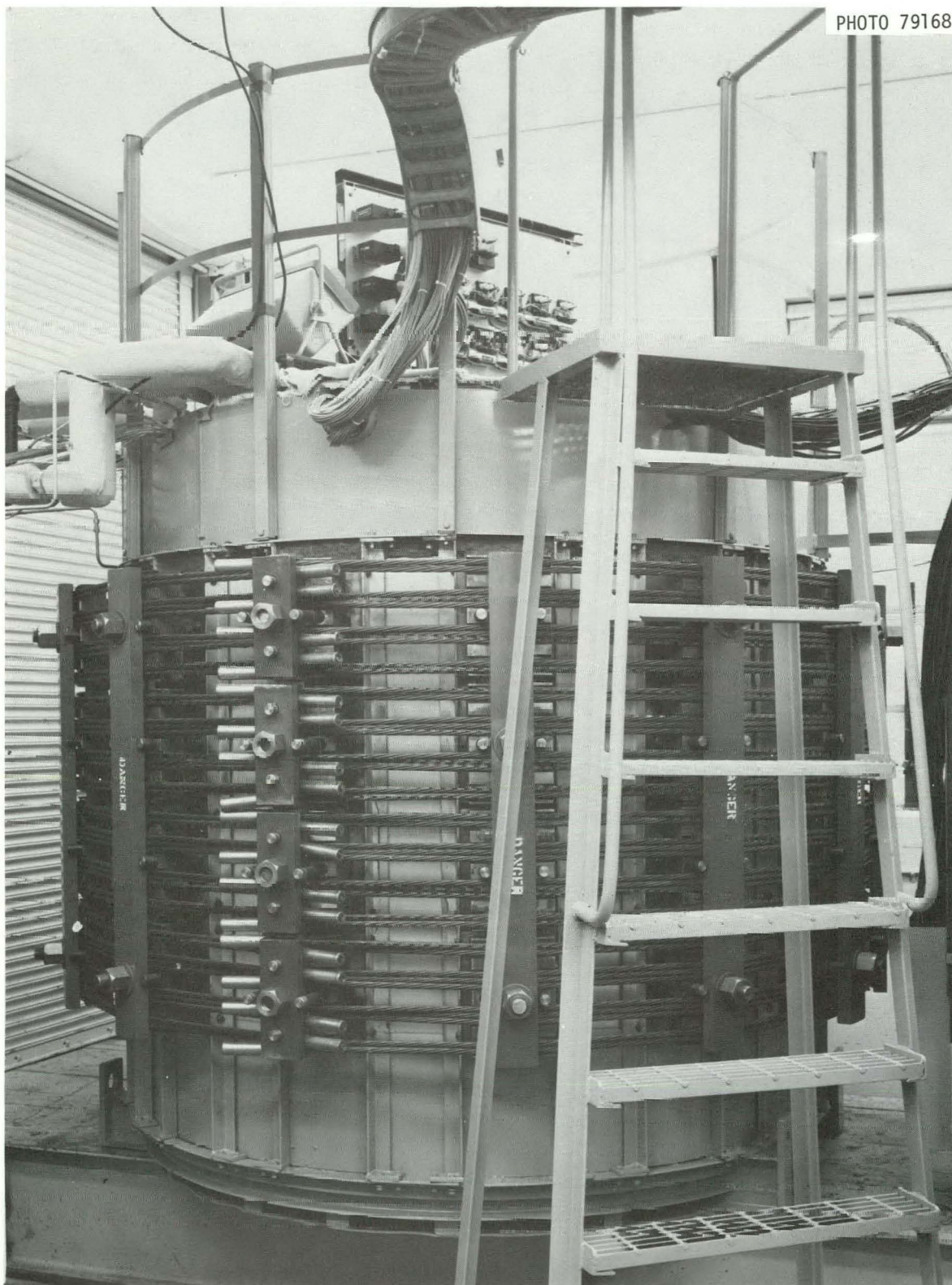
PHOTO 79168

Fig. 4.4. Completed thermal cylinder model.

was maintained at 297 K, the temperature of the interior heat exchangers
(A and B Panelcoils) was increased at a rate of 2.8 K per day from the
initial 297 K to a final value of 338.7 K. The resulting through-the-wall
thermal gradient shown in Fig. 4.5 was maintained for a period of approxi-
mately 14 1/2 months as indicated in Fig. 1.2.

In addition to the prestress loading and thermal gradient, the model
was subjected to a 4.83-MPa internal pressure by means of the annulus
during the two time increments shown in Fig. 1.2. The initial 194-day
pressurization period simulated normal PCRV operating conditions followed
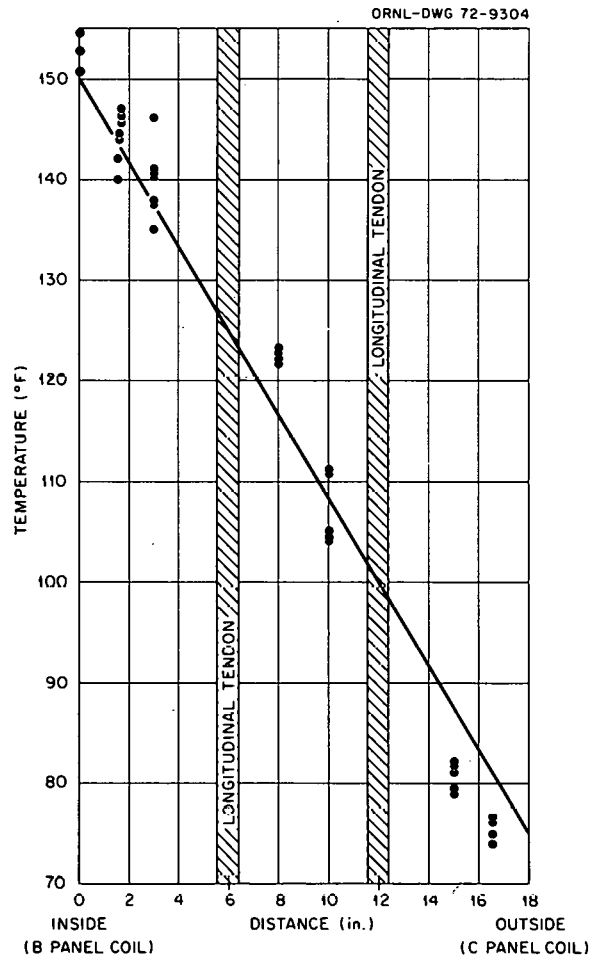by a 146-day reactor shutdown.

Fig. 4.5. Final thermal cylinder temperature gradient. Points
indicate individual temperature readings of thermocouples and precision
resistors. [1 in. = 25.4 mm; K = 273.15 + 5/9 (°F − 32).]

4.4 Hot-Spot Test

After the shutdown period, the 4.83-MPa pressure was reapplied and
maintained for the duration of the hot-spot test. The inner water-circu-
lation system was shut down, and two electric resistance heaters located
on the concrete side of heat exchanger B were activated 21 days after re-
pressurization. After an initial two-week adjustment period, the tempera-
ture stabilized at the specified value of 505.4 K on the heater sheath and
was maintained near that level for the 84-day duration of the test.

At the end of that period, the inner surface was cooled to 338.7 K,
using the inner water-circulation system, and eventually was cooled to
297 K in a second step. This temperature excursion simulates an off-design
hot-spot condition in which the liner cooling system and/or the insulation
is assumed to have failed in an operating nuclear reactor.

5. ANALYSIS

A time-dependent creep analysis of the entire operational history of the thermal cylinder model was conducted using the SAFE-CRACK computer program[5] together with concrete materials properties data developed at the University of Texas[6] for the same basic concrete mixture. The original computer program was modified to include a new integration scheme and a new temperature treatment based on the shift principle.[7] These improvements are most important in cases where the stress relaxation curve deviates appreciably from a straight line. The time-temperature shift treatment is applicable to creep behavior only. In addition, the new integration scheme will permit the use of larger time steps in the analysis, although this was not needed at this time for analyzing the thermal cylinder model. The complete analysis employed 47 time steps covering 585 days from the completion of posttensioning.

The analytical model is the axisymmetric thick-walled cylinder shown in Fig. 5.1, having the dimensions and geometry of the test model. Both the cylinder and core are included in the finite-element grid. A total of 564 elements are used, with triangular ring elements representing the concrete and membrane shell elements representing the liner or heat exchangers. The circumferential prestressing is represented as uniform pressure applied to the outer barrel section, and the axial prestressing tendons are treated as concentrated nodal loads. Once the specified failure criteria are exceeded, the affected concrete element is allowed to crack, and new stiffness and load matrices are computed in the analysis. The resulting new equilibrium equations are then solved for new displacements.

A heat transfer analysis was performed for the hot-spot condition to evaluate the temperatures that were measured during this overtemperature event. Internal and external boundary conditions and materials properties were varied to obtain the best fit of measured temperatures in the test specimen section. The material and heat transfer parameters that gave the best fit are listed in Table 5.1, and the recorded and predicted temperatures are shown in Fig. 5.2. The transport of heat by the synthetic fluid
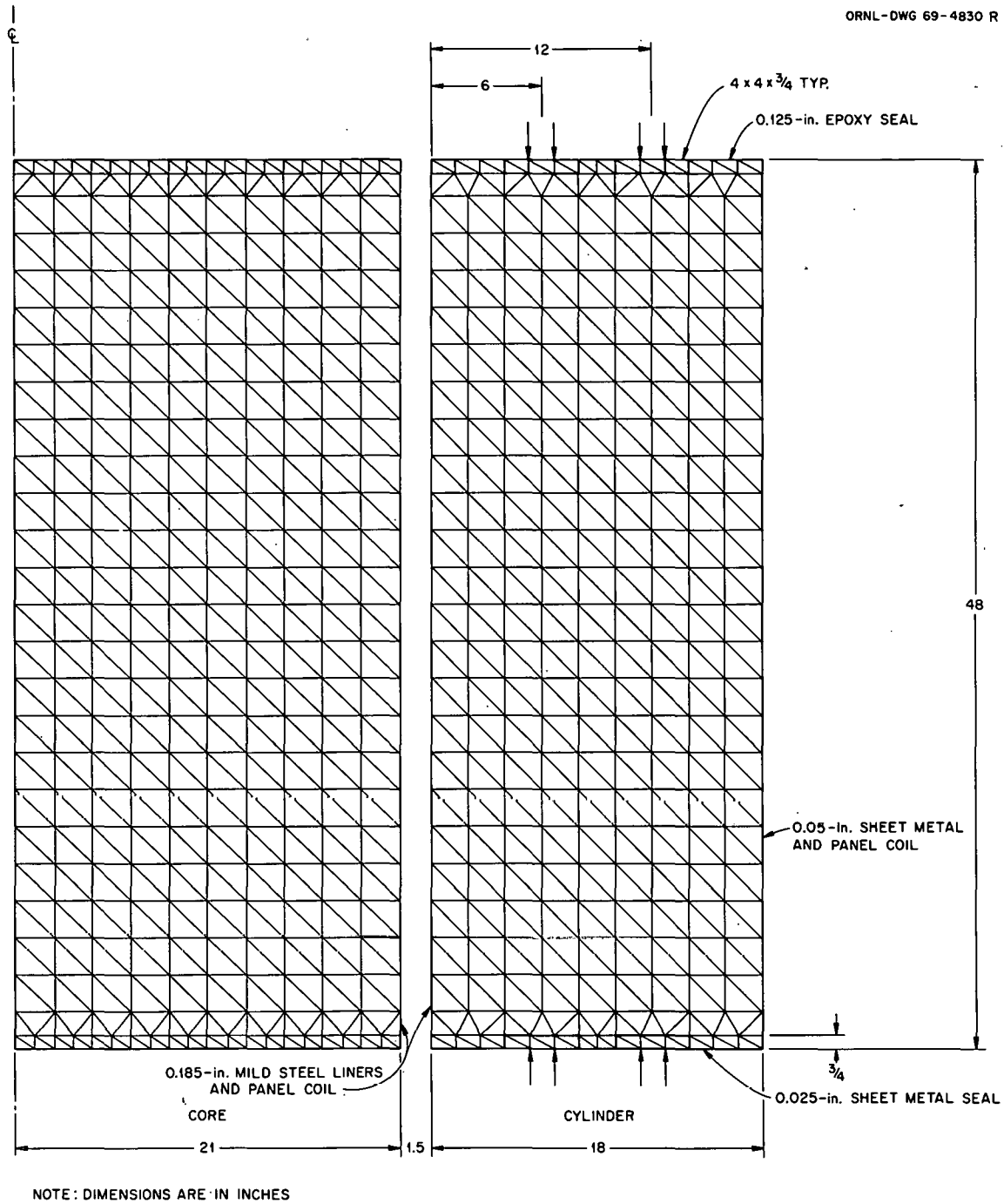
Fig. 5.1. Axisymmetric finite-element layouts for thermal cylinder test section and core (1 in. = 25.4 mm).

Table 5.1. Material and heat transfer parameters for hot-spot analysis

Electric heater power, 3100 W
Recorded sheath temperature, 505.3 K (450°F)

	Concrete	Oil	Water
Density, kg/m^3 (lb/ft^3)	2402.8 (150.0)	1414.4 (88.3)	961.1 (60.0)
Thermal conductivity, W/m•K [Btu hr^{-1} ft^{-1} (°F)$^{-1}$]	2.86 (1.65)	0.118 (0.068)	0.69 (0.4)
Specific heat, J/kg•K [Btu lb^{-1} (°F)$^{-1}$]	837.4 (0.2)	1172.3 (0.28)	4186.8 (1.0)
Heat transfer coefficient, W/m•K [Btu hr^{-1} ft^{-1} (°F)$^{-1}$]		a	3459.1 (2000)

^{a}Convection type, $h = 0.135 (\Delta T)^{0.25}$, where h is the coefficient (Btu hr^{-1} ft^{-2}) and ΔT is the temperature difference between node bulk temperature and node surface temperature (°F). [To convert from Btu hr^{-1} ft^{-1} (°F)$^{-1}$ to W/m•K, multiply by 1.72958.]
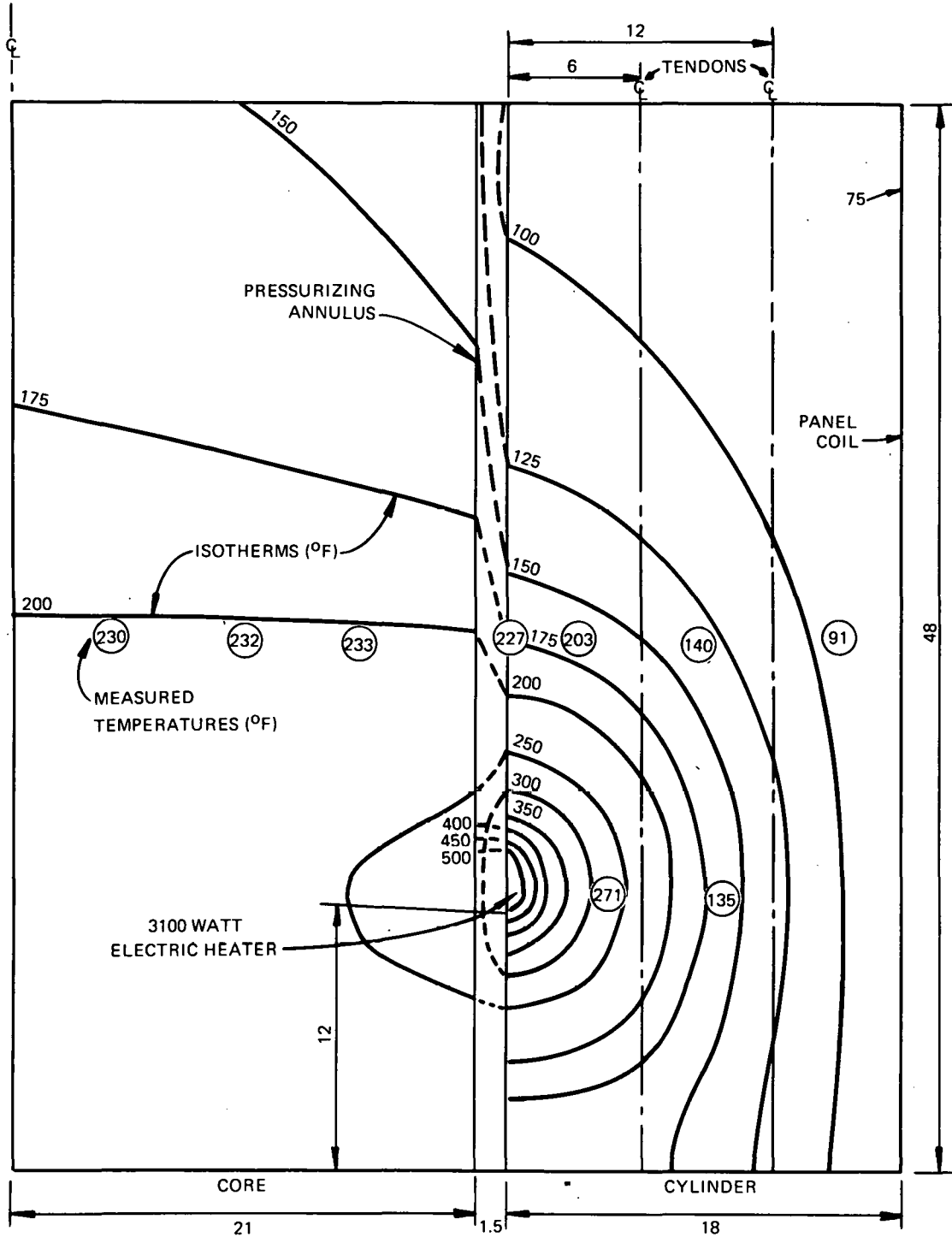
ORNL—DWG 73—2212

Fig. 5.2. Temperature profiles during thermal cylinder hot—spot test [1 in. = 25.4 mm; K = 273.15 + 5/9 (°F − 32)].

in the pressurizing annulus, the refluxing of water and steam in the inactive circulating-water heating coils, and the variation in properties of the concrete as a function of temperature made this analysis difficult. However, the agreement with experimental data is generally good.

. The results of the finite-element analysis are compared with the corresponding experimental results in the next chapter.

6. EXPERIMENTAL AND ANALYTICAL RESULTS

The performance of the 155 gages included in the model is summarized in Table 6.1; however, no general conclusions can be reached on overall gage performance, since there were 11 gage types or installations, each having a different level of development or calibration at the time of selection and each having been installed and checked under widely varying conditions. The following sections discuss the relative performance of the various types of instrumentation. The strains shown in the various data plots have all been adjusted to eliminate thermal expansion.

Table 6.1. Thermal cylinder test gage survival

Gage type	Letter designation	Total number	Number failed	Percent survival
Embedment gages				
Single-filament resistance	EB	47	18	61.7
Vibrating wire				
Type A	D	27	21	22.2
Type B	P	9	3	33.3
Type C	GA	1	1	0
Wound-wire resistance		6	1	83.3
Stress cells				
Titanium resistance	T	8	3	62.5
Pressure diaphragm	PSC	6	6	0
Strain gages				
Weldable (liner)		19	6	68.4
Axial tendons	CB	12	3	75.0
Circumferential tendons	CG	8	0	100.0
Load cells				
Axial tendons	TR	12	1	91.7
Total		155	63	59.4

6.1 Embedment Strain Gages

Of the various concrete embedment gages, the single-filament resistance type provided the most consistent and interpretable data. The performance of the vibrating-wire gages varied markedly by type, which was due in part to a mismatch in readout equipment.

Comparisons of analytical and experimental results for axially and radially oriented gages located in position 1 are given in Figs. 6.1 and 6.2, respectively. (See Sect. 2.1 for a complete explanation of gage and position designations.) In both cases, the prestressing and pressurization strains were overestimated, while strains produced during heatup were underestimated. The behavior of the axial gages during hot-spot heating appears erratic, since a strain jump was recorded shortly after repressurization. The probable causes of this effect as well as the sharp fluctuations in analytical values are discussed in Chap. 7.

The calculated and experimental results for gages in the second rosette position are given in Figs. 6.3 to 6.5. The same behavioral trends seen for the gages in position 1 were recorded by these gages as well, with the prestressing and pressurization strains being overestimated and the heatup strains underestimated. As expected, the recorded strains during hot-spot heating were less deviant, since these gages were farther away from the heated zone (center rosette position of Fig. 2.1). However, significant strain jumps were again monitored by the axial gages, and the analytical curves showed sharp fluctuations during hot-spot heating.

Single-filament-type embedment strain gages were also positioned in the concrete directly adjacent to the hot-spot heaters, as shown in Fig. 2.1 for the "D" section. In Figs. 6.6 and 6.7, calculated and experimental results are compared for radial and circumferential gages at the hot spot. The prestressing strains agreed exceptionally well for these two gages, although, as seen previously, the initial heatup strains differed significantly from the calculated values and the experimental pressurization strains were consistently low. With the exception of three questionable calculated data points in Fig. 6.6, the experimental and analytical curves followed each other exceedingly well during the hot-spot test.

Average comparisons for the type A vibrating-wire strain gages in radial position 1 (see Fig. 2.1) are shown in Figs. 6.8 to 6.10 for axial, radial, and circumferential directions, respectively. The same general trends discussed for the single-filament-type gages shown in Figs. 6.1 and 6.2 were recorded by this entirely different type of concrete embedment strain gage, which was cast directly into the concrete of the thermal
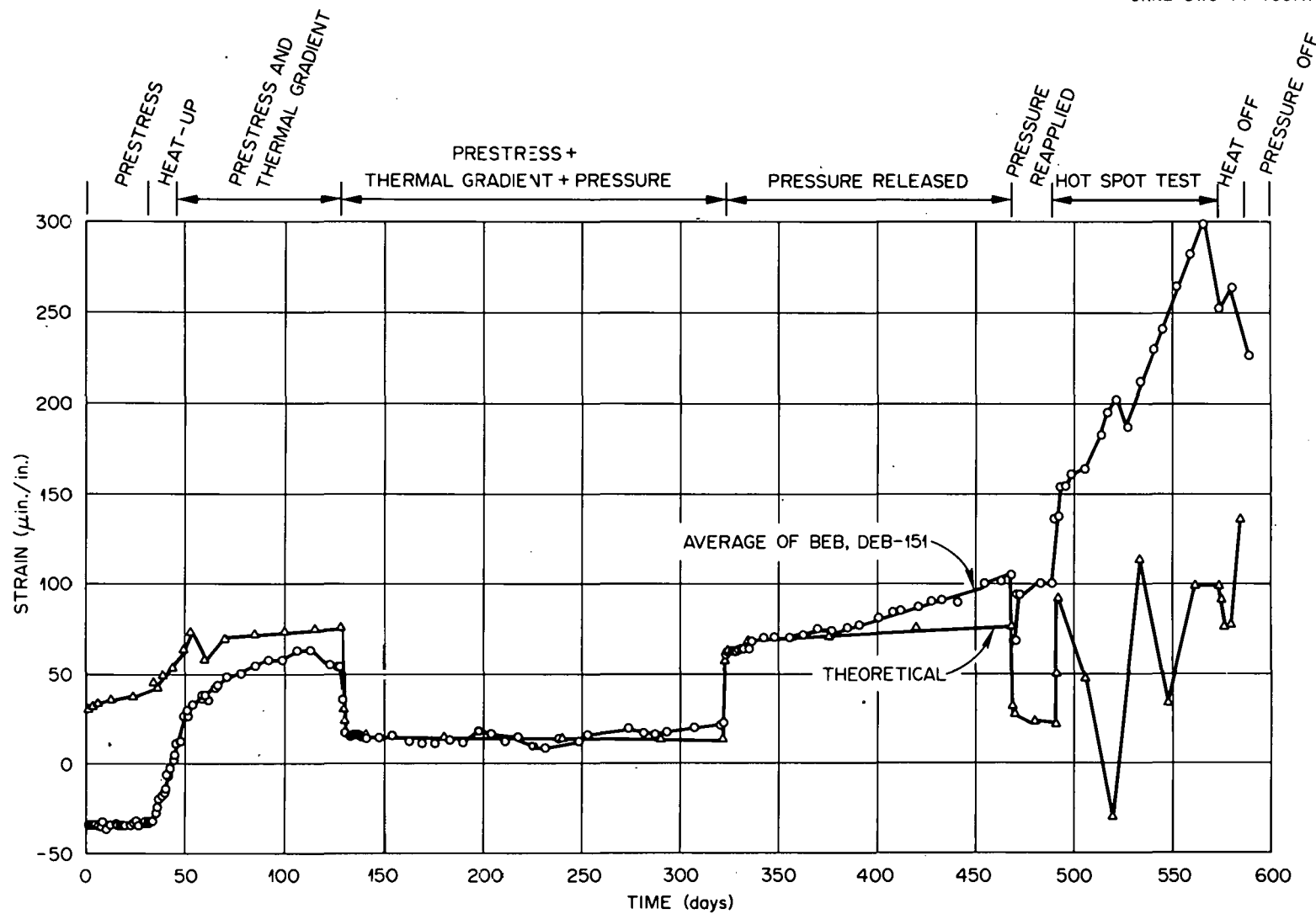
Fig. 6.1. Calculated and experimental results for first-position axial single-filament resistance strain gages.
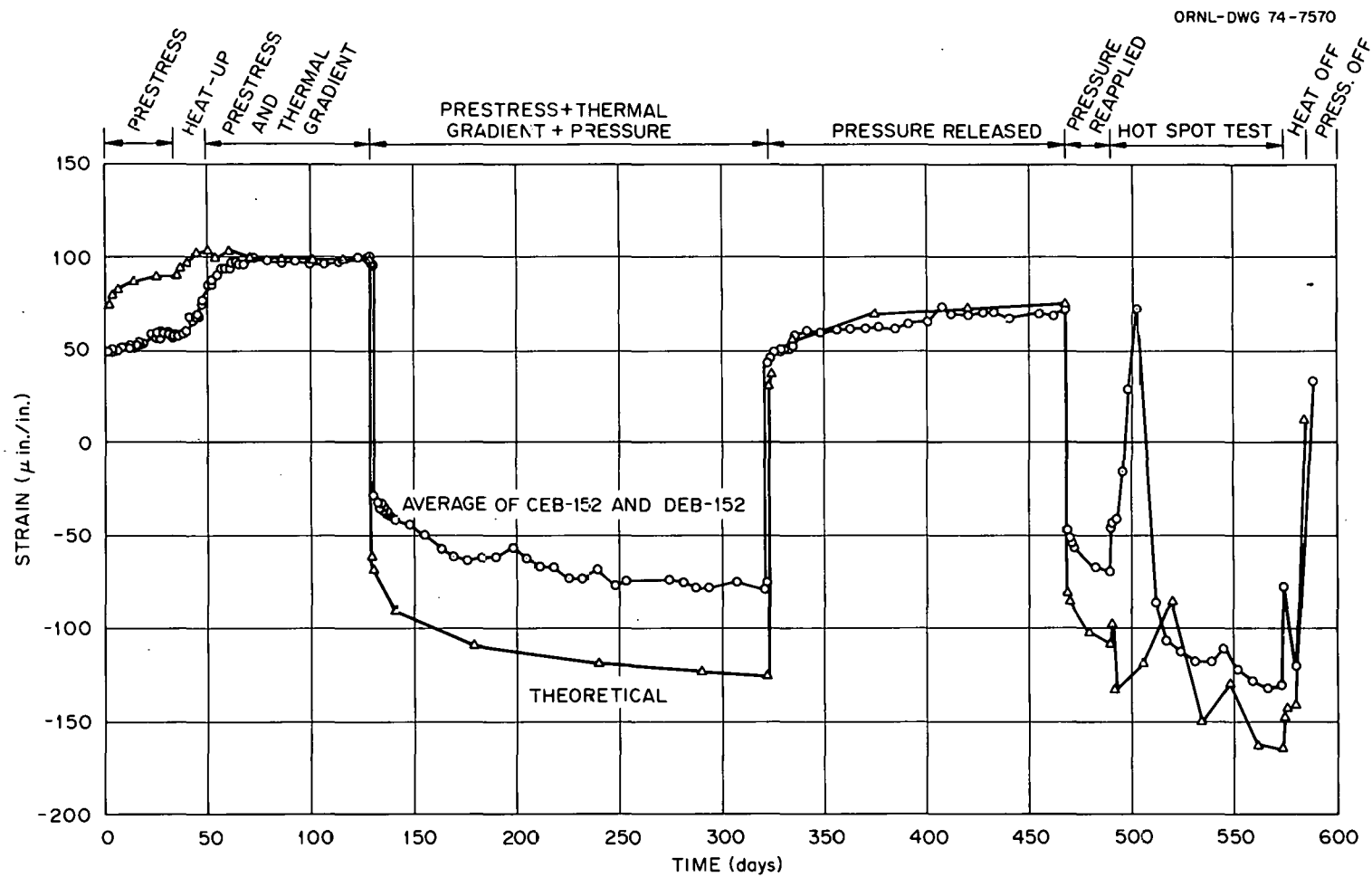
Fig. 6.2. Calculated and experimental results for first-position radial single-filament resistance strain gages.
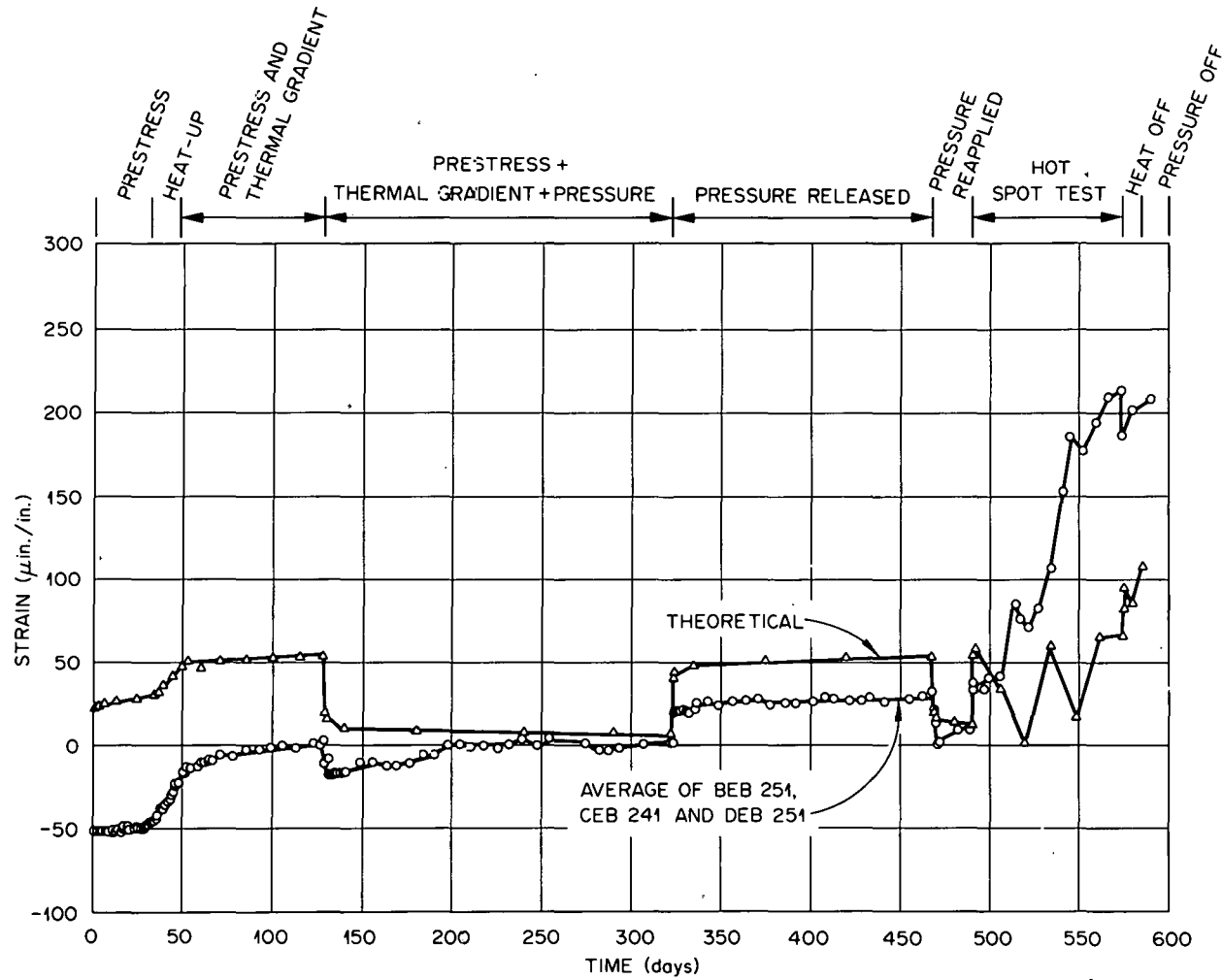
Fig. 6.3. Calculated and experimental results for second-position axial single-filament resistance strain gages.
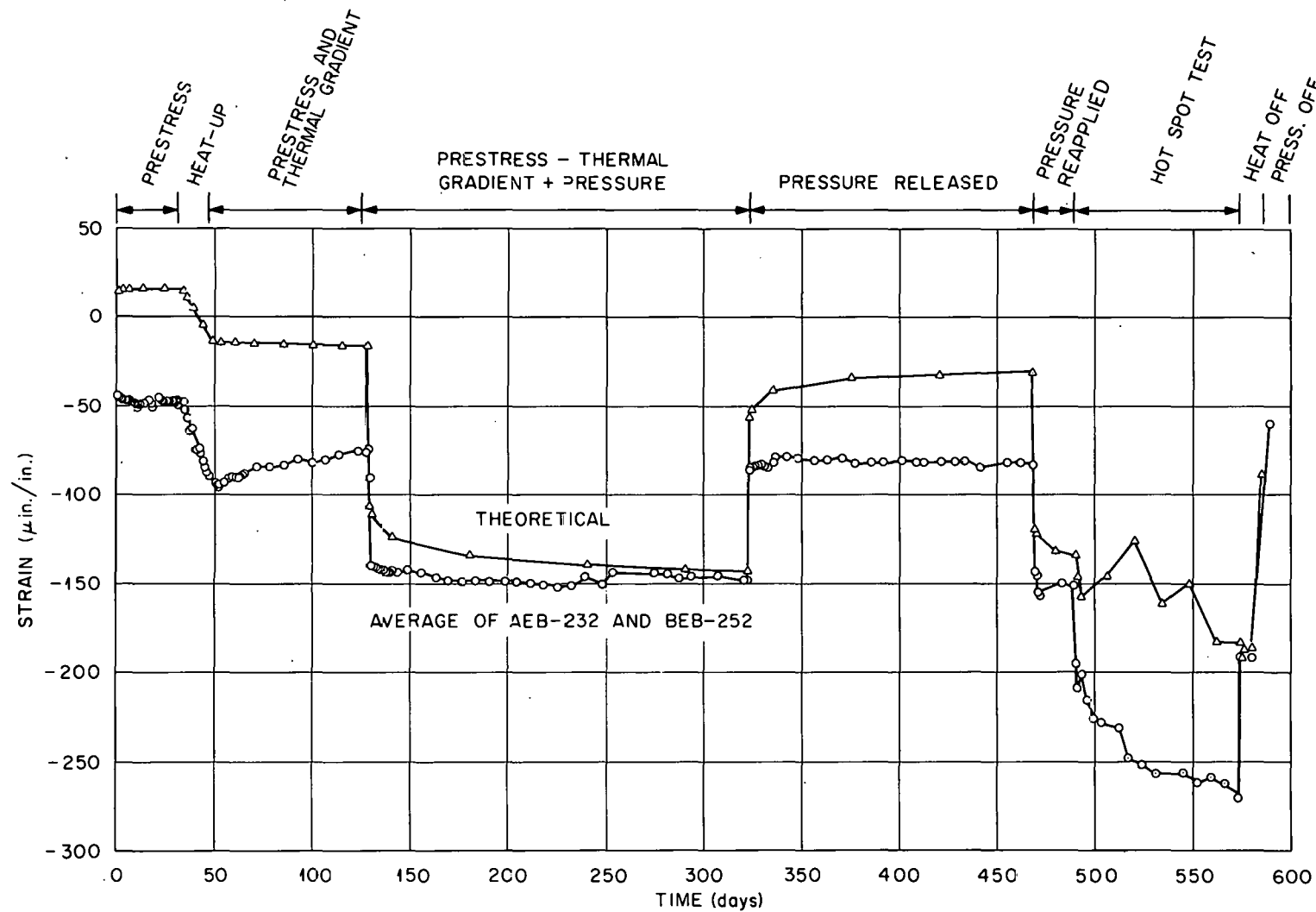
Fig. 6.4. Calculated and experimental results for second-position radial single-filament resistance strain gages.
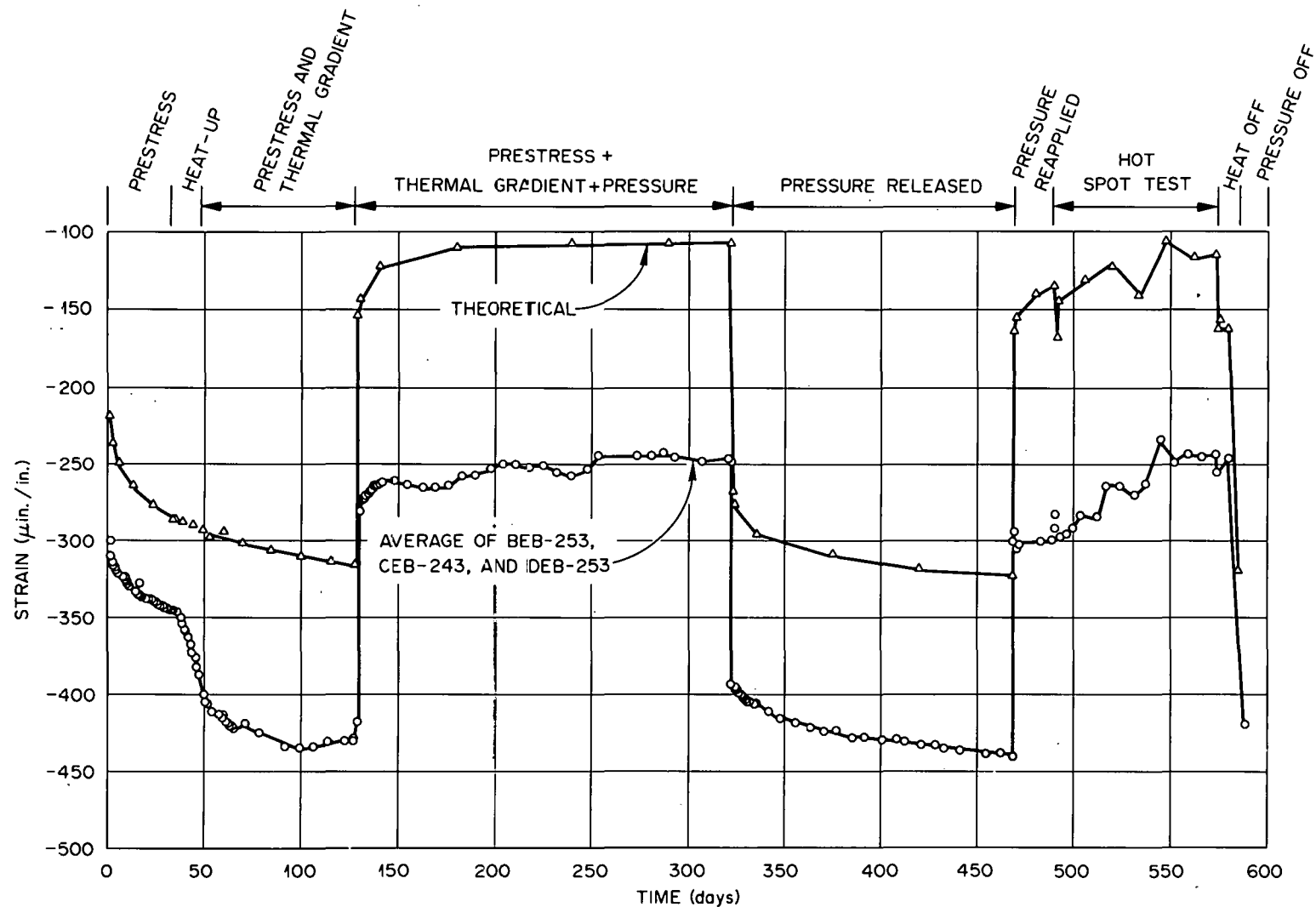
Fig. 6.5. Calculated and experimental results for second-position circumferential single-filament resistance strain gages.
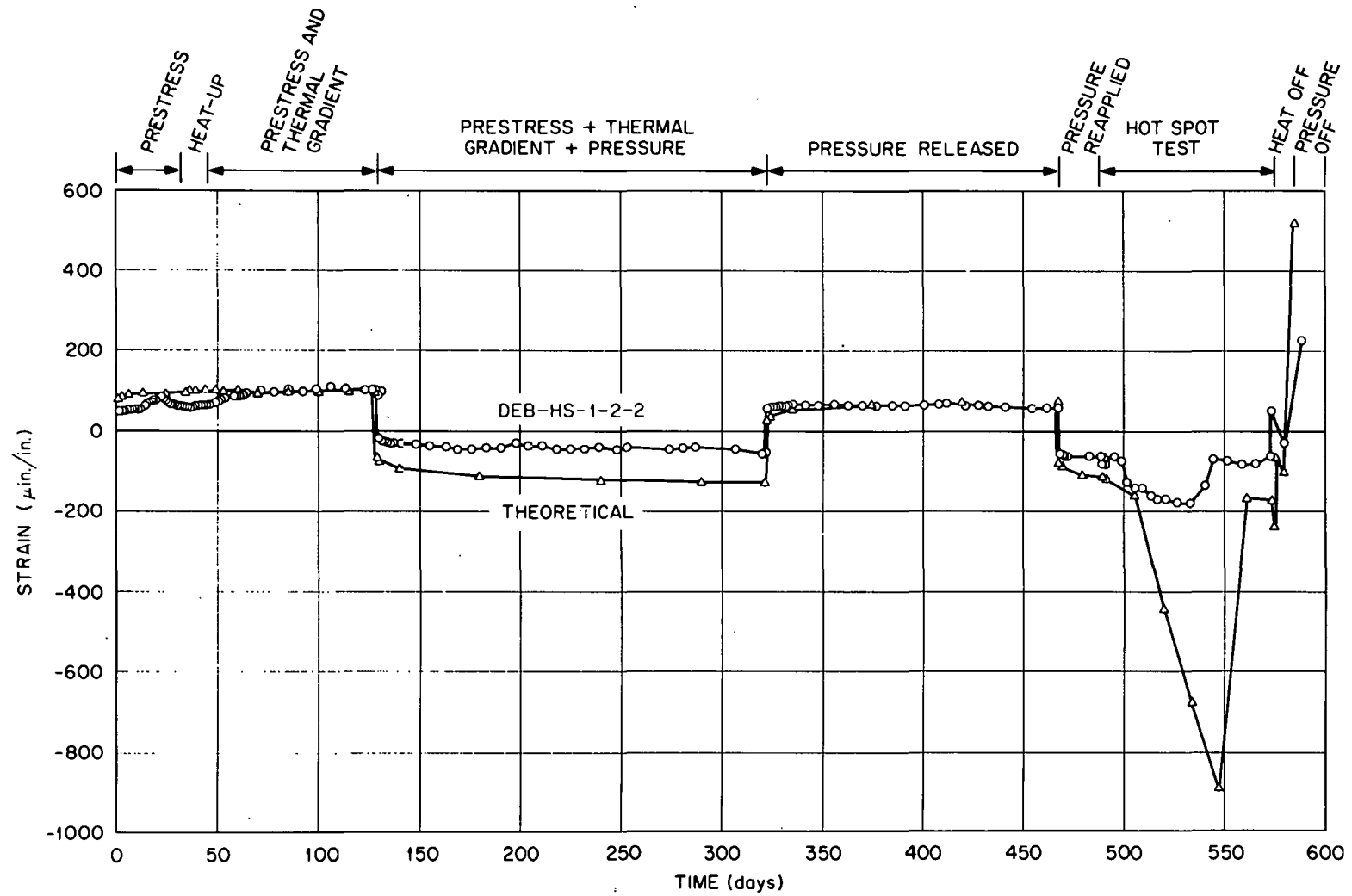
Fig. 6.6. Calculated and experimental results for hot-spot-position radial single-filament resistance strain gage.
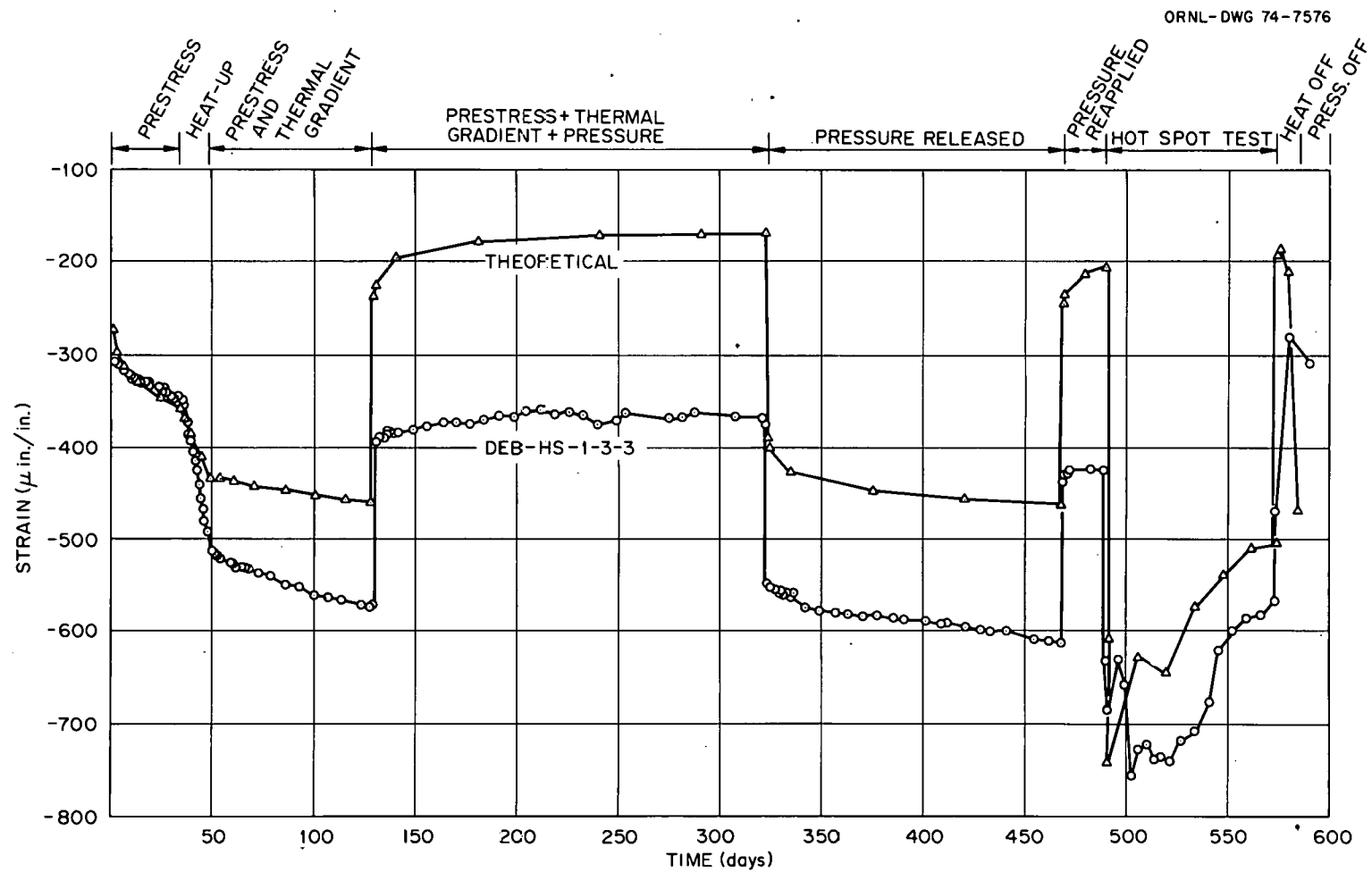
Fig. 6.7. Calculated and experimental results for hot-spot-position circumferential single-filament resistance strain gage.
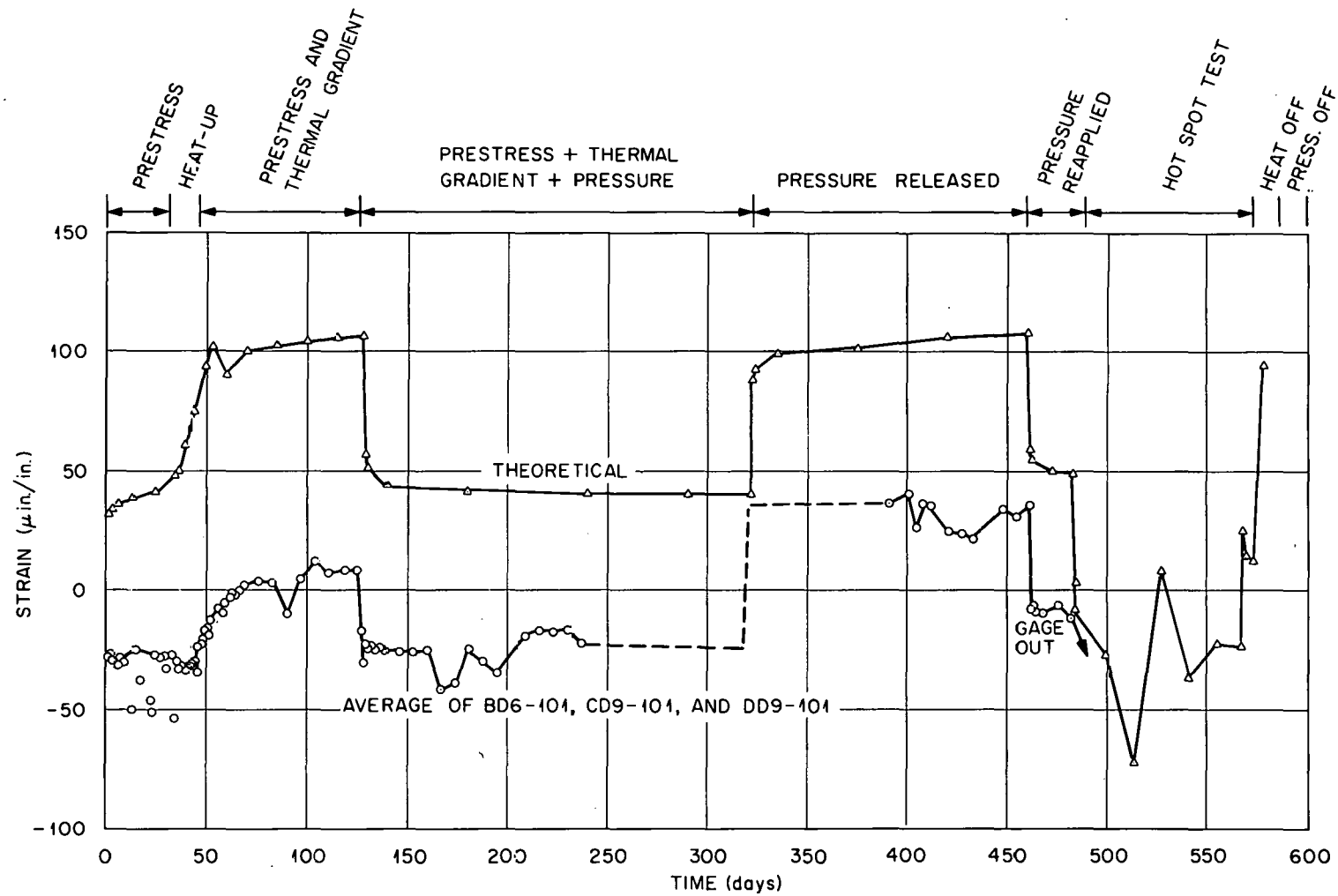
Fig. 6.8. Calculated and experimental results for first-position axial type A vibrating-wire strain gages.
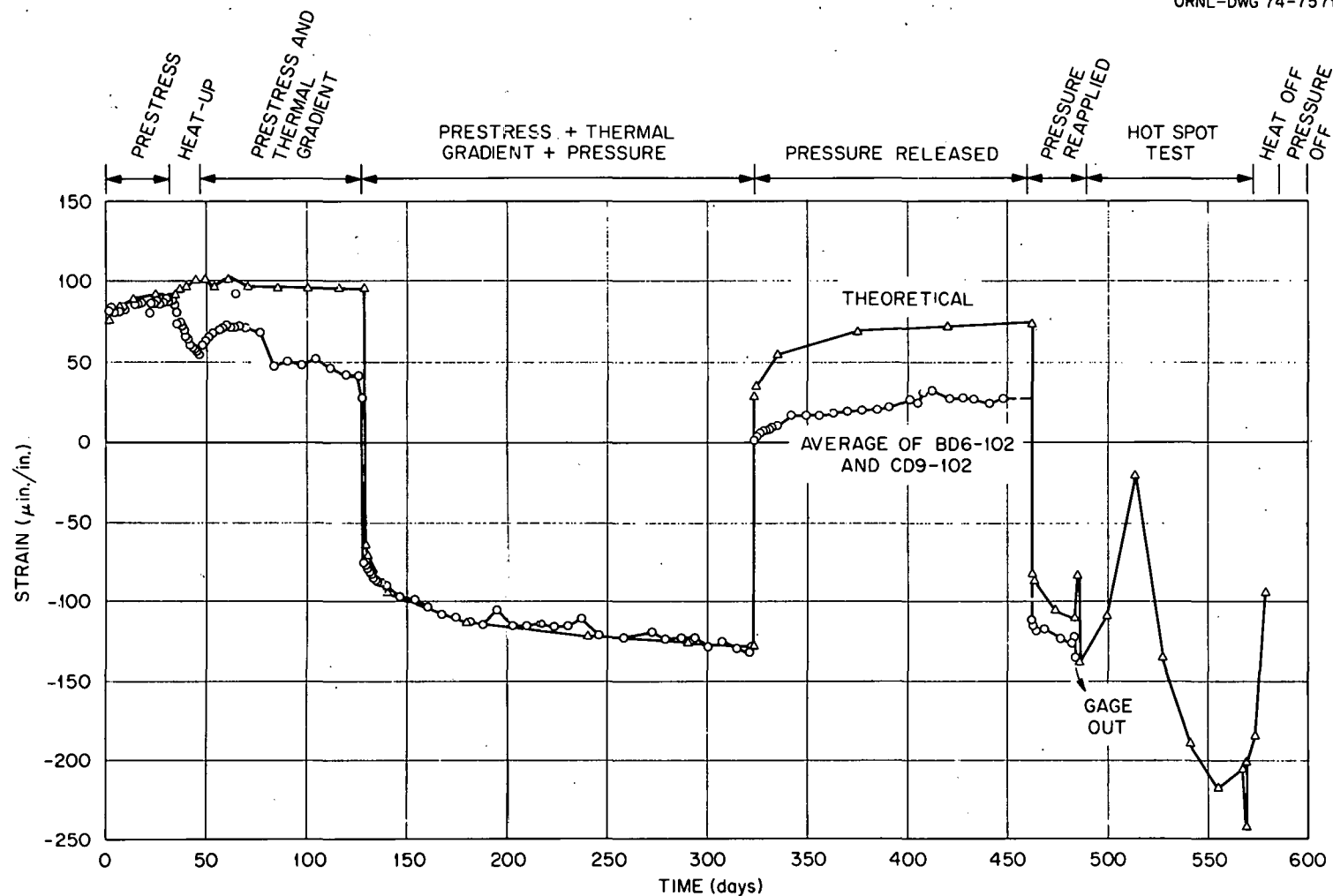
Fig. 6.9. Calculated and experimental results for first-position radial type A vibrating-wire strain gages.
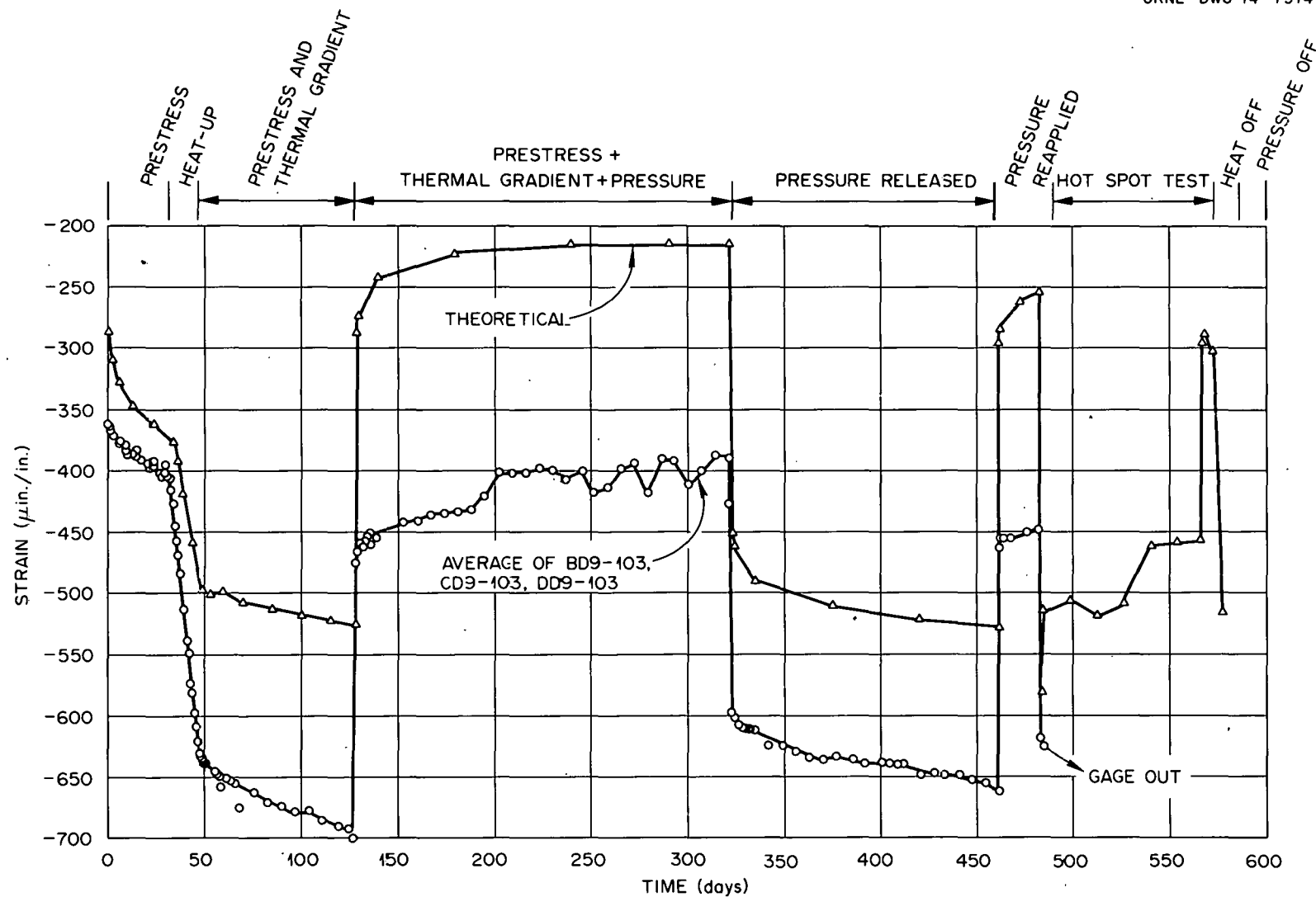
Fig. 6.10. Calculated and experimental results for first-position circumferential type A vibrating-wire strain gages.

cylinder model; that is, there was overestimation by the analyses of pre-stressing and pressurization strains and underestimation of heatup strains. Since the vibrating-wire strain gages will function satisfactorily only at temperatures less than ∿340 K, the gages failed at the beginning of the hot-spot test. The missing data from 240 to 390 days (see Fig. 6.8) was caused by problems with the gage readout equipment. Although four vibra-ting-wire gage positions were used across the test section, the position 3 gage results (shown in Fig. 6.11) can be compared from the behavioral standpoint with the single-filament gage data shown in Fig. 6.5; the same basic differences between experimental and analytical results are seen for both gage types.

Of the nine type B vibrating-wire embedment strain gages used in the model, six continued to operate during the experiment; however, the read-ings in many cases were inconsistent because of problems with the readout equipment. The vibrating-wire gage frequency monitor used for the study was designed specifically for use with type A gages and frequently gave inconsistent readings when used with type B and C gages.

Comparisons for two circumferential type B gages are given in Figs. 6.12 and 6.13 for the first and second gage positions. Although better agreement occurred for prestressing strains, the same basic trends are again seen for this gage type; that is, the calculated strains during pres-sure steps are larger and the heatup strains smaller than the experimental values.

Only one of the type C vibrating-wire strain gages was included in the model. Although this gage is far superior in basic design than the other two types of vibrating-wire gages, it requires precasting to ensure satis-factory performance. (This was not done in this experiment.)

The wound-wire resistance embedment strain gages also failed to per-form satisfactorily, although all but one remained operational during the experiment. (However, the gages of this type used in the companion con-crete specimens functioned satisfactorily.) The unsatisfactory performance of these gages is attributed to the absence of bonding between gage and concrete. It is felt that the present gage deficiency could be corrected with only minor modifications of the bonding surfaces of the gage housing.
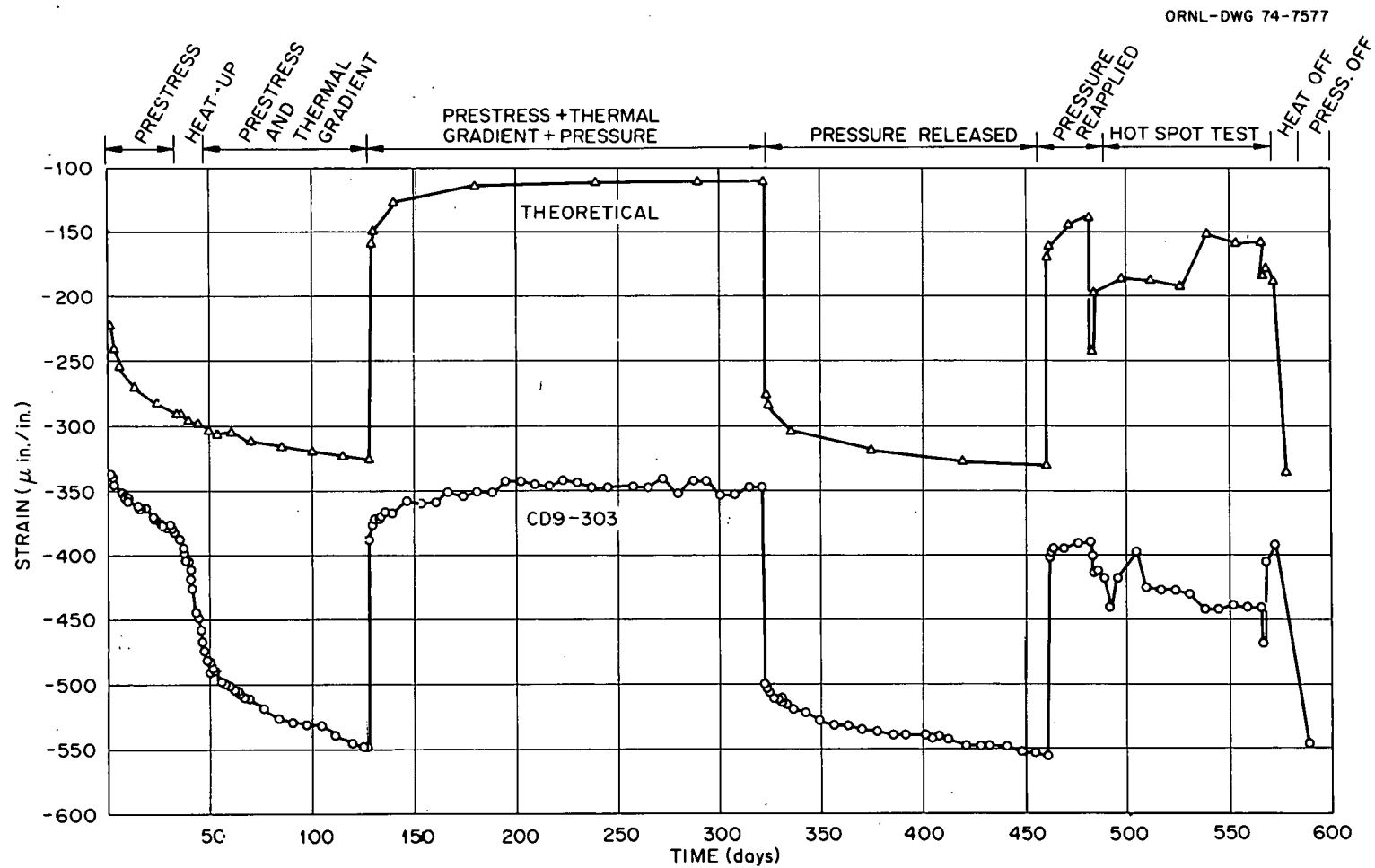
Fig. 6.11. Calculated and experimental results for the third-position circumferential type A vibrating-wire strain gage.
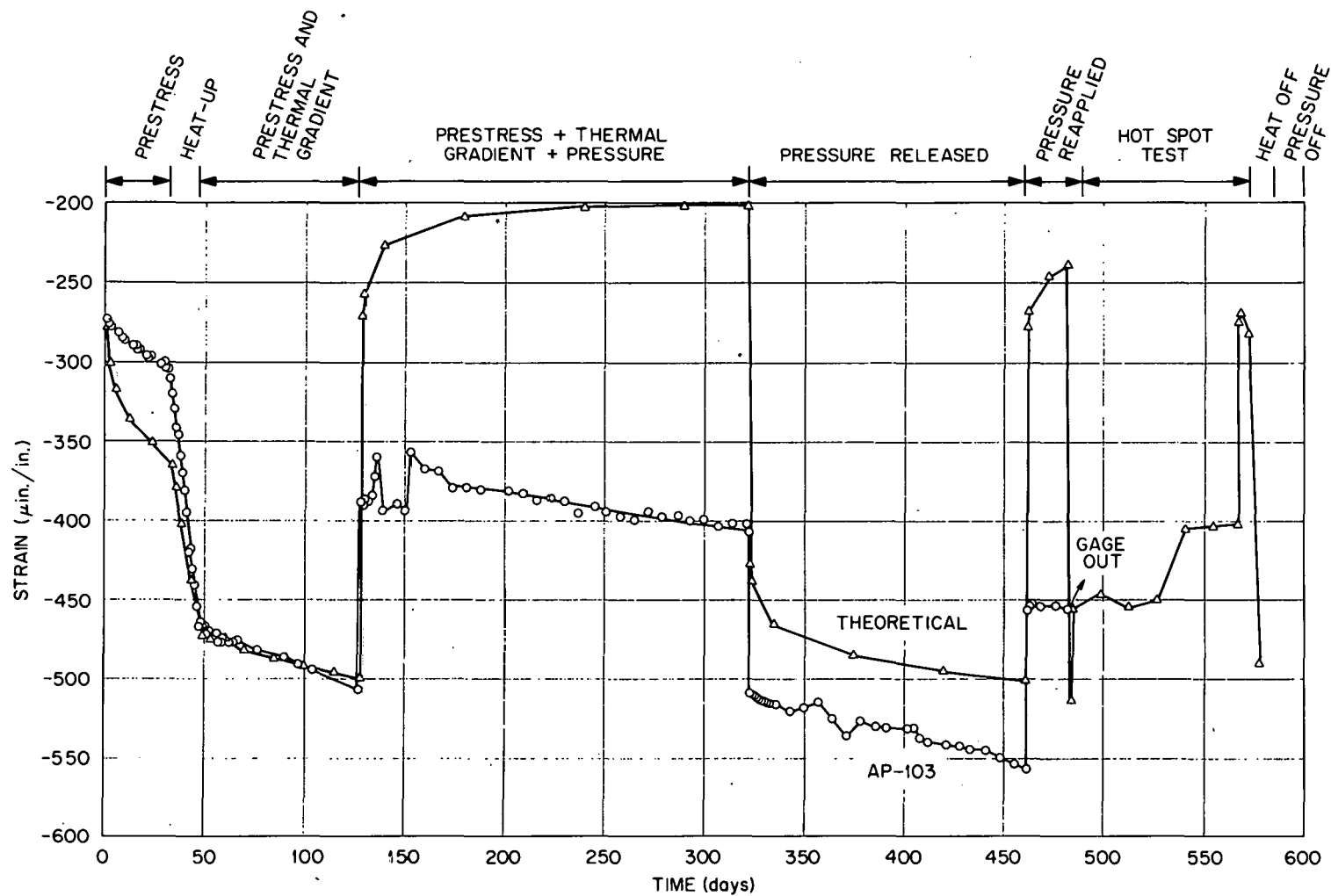
Fig. 6.12. Calculated and experimental results for first-position circumferential type B vibrating-wire strain gage.
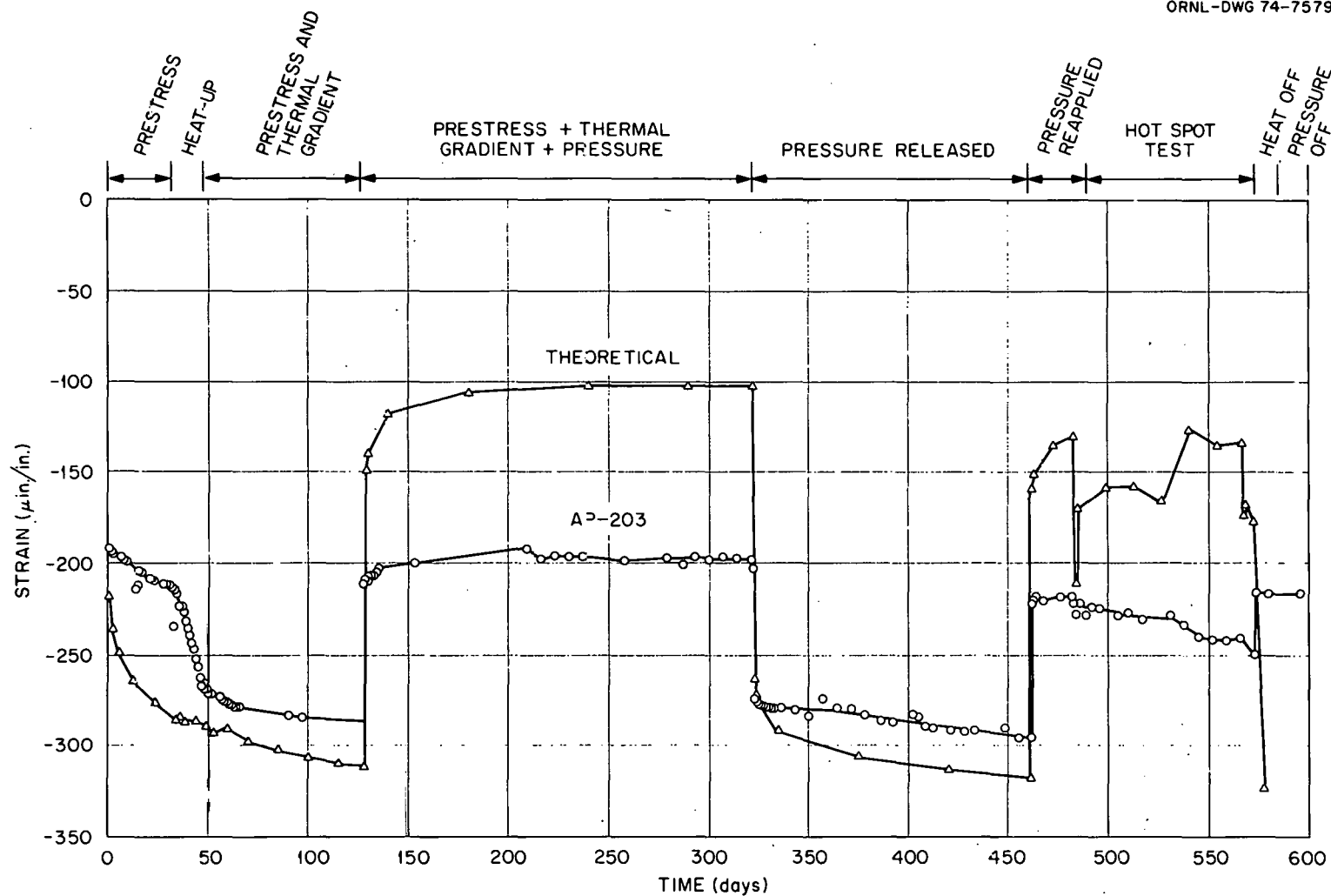
Fig. 6.13. Calculated and experimental results for second-position circumferential type B vibrating-wire strain gage.

6.2 Stress Cells

Experimental and calculated stresses for three circumferentially oriented titanium stress cells are shown in Figs. 6.14 to 6.16 for the first, second, and fourth positions of Fig. 2.1, respectively. These cells functioned satisfactorily until after the initial pressurization loading. Cell 253 performed spasmodically from that point until the pressure was released, and cell 4-11-3 monitored an unexplainable stress drop at 360 days. This test was the first attempt to use a stress cell of
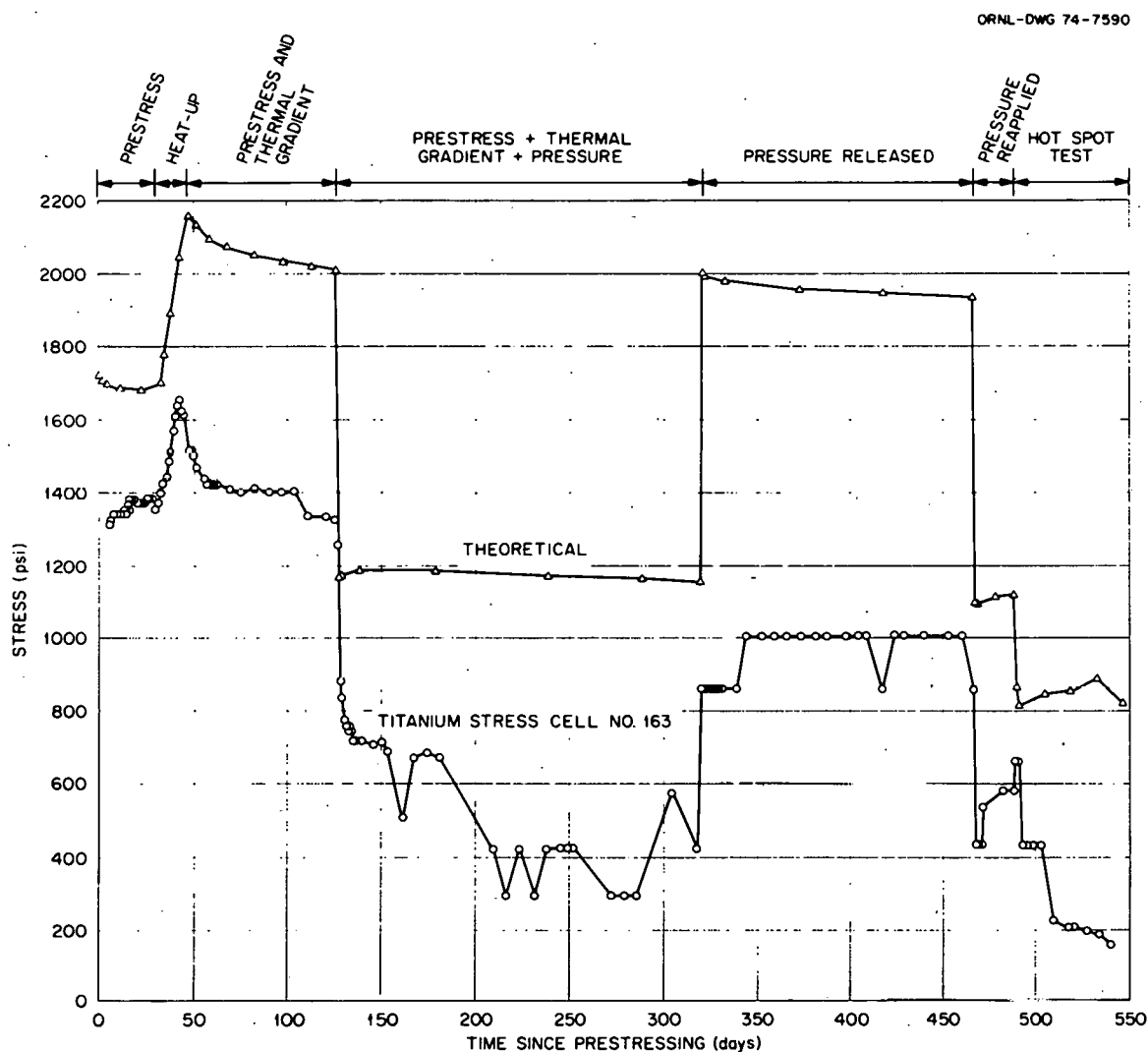

Fig. 6.14. Calculated and experimental results for first-position circumferential titanium stress cell (1 psi = 6895 Pa).
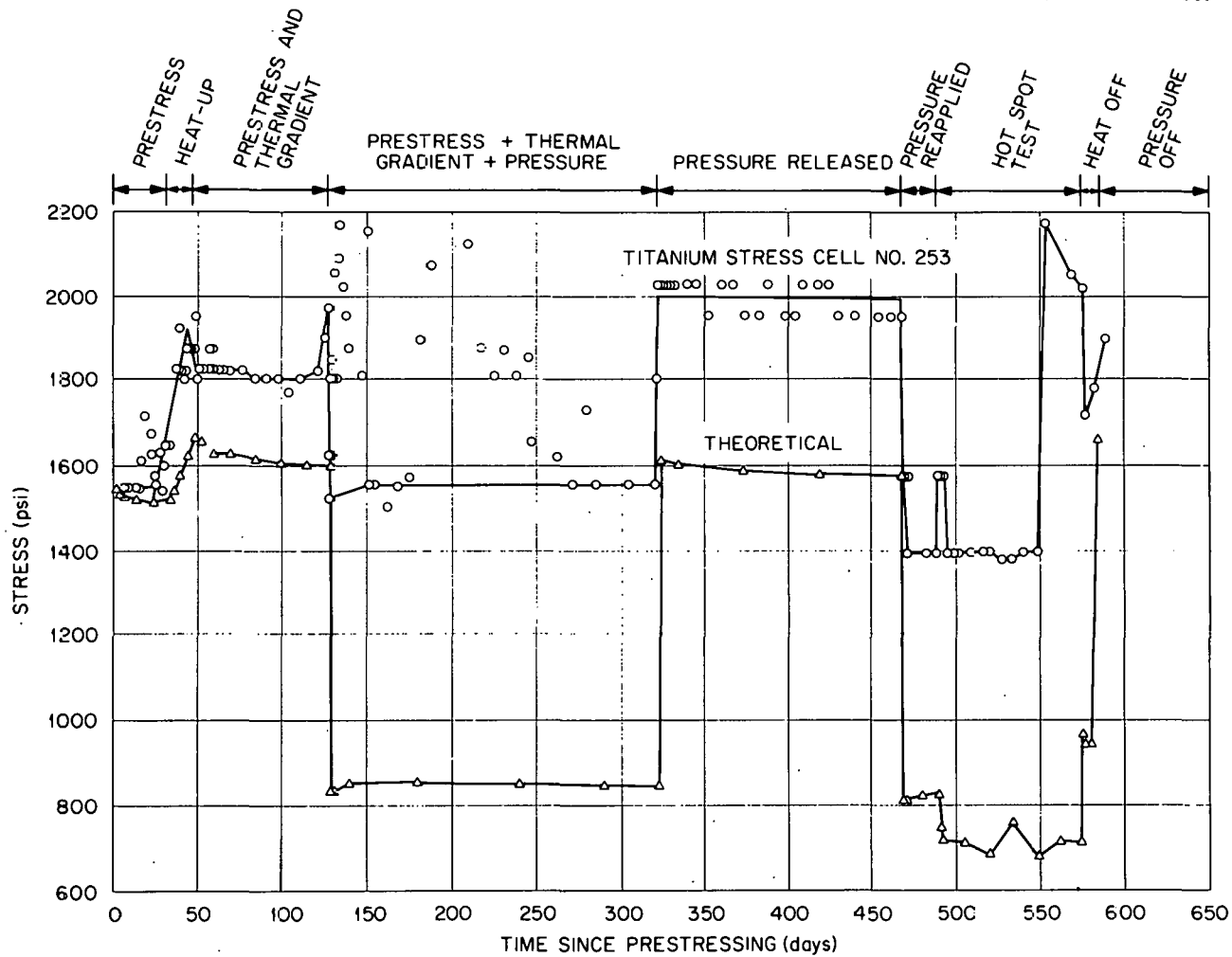
Fig. 6.15. Calculated and experimental results for second-position circumferential titanium stress cell (1 psi = 6895 Pa).
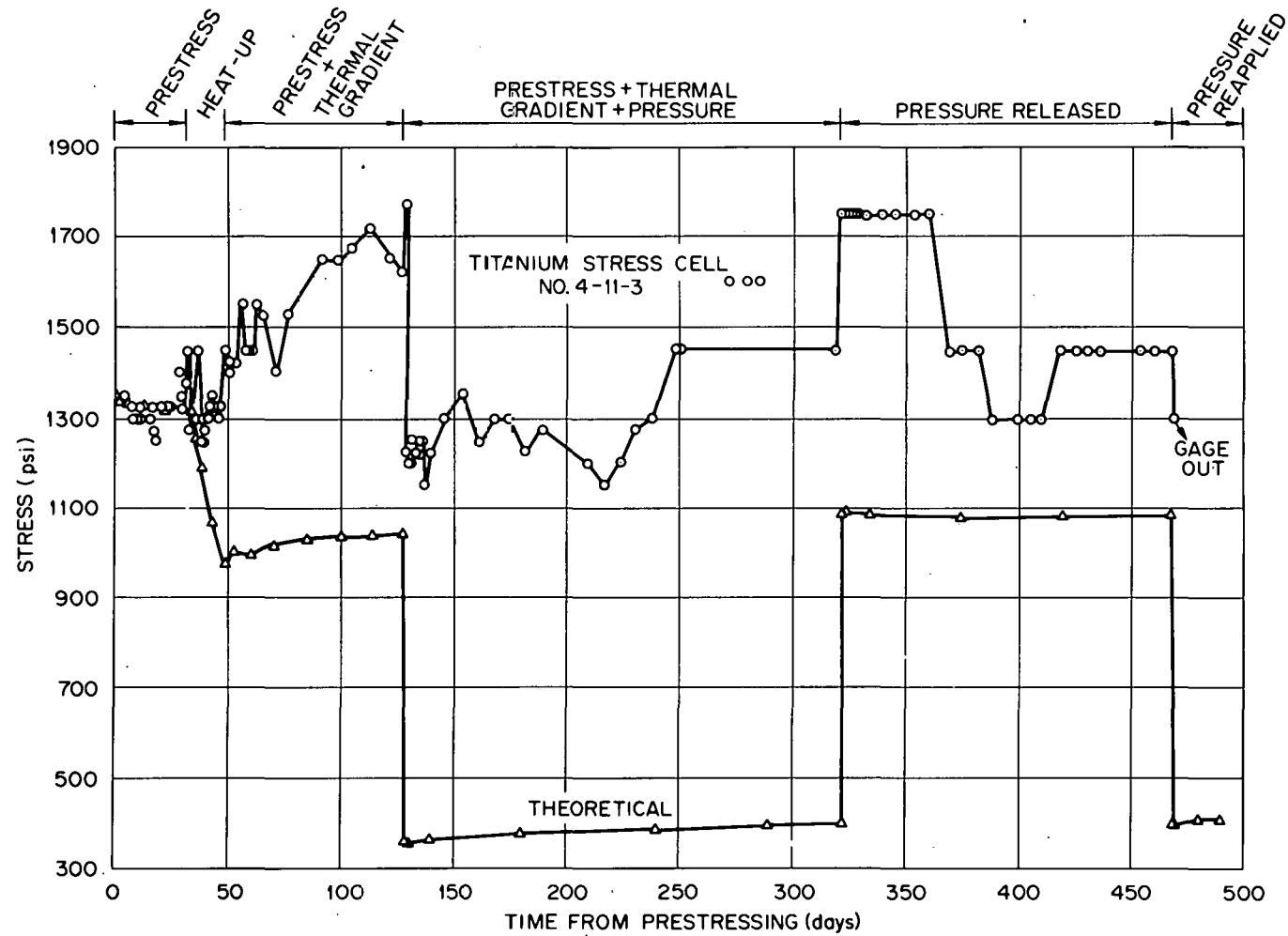
Fig. 6.16. Calculated and experimental results for fourth-position circumferential titanium stress cell (1 psi = 6895 Pa).

this particular design; further refinement will be required to ensure reliability and long-term stability.

The pressure diaphragm type of stress cell consists of two single-filament embedment strain gages positioned in parallel in uniform stress locations, with one having a relatively thin sheet-metal pressure diaphragm attached. The stress is determined by measuring the applied diaphragm pressure required to balance the strain readings of the two gages. Although this technique appeared capable of measuring stresses developed during short-term loading (see following discussion of companion specimen tests), it was incapable of determining time-dependent stresses in the thermal cylinder model. To do this would require individual diaphragm pressure control and strain gage readout systems.

6.3 Liner Strain

The calculated and experimental strains for axial and circumferential weldable strain gages are shown in Figs. 6.17 and 6.18 for the concrete and annulus sides, respectively, of the inside heat exchanger (heat exchanger B). The same general observation made for the embedment instrumentation also applies to these gages; that is, except for the hot-spot test, the strains produced by mechanical loadings were slightly overestimated by the analysis and those produced during heatup were underestimated. The sharp flucuations in calculated results noted previously for the embedment gages during hot-spot heating were not seen on the liner, but the greatest disagreement occurred during the hot-spot test. This was especially true in the case of the circumferential gage.

Comparisons for the weldable gages located on the annulus side of the heat exchanger or liner (Fig. 6.18) show considerably greater disagreement. This trend was consistent for all four sets of liner gages. The strains produced by heatup were considerably distorted; however, pressurization strains were consistent with the readings for the concrete side. A final check of the gages on both sides showed that the resistance of the gages on the annulus side, which were not equipped with integral leads, changed during the experiment, whereas the resistance of the gages on the concrete side, which were equipped with integral leads, remained unchanged. It was
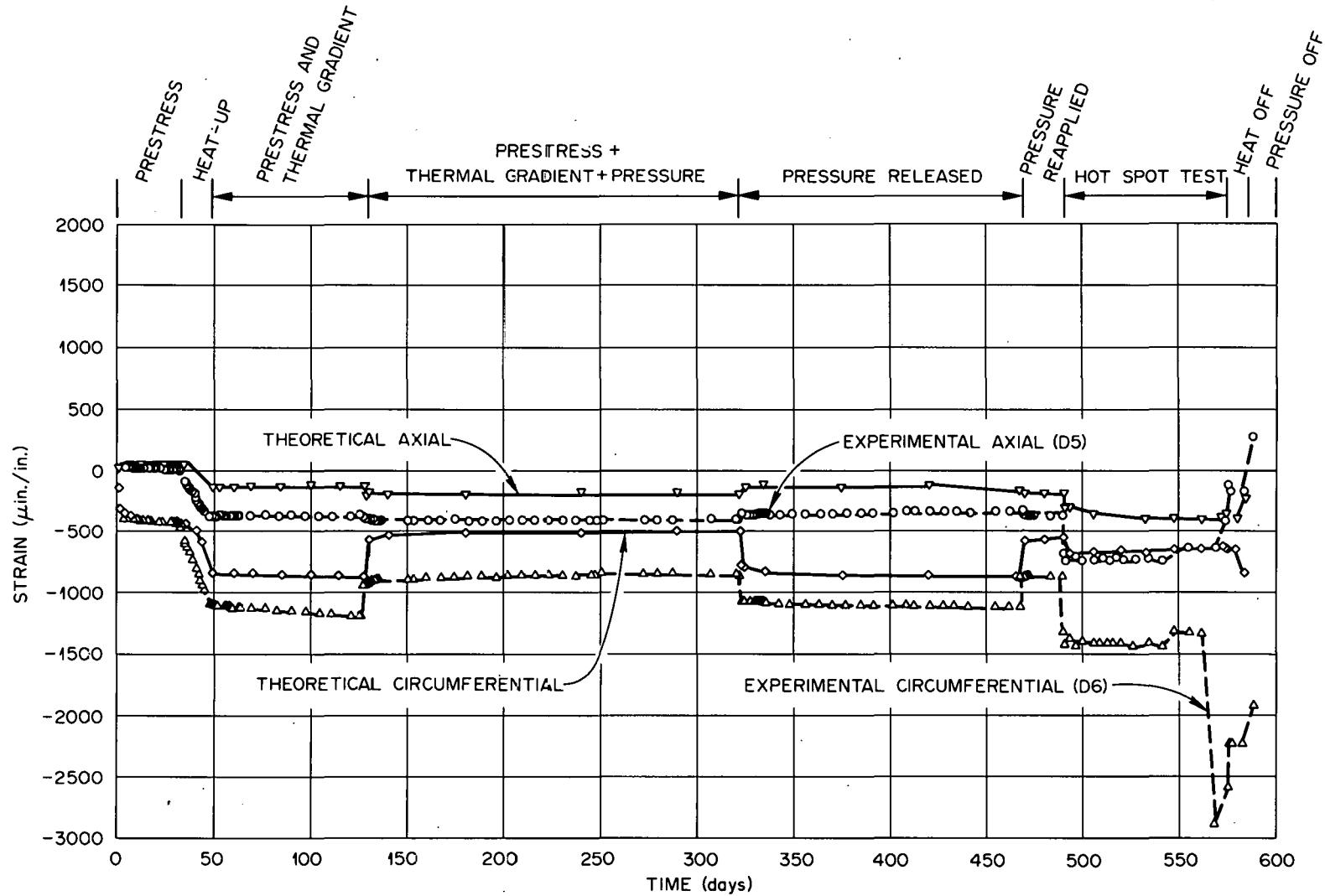
Fig. 6.17. Calculated and experimental results for axial and circumferential weldable strain gages attached to the concrete side of B heat exchanger.
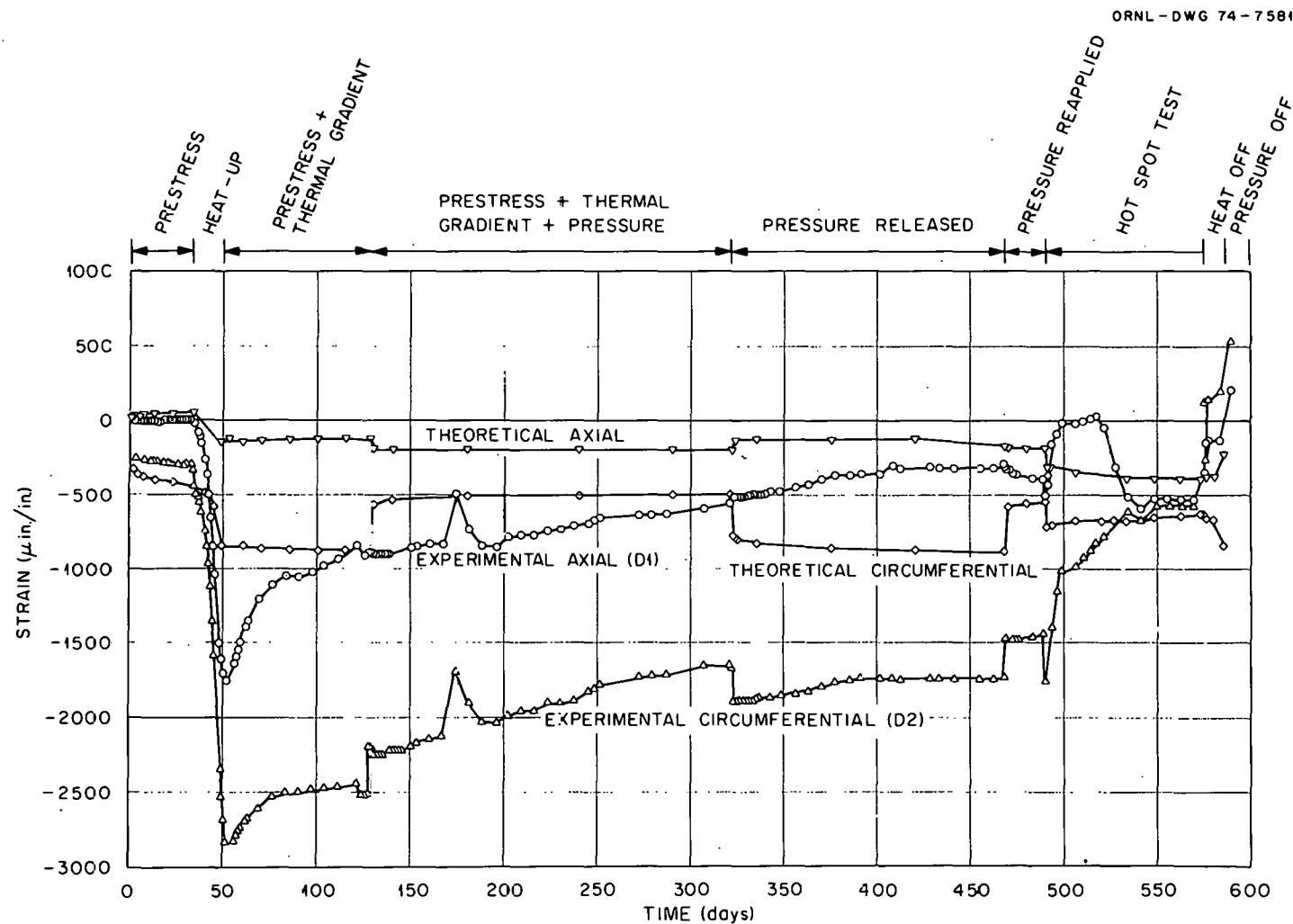
Fig. 6.18. Calculated and experimental results for axial and circum-
ferential weldable strain gages attached to the annulus side of B heat
exchanger.

concluded from this behavior that the gage data shown in Fig. 6.17 represented the behavior of the heat exchanger and that the strain distortions seen in Fig. 6.18 resulted from instrumentation problems rather than from liner behavior.

The results for weldable gages attached at the level of the hot-spot heaters are shown in Fig. 6.19, along with plots for circumferential gages attached to both sides of the heat exchanger for comparison. Although the strains during hot-spot heating were much greater than those shown in Fig. 6.17, the same general trend is seen; however, in this case, the circumferential gage did not exhibit the previously noted strain jump toward the end of the hot-spot heating period.

6.4 Tendon Instrumentation

Individual strands of 12 axial and 8 circumferential prestressing tendons were instrumented with conventional foil-type resistance strain gages, and compression load cells were attached in series with the axial tendons. Results for three axial tendon strain gages are shown in Fig. 6.20. The inner-row tendon gage CCB-3 apparently suffered a bonding failure prior to prestressing and must therefore be discounted. The two outer-row tendon gages, positioned as shown in the small inset of Fig. 6.20, indicated stable conditions until initiation of the hot-spot test. At that time, gage CCB-2 showed a gradual decrease in strain followed by a distinct downward jump. The load-vs-time plot of axial tendon load cell CTR-2 is shown in Fig. 6.21. This transducer, which was attached to the CCB-2 instrumented tendon, indicated a stable loading during the hot-spot heating period. It is therefore doubtful that the strain gage recorded the actual tendon behavior. On the other hand, load transducers CTR-1 and CTR-3, which were coupled to inner-row tendons, measured periodic step-load drops during the experiment. Recent postmortem studies yielded strong evidence that the load changes were produced by progressive corrosion failure of inner-row tendons. The corrosion problem is discussed in Chap. 7.

Strain gage data for two circumferential temdons are shown in Fig. 6.22. In contrast to the axial tendons, the circumferential tendons were located outside the concrete test section and were constrained, as shown in Fig.
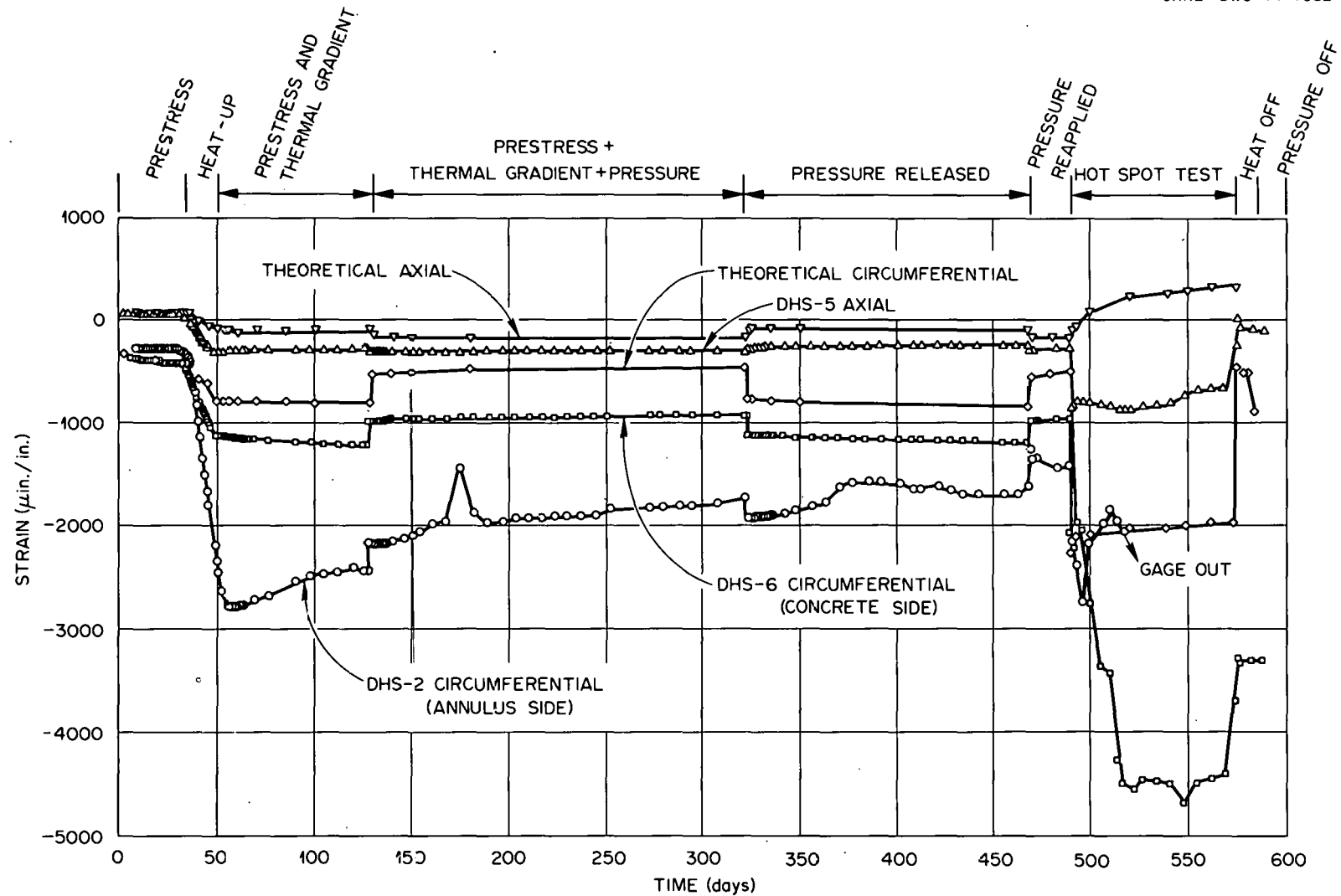
Fig. 6.19. Calculated and experimental results for axial and circumferential weldable strain gages attached to concrete side and for circumferential gage attached to annulus side of B heat exchanger.
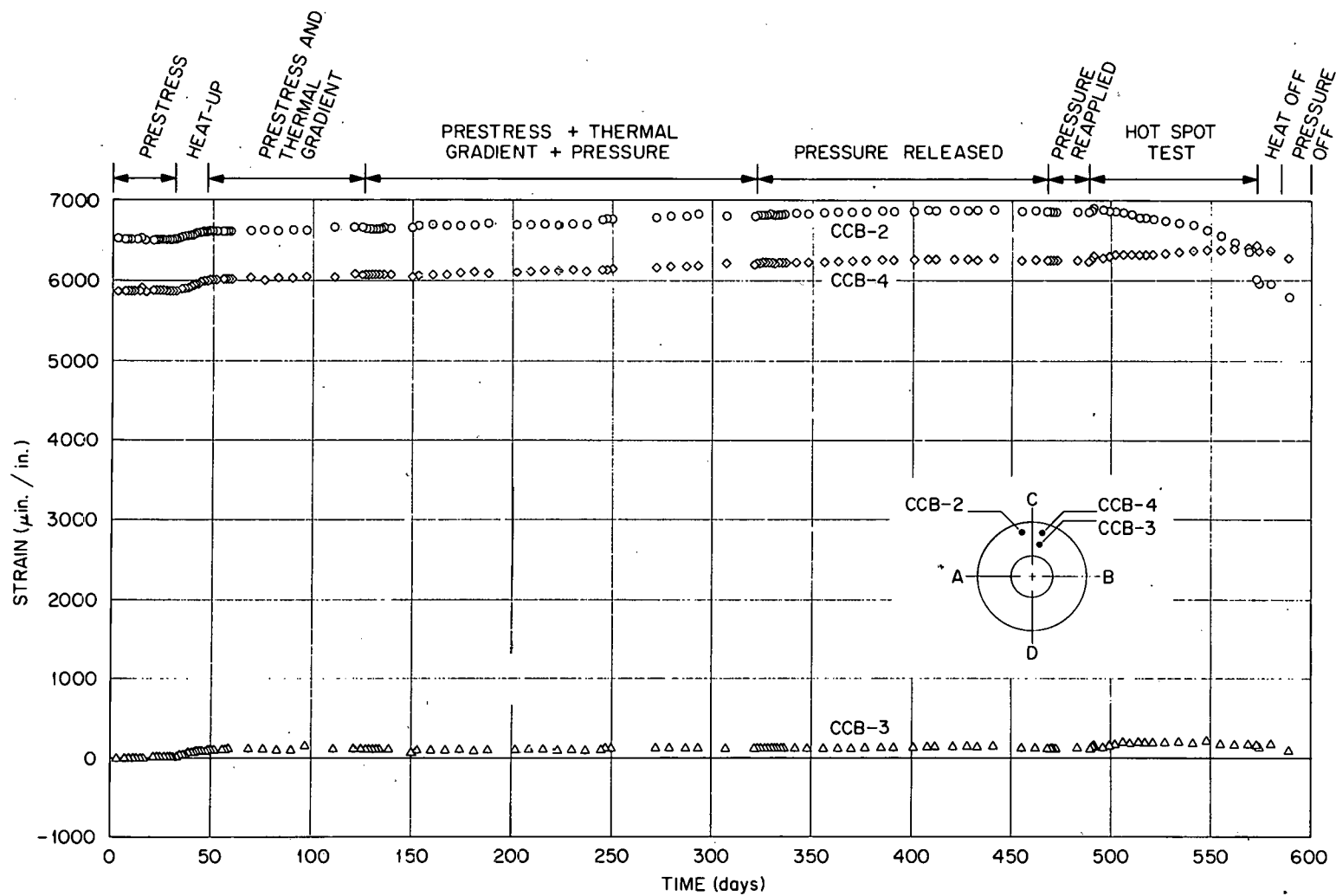
Fig. 6.20. Experimental results for foil-type strain gages attached to axial prestressing tendcns.
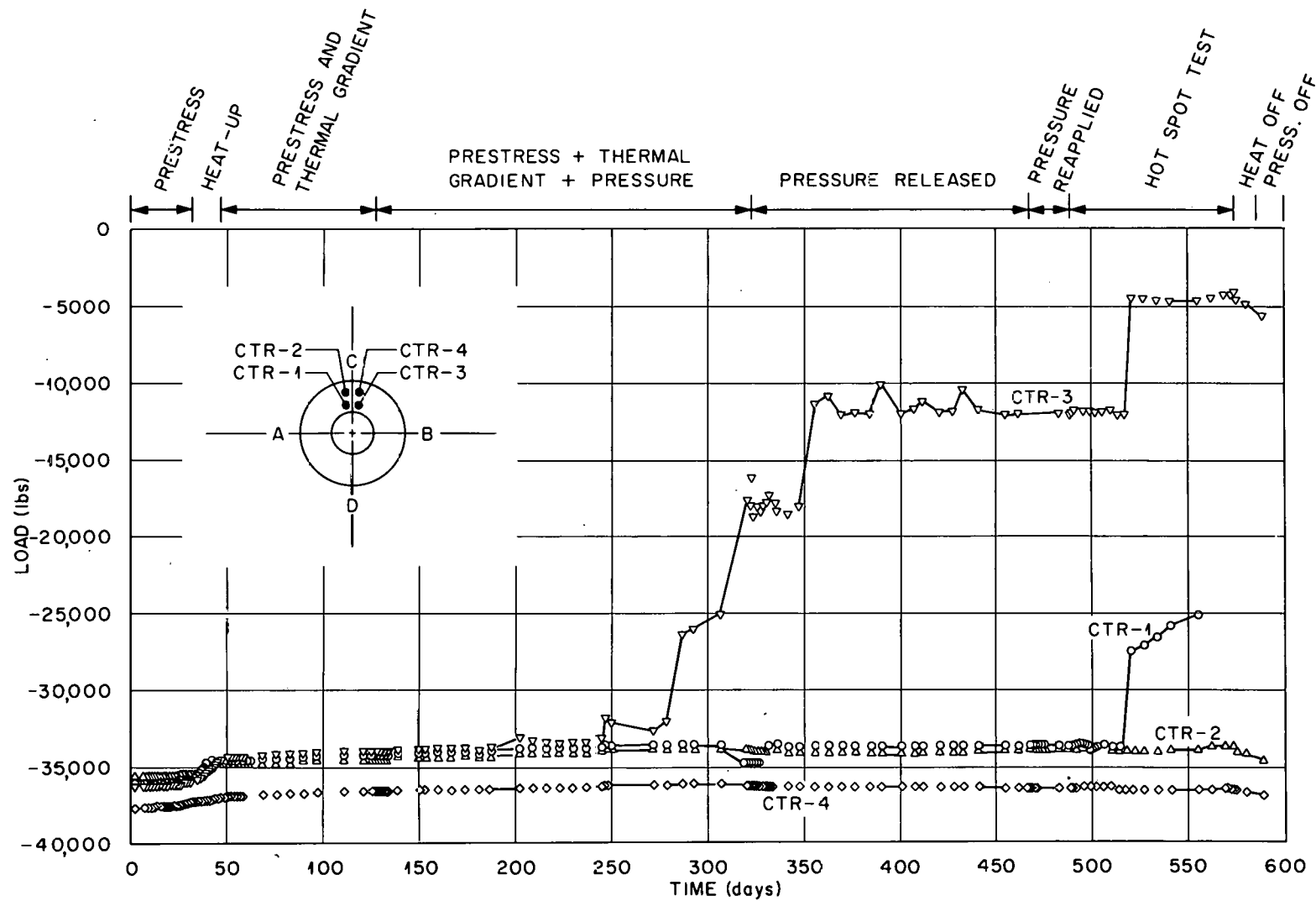
Fig. 6.21. Experimental results for load cells coupled to axial pre-stressing tendons (1 lb = 4.448 N).

Fig. 6.22. Experimental results for foil-type strain gages attached
to circumferential prestressing tendons.

4.3. Based on the strain gage data, the circumferential tendons apparently performed satisfactorily.

6.5 Moisture Measurements

The results of the probe-type neutron and gamma-ray backscattering instrument calibration tests are shown in Fig. 6.23. Inconsistencies were found between the recorded weights and the probe readings of the specimens subjected to 100% relative humidity when compared with those from the remaining nine specimens; consequently, only two sets of these r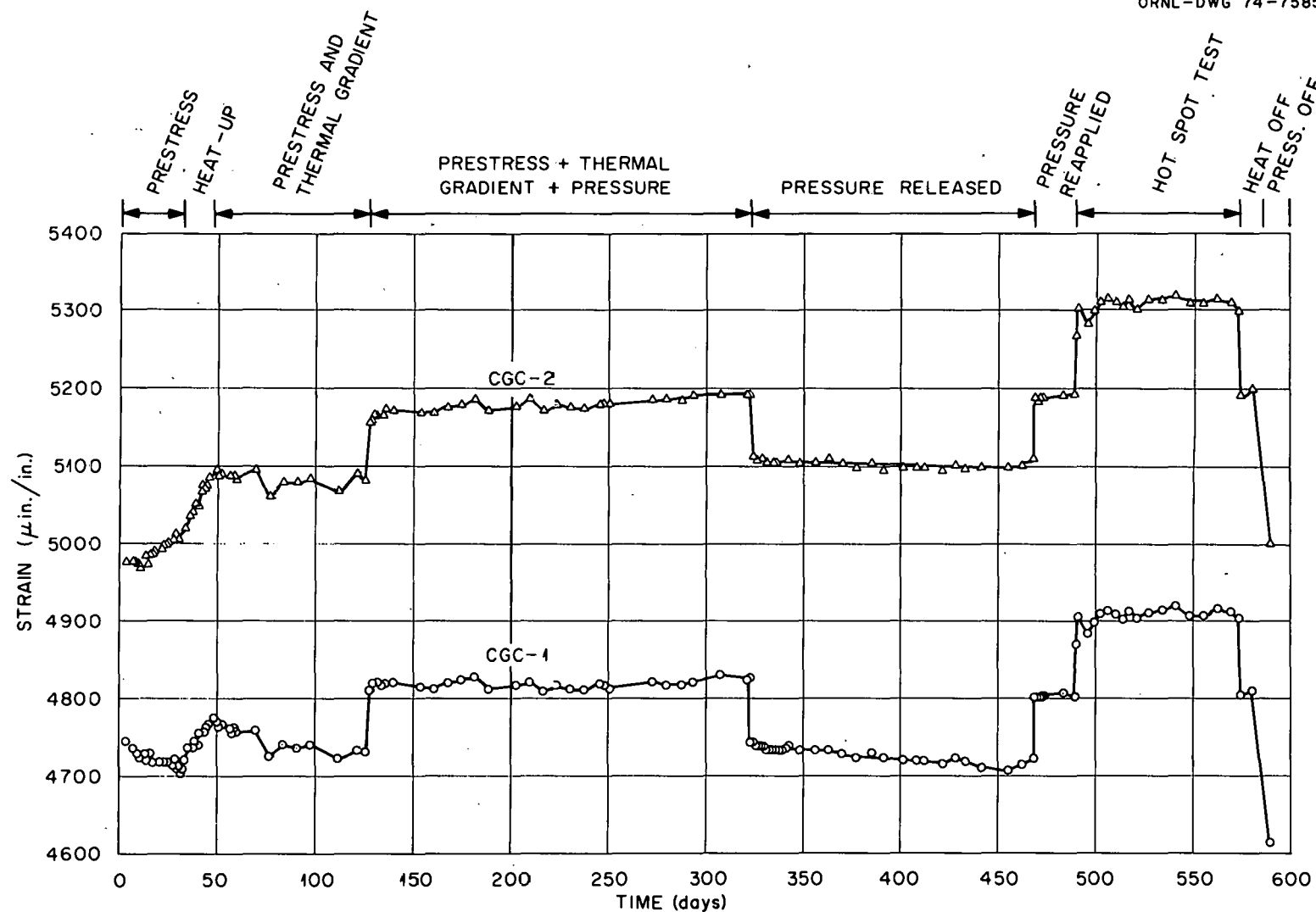eadings are shown in the figure. No discernible difference was seen between the rates of moisture loss in the remaining three sets; the average values are shown in Fig. 6.23. Of the two curves shown, the upper curve and data points represent total moisture content (based on calculated dry weight), and the lower curve represents evaporable moisture content (based on oven-dried specimen weight). The circled data points on both curves represent the moisture content measured using a 0.3- by 0.3- by 0.3-m specimen cut from the thermal cylinder model.

This scaling factor was then used to reduce the thermal cylinder moisture probe counts, or readings, to the values shown in Table 6.2. From left to right in the table, the positions extend raidally from near the center of the core (designated as 3.81 cm) to the three positions located in the test section. The 69.9-cm position is nearest the 338.7 K surface and the hot-spot heater; the 77.5-cm position is in the center of the test section; and the 88.9-cm position is located nearest to the 297 K surface, which is the outer surface of the section. In most cases, each value listed in the table represents the average of nine 1-min counts, which are taken in sets of three at each of three levels in the cylinder.

Initially, little variation is seen in the readings for the various radial positions in the cylinder, which indicates that the moisture seal was effective and little migration of moisture resulted from the heating. The intensive heating during the hot-spot test resulted in excessively high counts at 614 days. Only those readings that appeared to be relatively unaffected by the heating are shown in Table 6.2; however, the high reading shown for the center of the core was caused by heating of the moisture probe.
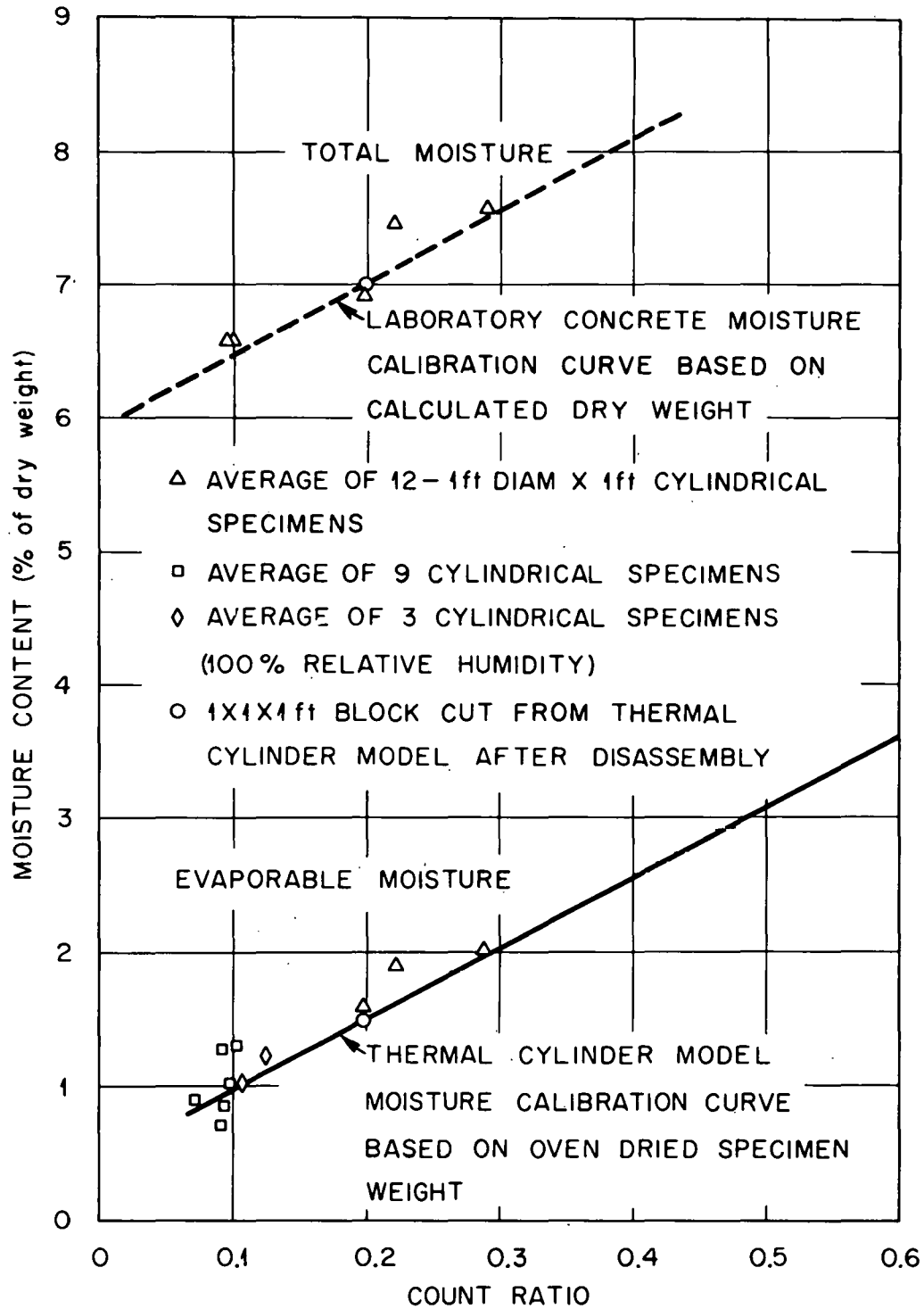
ORNL-DWG 74-7565

Fig. 6.23. Total and evaporable moisture-content calibration curves for ORNL thermal cylinder concrete having 7.59% as-cast total moisture content (1 ft = 0.3048 m).

Table 6.2. Average evaporable moisture content (% of oven-dried weight) for various radial positions in ORNL thermal cylinder model

| Days since prestressing | Radial distance from center [cm (in.)] | | | | | | Status of test section |
| | 1.05-m-diam (41.5 in.) core | | | 2.06-m-OD (81-in.) test section [0.46 m (18 in.) thick] | | | |
	3.8 (1.5)	20.3 (8.0)	29.4 (15.5)	69.9 (27.5)	77.5 (30.5)	88.9 (35)	
130		1.47	1.44	1.41	1.40	1.37	297 K (75°F) inside, 297 K (75°F) outside
135	1.48	1.53	1.46	1.45	1.46	1.44	314 K (105°F) inside, 297 K (75°F) outside
146	1.49	1.53	1.46	1.47	1.46	1.45	339 K (150°F) inside, 297 K (75°F) outside
175	1.51	1.55	1.48	1.47	1.49	1.47	339 K (150°F) inside, 297 K (75°F) outside
223	1.51	1.55	1.47	1.46	1.48	1.47	339 K (150°F) inside, 297 K (75°F) outside, before pressurization
236	1.47	1.51	1.46	1.44	1.46	1.45	339 K (150°F) inside, 297 K (75°F) outside, pressurized to 4.83 MPa (700 psi)
318	1.51	1.54	1.47	1.47	1.48	1.47	Same as for 236 days
403	1.54	1.57	1.52	1.44	1.46	1.44	Same as for 236 days
425	1.54	1.58	1.53	1.44	1.45	1.43	339 K (150°F) inside, 297 K (75°F) outside, pressure released
614	a	a	c	1.65[c]	1.52	1.48	Repressurized to 4.83 MPa (700 psi) and subjected to 505 K (450°F) hot-spot heating
686	1.20	1.31	1.20	1.46	1.50	1.50	After cooldown to 339 K (150°F) inside, 297 K (75°F) outside, at pressure
718	1.23	1.29	1.19	1.43	1.48	1.48	After complete cooldown to 297 K (75°F) inside, 297 K (75°F) outside, and pressure released

[a]Readings appreciably influenced by heating during hot-spot test.

Since the moisture probe was found to be temperature sensitive, the increases in values coinciding with temperature changes to which the model was subjected are the result of the temperature increases. If these temperature effects are taken into consideration, it can be concluded that the copper-epoxy moisture seal was adequate for conditions simulating normal PCRV operation. An examination of the moisture readings made in the core region after the hot-spot test shows that a small amount of moisture was lost during heating. This is a reasonable conclusion based on the measured temperature profiles, which show that a large portion of the core was subjected to temperatures of 352.6 to 366.5 K.

A similar examination of probe readings for the model test section indicates that moisture content remained constant during and after the hot-spot test. It should be noted that a relatively small portion of this test section was subjected to elevated temperatures during the hot-spot heating; in fact, a fairly large portion of the section was cooled to temperatures of 311 K or lower, which should account for the differences of moisture content in the core and test ring. There is also little evidence of appreciable migration of moisture from inside to outside of the test section during the course of the experiment except for the readings made after the hot-spot heating, which show a slight increase in moisture in the two outer probe positions in comparison with the innermost position.

Although it is difficult to make any meaningful comparison between the moisture content of the model and that of the relatively small moisture calibration specimens, values can be used to provide an order-of-magnitude evaluation. At 28 days, the average moisture content of the specimens at 100% relative humidity was 1.89%, while the average moisture content of the specimens subjected to the three lower relative humidities was 1.30%. In comparison, the moisture content for the thermal cylinder model at 227 days (130 days after prestressing) was 1.42%.

6.6 Companion Specimen Tests

Two 0.46- by 1.02-m concrete cylinders were instrumented with every type of embedment stress and strain measuring device employed in the thermal cylinder in order to provide a better understanding of basic gage

behavior. These companion test cylinders were cast, sealed, and heated, and one was loaded uniaxially in accordance with the time schedule of the large model. Both cylinders were maintained at a temperature of 338.7 K during the time-dependent portion of the study. Cylinder M-1 was subjected to a 24.8-MPa uniaxial loading 56 days from the time of thermal cylinder model prestressing, and cylinder M-2 remained unstressed during the model testing period. The unabridged strain history of the companion specimen single-filament resistance strain gages is shown in Fig. 6.24. The axial gages in both cylinders experienced excessive drift quite early in the experiment, and the unstressed M-2 cylinder lateral gage began drifting severely at 420 days. On the other hand, the stressed M-1 specimen lateral gage performed consistently for the duration of the experiment. The excessive number of gage failures was probably caused by the relatively high temperatures to which these gages were subjected.

In addition to the sustained testing period, the M-1 specimen was loaded and unloaded in steps both at 297 and 338.7 K; the M-2 specimen was also load tested for short time periods at 297 K to provide additional gage data. Typical stress-vs-strain plots for these short-term tests are shown in Figs. 6.25 and 6.26 for axial single-filament resistance gage M1-SEB-111 and type B vibrating-wire gage M2-P-101, respectively. The concrete properties obtained for the operating gages of each type are shown in Table 6.3, where the final values are average 180-day strength test results for moist-cured 15.2- by 30.5-cm cylinders. Since the much larger companion specimens were sealed to prevent moisture loss and were at least 180 days of age, the 180-day compressive strength test data were used as the basis for comparison of gage performance. The 338.7 K data were obtained after approximately 550 days of heating; consequently, the modulus of elasticity should be slightly higher than the 180-day value. All the gages could not be evaluated because of premature failure of some of the companion specimen gages; however, certain conclusions can be drawn based on the available data.

The single-filament resistance and type B vibrating-wire embedment gages gave the most accurate readings. The wound-wire resistance gages also performed satisfactorily at both temperatures, which was surprising since the thermal cylinder model gages of this type were unsatisfactory.
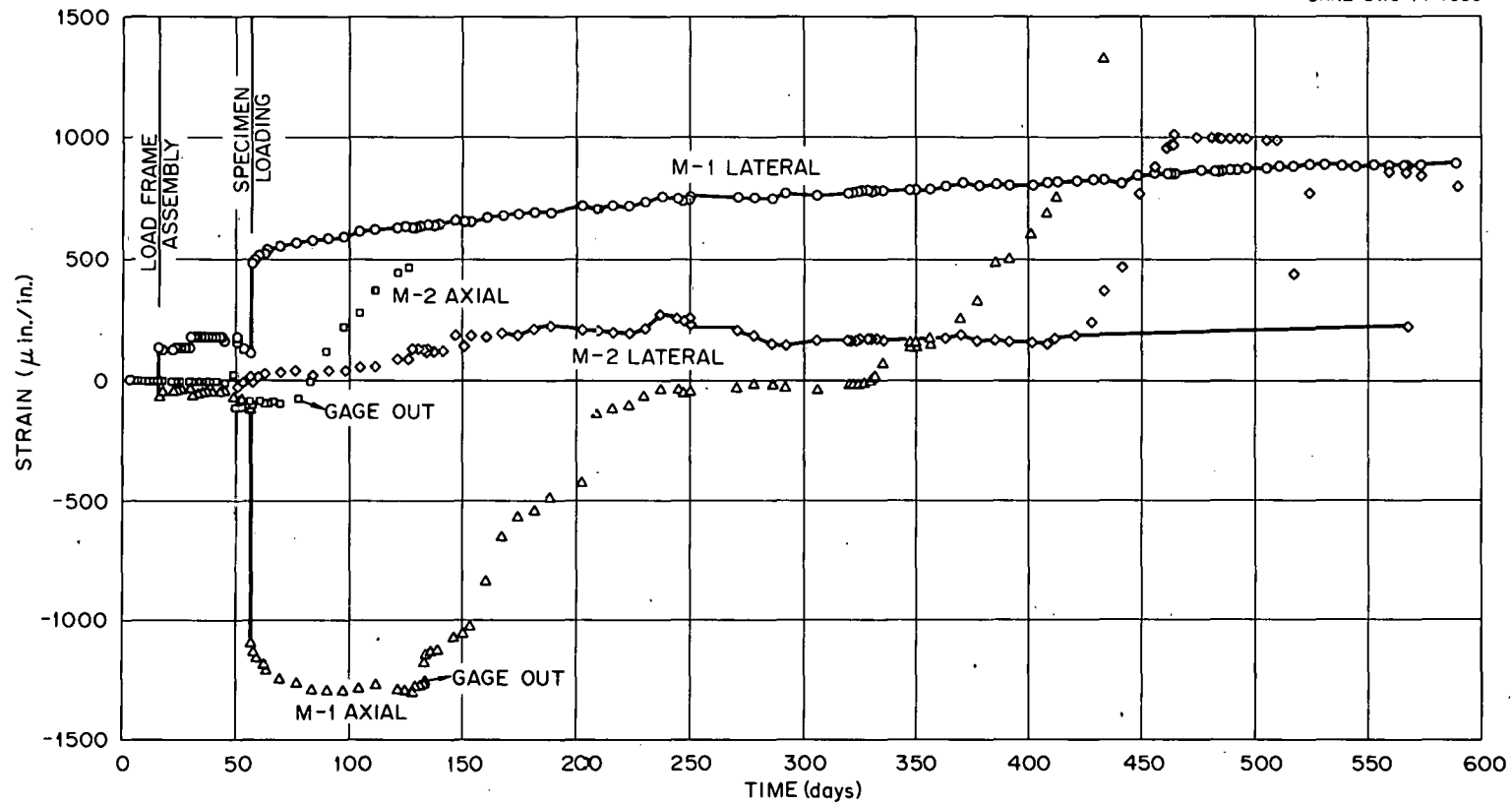
Fig. 6.24. Experimental results for axial and lateral single-filament resistance strain gages of stressed M-1 and unstressed M-2 companion concrete cylinders.
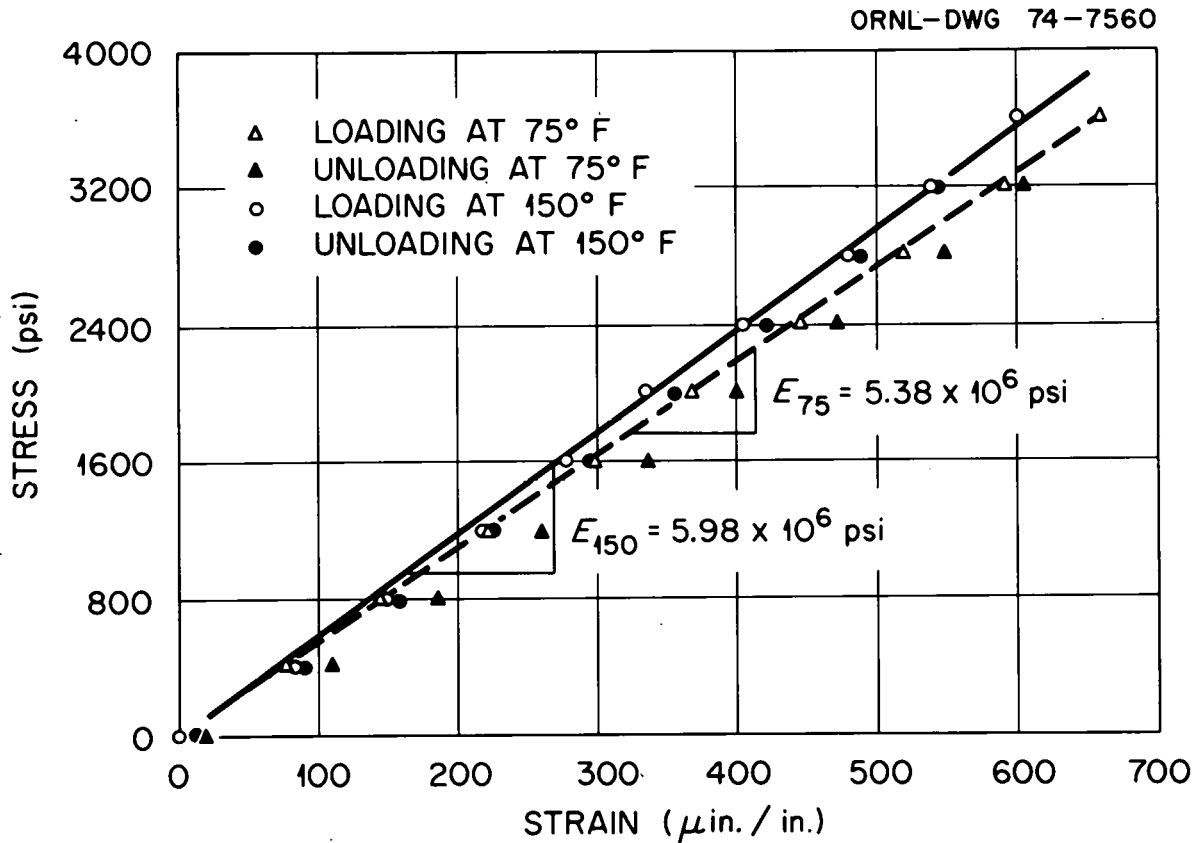
Fig. 6.25. Results of short-time M-1 specimen load test for axial single-filament resistance strain gage [1 psi = 6895 Pa; K = 273.15 + 5/9 ($^\cap$F − 32)].

The type C vibrating-wire gage gave reasonable results at room temperature, but the 338.7 K readings for this gage were significantly low.

The surface resistance gages listed in Table 6.3 were experimental gages developed as part of the ORNL biaxial creep test apparatus.[8] Three gages were attached to pairs of small steel posts protruding from the surface of each cylinder at equal angular spacing. Although these gages were not operational during the room-temperature test, they performed satisfactorily at 338.7 K.

The results of the uniaxial compression testing of the titanium stress cell are shown in Fig. 6.27. In addition to the companion specimen tests of the embedded gages, each stress cell was load-calibrated under uniaxial compression. The results indicated that the embedded stress cell readings must be multiplied by 1.19 to obtain the actual stress in the concrete.
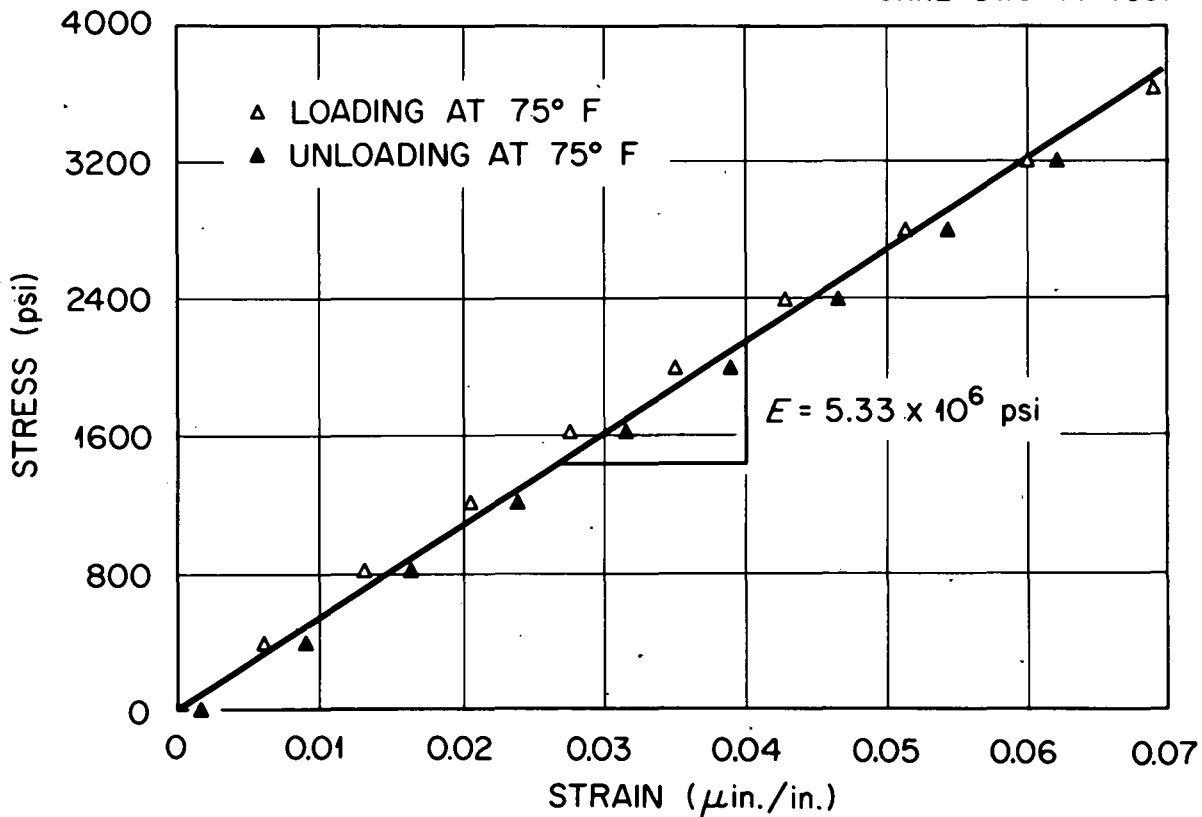
Fig. 6.26. Results of short-time M-2 specimen load test for axial type B vibrating-wire strain gage [1 psi = 6895 Pa; K = 273.15 + 5/9 (°F − 32)].

We also attempted to monitor the embedded pressure stress cells during the companion specimen tests, but owing to a need for additional and more sophisticated instrumentation, we were able to obtain only the following three readings:

Actual stress [MPa (psi)]	Stress cell pressure [MPa (psi)]	Percent deviation
2.77 (402)	4.83 (700)	74
5.48 (795)	10.34 (1500)	89
25.28 (3666)	28.96 (4200)	15

The pressure stress cell was able to determine the maximum specimen stress to within 15%, but was unable to measure the lower stress levels to a reasonable accuracy.

Table 6.3. Companion specimen compression test results

Gage type	Modulus of elasticity [GPa (10^6 psi)]		Poisson's ratio
	297 K (75°F)	339 K (150°F)	
0.46- by 1.02-m (18- by 40-in.) cylinders			
Single-filament resistance	37.09 (5.38)	41.23 (5.98)	
Type B vibrating-wire	36.75 (5.33)		0.24
Type C vibrating-wire	32.20 (4.67)	32.68 (4.74)	
Wound-wire resistance	33.78 (4.90)	44.13 (6.40)	0.31
Surface resistance		40.00 (5.80)	
15.2- by 30.5-cm (6- by 12-in.) concrete strength cylinders			
Surface resistance[a]	37.23 (5.40)		0.28

[a]See Table 4.1 for additional concrete strength data.

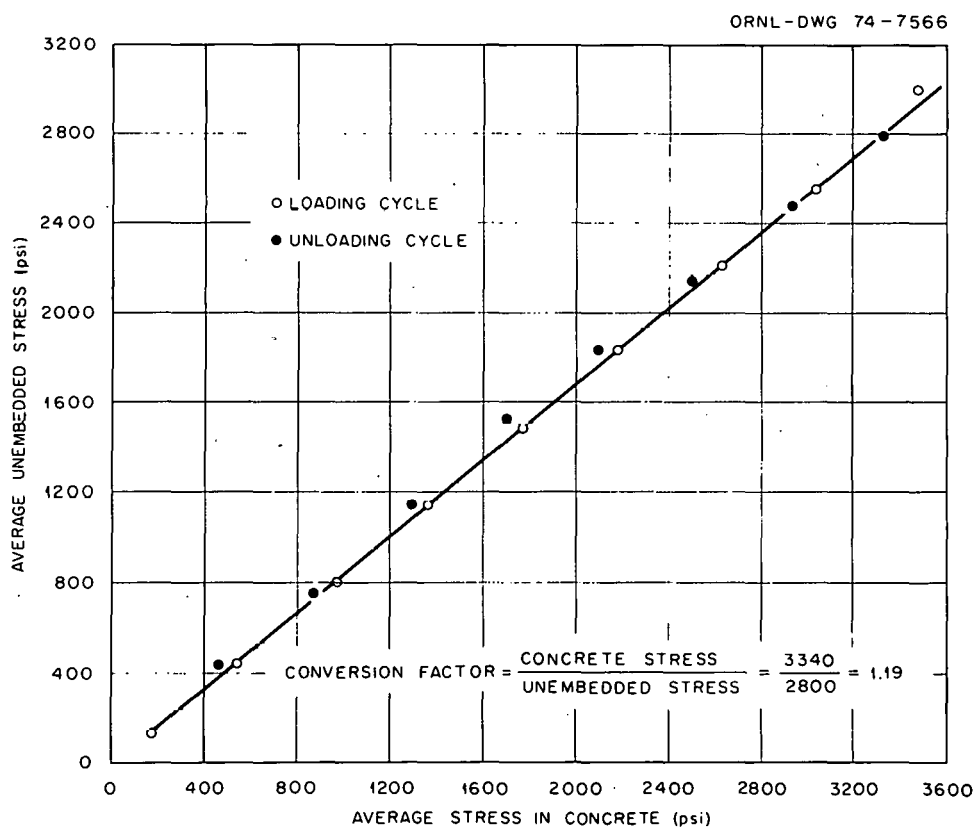Fig. 6.27. Comparison of laboratory calibration of concrete embedment stress cell for embedded and unembedded conditions (1 psi = 6895 Pa).

Although both types of stress-measurement devices used in this experiment offer some promise, considerable work will be required to develop a satisfactory embedment stress cell that is capable of monitoring time-dependent stresses in prestressed concrete structures.

7. POSTMORTEM STUDIES

7.1 Disassembly of the Model

Detensioning of the thermal cylinder model was completed on May 30, 1973 — 771 days from the time of the original tensioning of the prestressing system. First the circumferential tendons were completely detensioned; then the axial tendons were detensioned one step at a time (in sets of 13 in a quadrant), using the reverse of the original loading sequence.

One significant system failure was revealed during the detensioning operation. The axial tendons shown in Fig. 7.1 were equally divided into an inner and an outer row on the model test section. The hydraulic pull rams, which are shown positioned on top of the model in Fig. 4.3, were coupled to the tendons, and the loading was raised to 200 to 209 kN to lift off, or unseat, the restraining nut, which was then loosened. The first inner-row tendon was pulled out excessively at ∿90 kN, thereby indicating failure. All the outer-row tendons required a force of at least 200 kN to loosen the restraining nut, while all but two of the inner-row tendons required only a low ram pressure to unseat the nut.

Upon completion of the detensioning operation, one of the tendons that failed was removed. It appeared to have failed near the bottom anchor, and as indicated by the darkened appearance of some of the fracture surfaces, the wires had evidently failed prior to detensioning. The investigation of the mechanism of these tendon failures is discussed in Sect. 7.3.

After the circumferential prestressing assemblies were removed, the model was stripped and the inner concrete core (shown in Fig. 1.3) removed. A visual examination of the liner did not reveal any buckling, cracking, or other problems. Portions of the steel liners were removed at the six locations designated as cut sections in Fig. 7.2, and the exposed portions of the axial tendon assemblies were capped and sealed, as shown in Fig. 7.3, to prevent contamination during sectioning of the concrete. The model outer ring was transported to a commercial marble company for sectioning. The ring was first cut in half using a water-cooled (nonchlorinated well water) diamond wire saw; additional sectioning was done using a diamond

ORNL-DWG 73-7190R
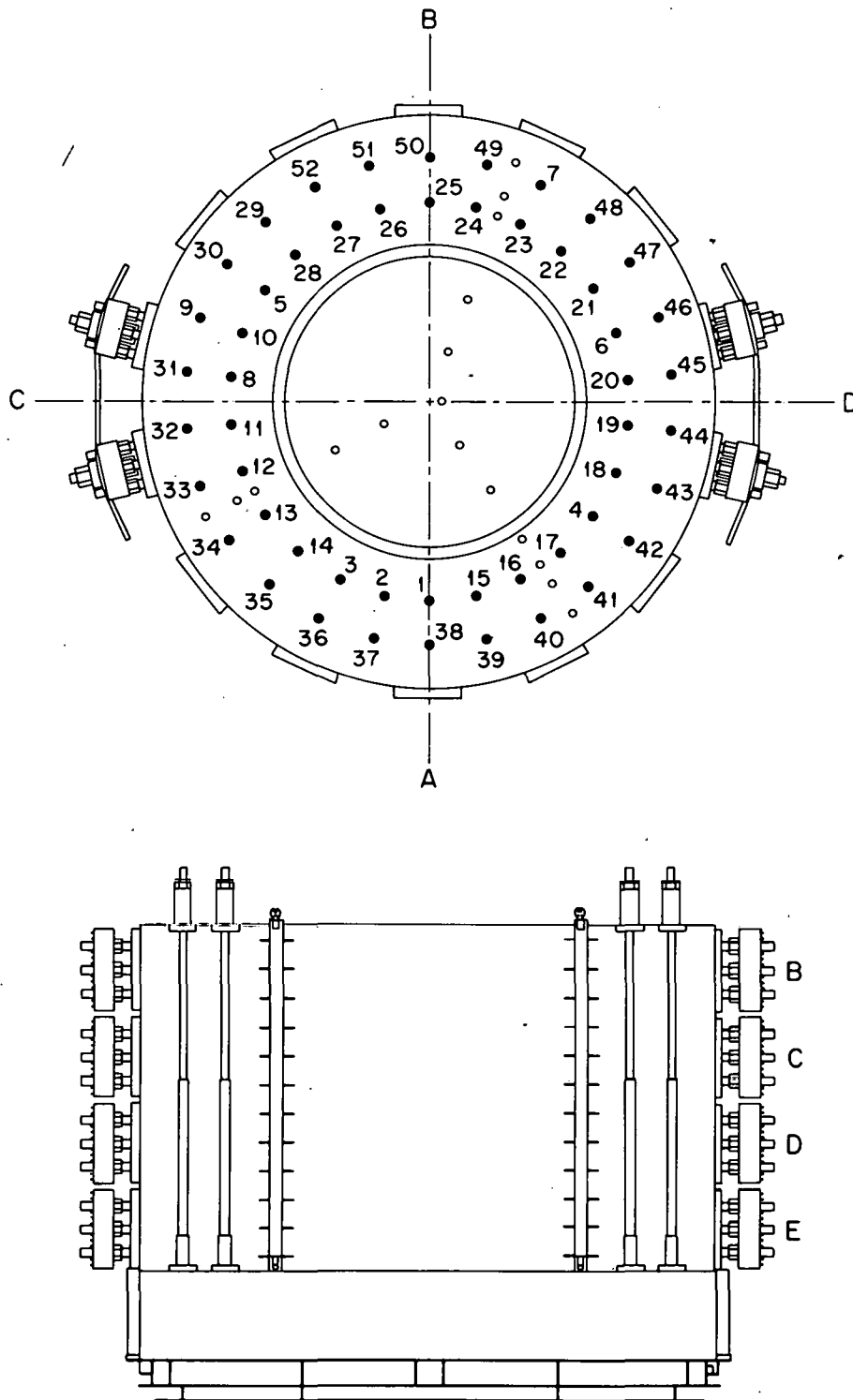
Fig. 7.1. Thermal cylinder prestressing system.

ORNL-DWG 74-7562

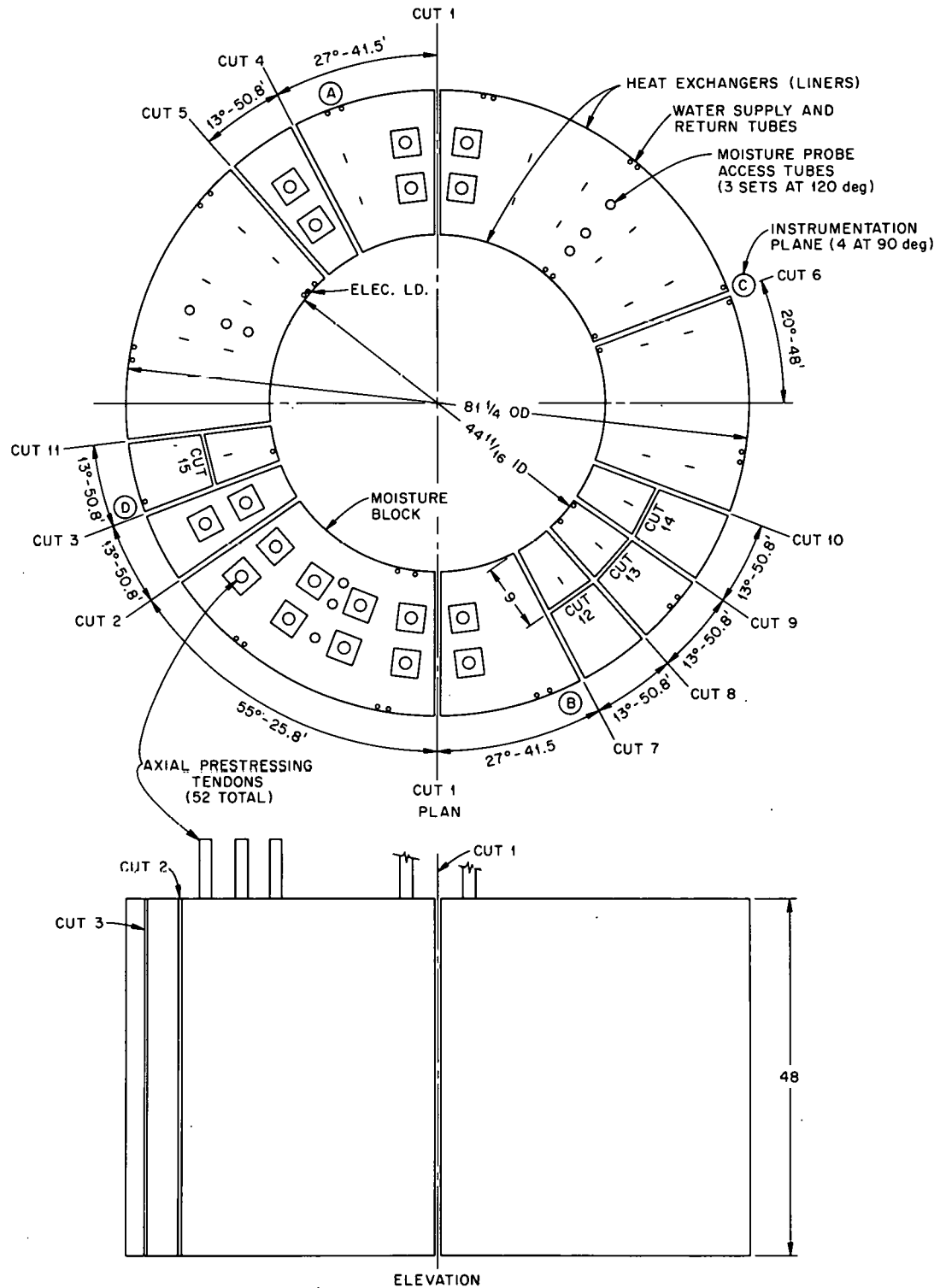Fig. 7.2. Thermal cylinder model sectioning plan [dimensions not otherwise identified in figure are in inches (1 in. = 25.4 mm)].

ORNL- DWG 74 - 7561

DUX - SEAL

PLAN SECTION

POLYETHYLENE CAP

$2\frac{1}{2}$ - in. O.D. ,16 GAGE
TUBING

SHIM BETWEEN
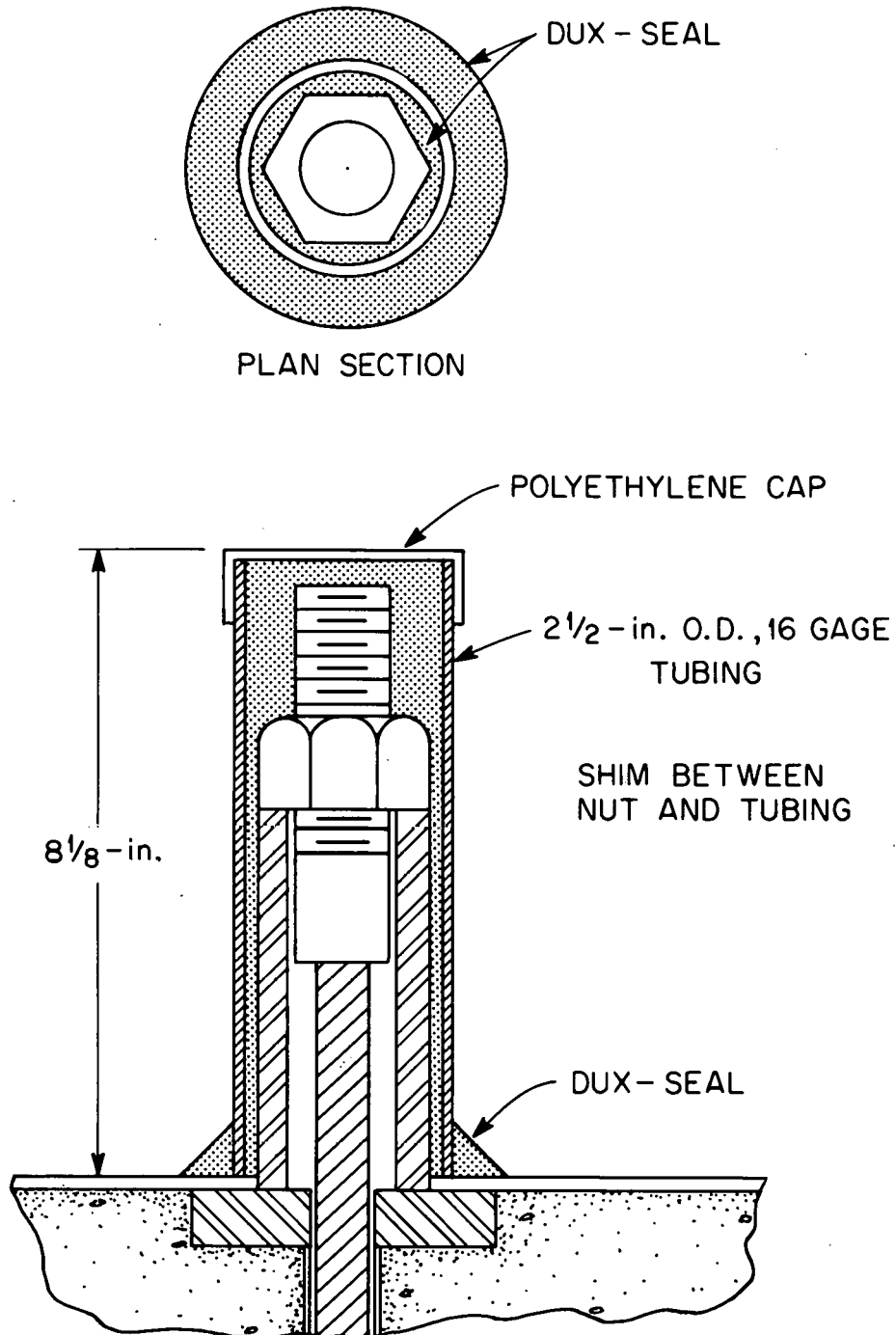NUT AND TUBING

$8\frac{1}{8}$ - in.

DUX - SEAL

Fig. 7.3. Axial prestressing tendon assembly moisture seal for con-
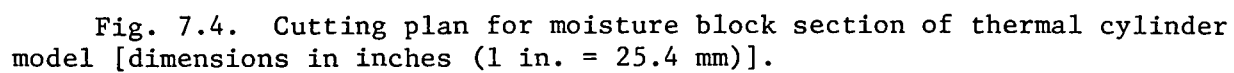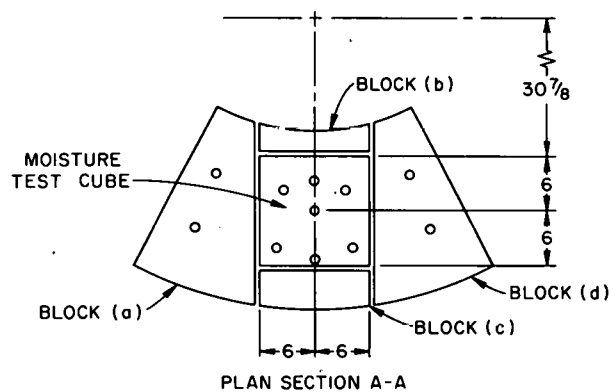crete sectioning (1 in. = 25.4 mm).

circular saw. The portion of the test section labeled "moisture block" in Fig. 7.2 was further sectioned, as shown in Fig. 7.4, to provide the 30.5- by 30.5- by 30.5-cm moisture test cube containing a stainless steel moisture probe access tube at the center. The use of this test cube in calibrating the moisture probe was described in Sect. 6.5.

Visual inspection of the exposed cross sections revealed no significant defects or structural cracks in the concrete. The slices made at the instrumentation section showed good bonds between the various gages and the concrete. The previously mentioned bonding problems with the wound-wire resistance embedment gages, which we assumed had occurred, were not discernible in the sliced sections.

The section produced by cut 15 (see Fig. 7.2) is shown in Fig. 7.5. The centermost gage label is to the right and below a precast three-gage rosette of single-filament resistance strain gages. A closeup of the excellent bond between the precast gage rosette and the remaining concrete is shown in Fig. 7.6. The upper gage shown in Fig. 7.5 is an axially oriented type A vibrating-wire gage, and the lower one is a radially oriented gage of the same type, with its activator coil housing and one end anchor exposed to view. The crack shown to the right of the upper gage occurred during the cutting operation, and the remaining inclusions seen in the concrete are primarily sectioned instrumentation leads.

7.2 Rebound Hammer Test

Although there were no significant defects seen in the cut surfaces, the concrete immediately surrounding the hot-spot heating elements was darkened, as shown in Fig. 7.7, which indicates that some change occurred in the concrete due to the 505.4 K hot-spot heating. A series of readings were made on the concrete faces using an impact hammer (or sclerometer) in order to quantify any change in the concrete properties. This test is based on the principle that the rebound of an elastic mass depends on the hardness of the surface against which the mass impinges. The compressive strength of materials can be determined from this behavior. The test apparatus consists of a spring-loaded mass having a fixed amount of energy imparted to it by extending a spring to a predetermined compression. When

Fig. 7.4. Cutting plan for moisture block section of thermal cylinder model [dimensions in inches (1 in. = 25.4 mm)].
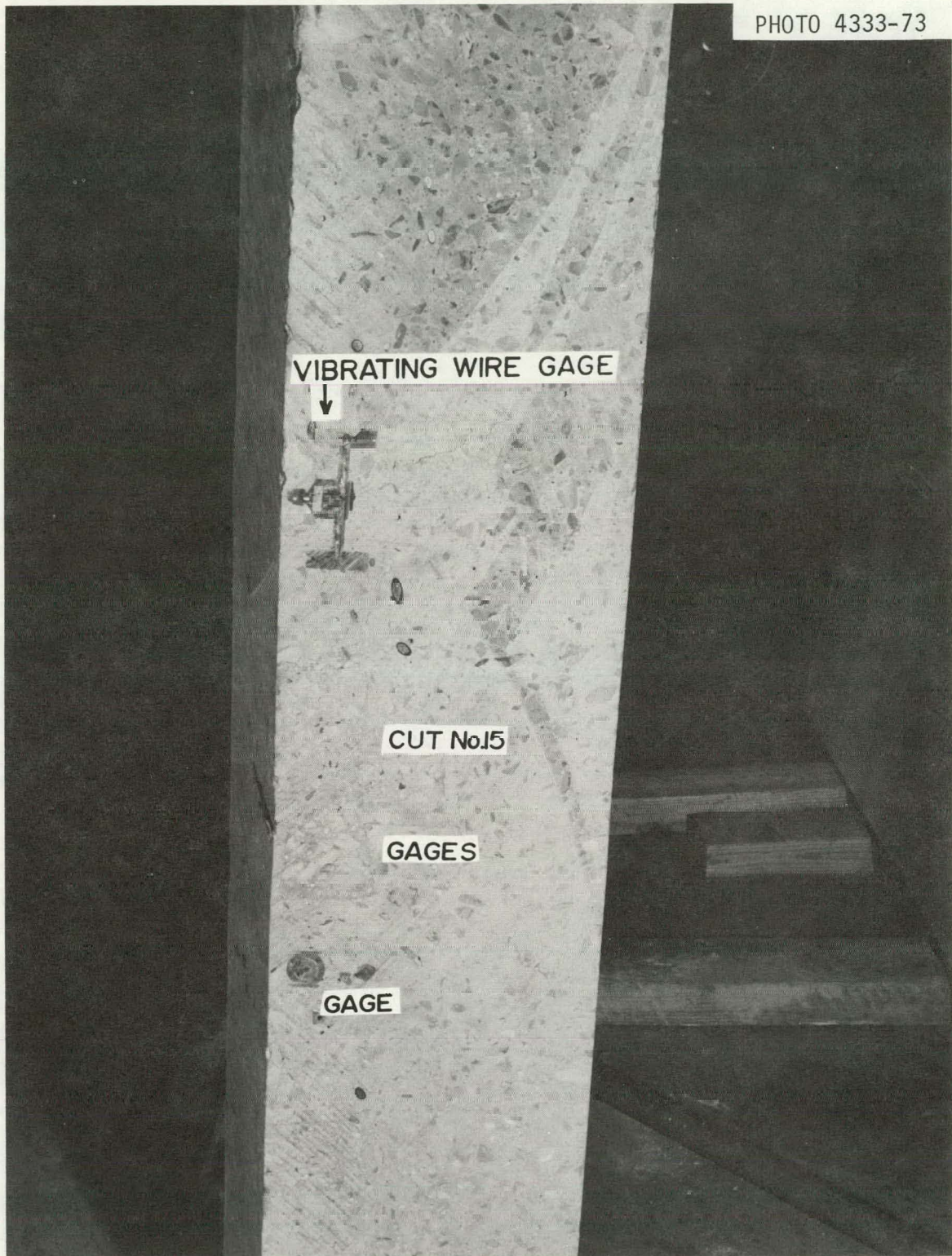
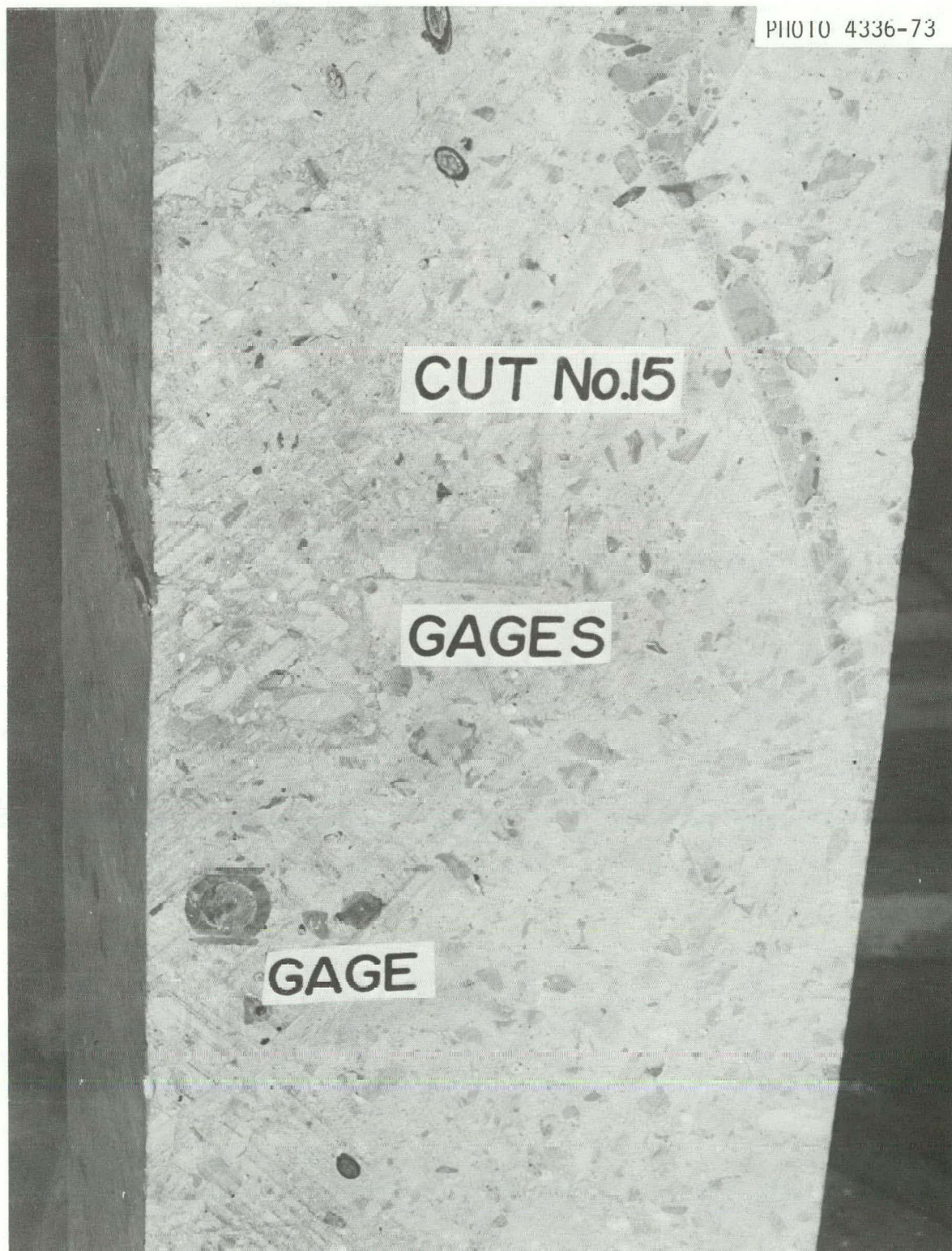Fig. 7.5. Thermal cylinder model section produced by cut 15.

Fig. 7.6. Closeup of cut 15 showing bond between precast single-filament resistance gage rosettes and model concrete.
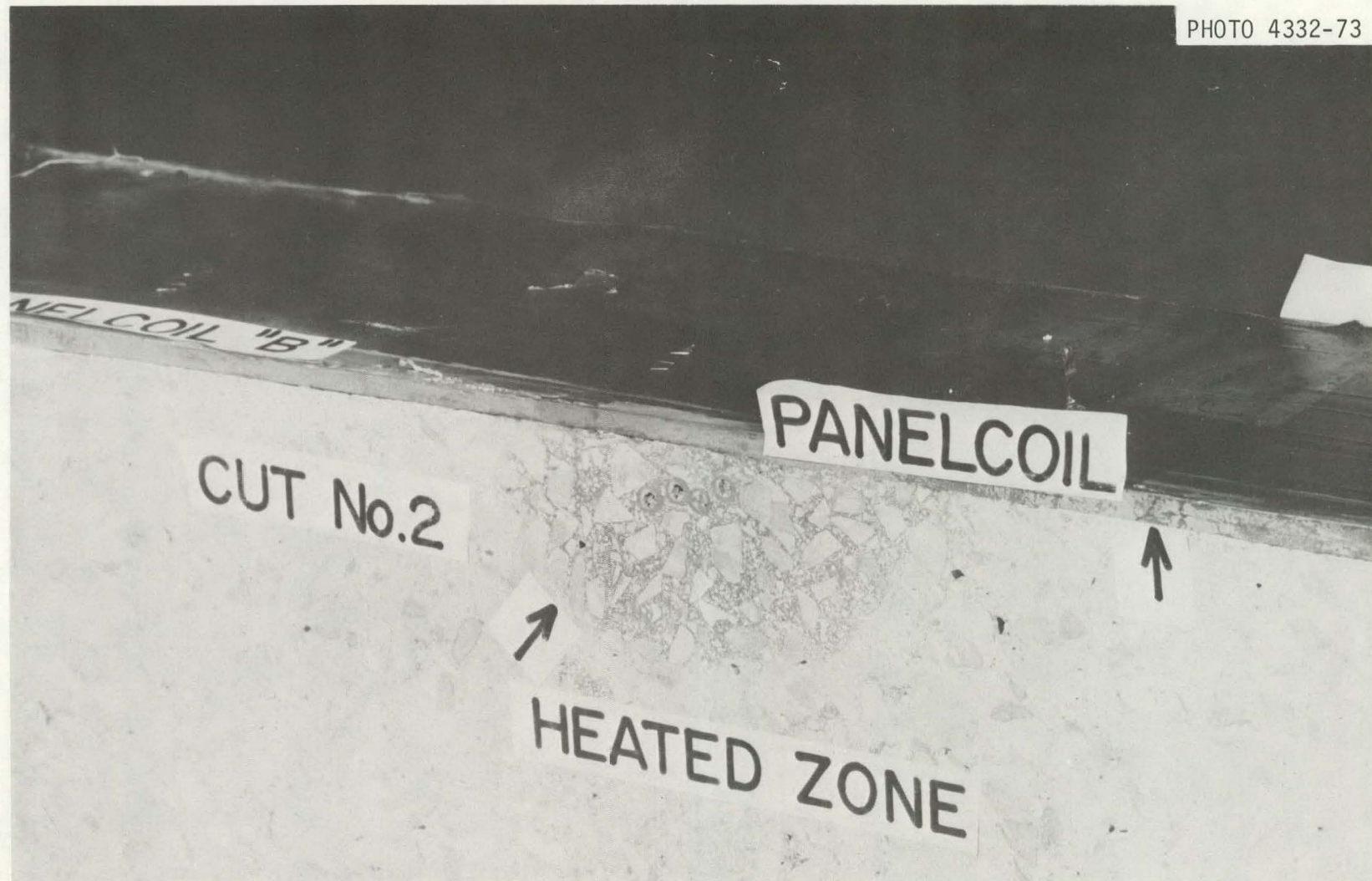
PHOTO 4332-73

Fig. 7.7. Cross section of cut 2 showing discoloration in the vicinity of the hot-spot heating coils.

released, the mass, or hammer, strikes the surface being tested and then rebounds; the distance traveled by the rebounding hammer, expressed as a percentage of the initial extension of the spring, is called the rebound number. This number is an arbitrary measure, since it depends on the energy stored in the given spring and on the size of the hammer.

The test is sensitive to local variations in the concrete; for example, the presence of a large piece of aggregate immediately beneath the plunger would result in an abnormally high rebound number, whereas the presence of a void in a similar position would result in a relatively low number. A correlation of rebound number with unconfined compressive strength is given by Neville[9] for a concrete made with crushed limestone aggregate; in Fig. 7.8, this curve is extended to include a compressive strength of 55.2 MPa.
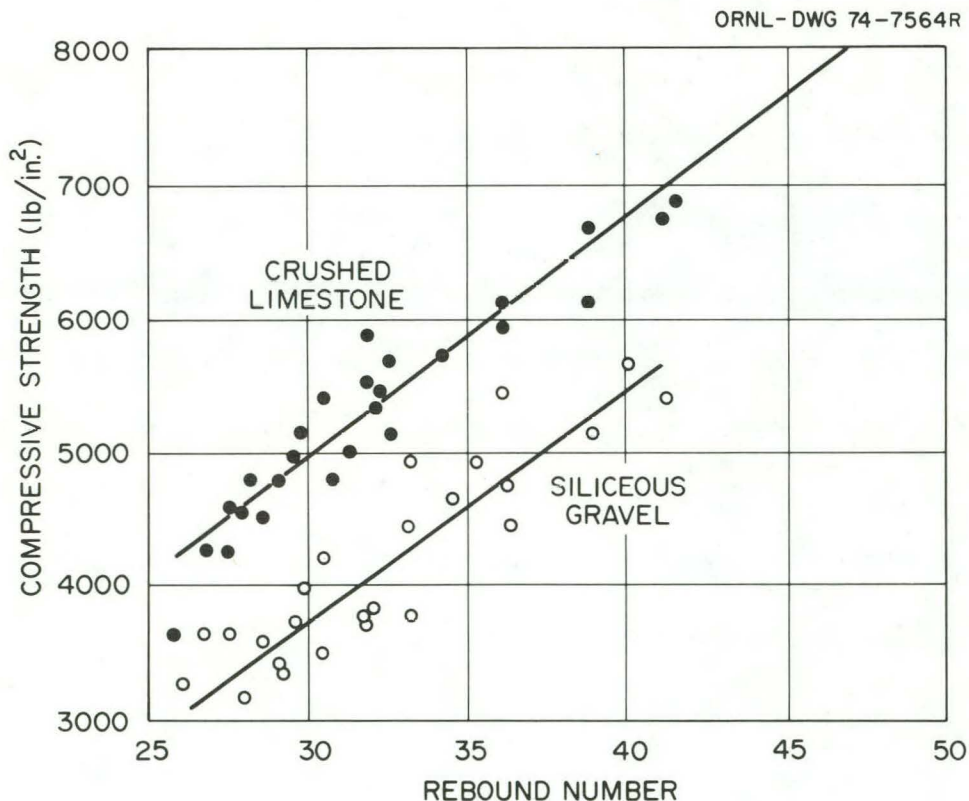
ORNL-DWG 74-7564R

Fig. 7.8. Relationship between compressive strength and rebound number for concrete cylinders made with different aggregates. Readings taken on the side of a cylinder with the hammer horizontal. (1 lb/in.^{2} = 6895 Pa.)

The results of a rebound test of the sectioned thermal cylinder model are shown in Table 7.1. Rebound readings were taken on the four faces of the cross section at the A and B quadrants. Readings were made along lines constructed perpendicular to the inside surface of the cylindrical test sections at two elevations, as shown in Fig. 7.9. One base set was taken in the upper part of the model approximately 0.3 m from the top, and one was taken through the vertical center of the hot-spot heated zone. The distances shown in the table were taken from the inside surface of the section. The "at heater" readings were taken directly adjacent to the Panelcoil heaters. As can be seen in the table, considerable compressive strength reductions were measured in the local heat-affected zone. This zone was easily distinguished by the distinct color change when compared with the rest of the cross section. On the other hand, the base readings taken at a considerable distance from the heat-affected zone show very little strength variation. The average strength determined from the base

Table 7.1. Summary of impact hammer (or sclerometer) readings
on thermal cylinder model cross sections

Distance [cm (in.)]	Base readings			Readings at hot-spot level					
	A	B	Average	A section		B section		Average	Compressive strength [MPa (psi)]
				1	2	1	2		
At heater				31	23		30	28.00	31.72 (4600)
2.54 (1)	43	41	42	38	40	38	34	37.50	43.44 (6300)
7.62 (3)	43	44	43.5	42	40	43	39	41.00	47.57 (6900)
12.70 (5)	45	46	45.5	41	40	40	43	41.00	47.57 (6900)
17.78 (7)	43	43	43.0	41	41	43	43	42.00	48.95 (7100)
22.86 (9)	44	43	43.5	48	41	42	44	43.75	51.71 (7500)
27.94 (11)	43	44	43.5	43	43	43	45	43.50	51.71 (7500)
33.02 (13)	43	44	43.4	42	45	43	45	43.75	51.71 (7500)
38.10 (15)	44	45	44.5	49[a]	43	44	44	43.70	51.71 (7500)
43.18 (17)	43	45	44.5	42	47	42	44	43.75	51.71 (7500)

[a]Excessively high readings taken on aggregates were not included in the average; readings for large aggregate inclusions were 50.
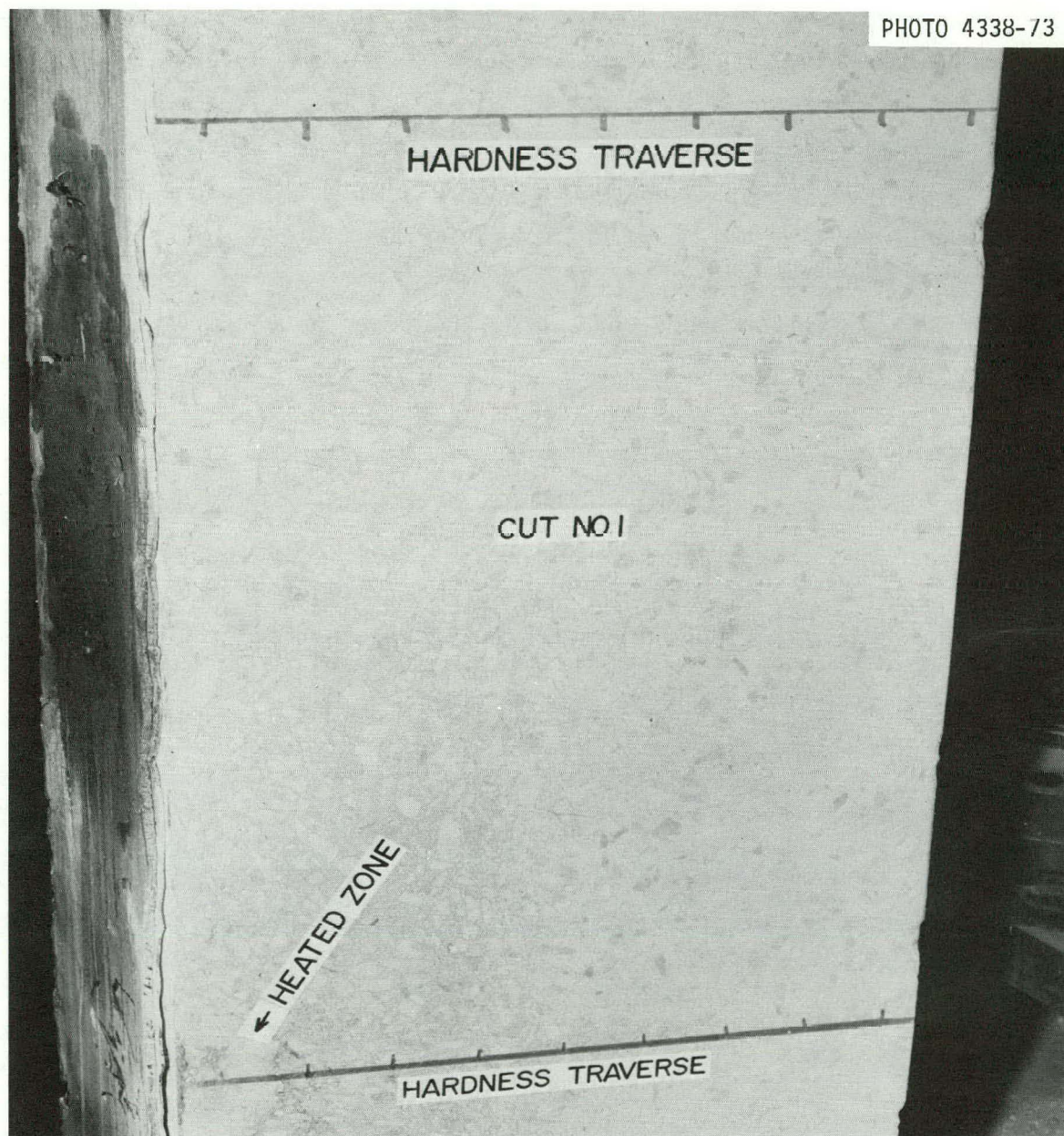
Fig. 7.9. Concrete rebound test traverse lines for concrete section of cut 1.

readings was 51.7 MPa. There is little doubt that a significant loss of strength occurred in the heat-affected zone. The thermal cylinder had a 28-day unconfined compressive strength of approximately 48.3 MPa, which may indicate that the rebound reading strength correlation may be slightly low. However, these readings were taken on the matrix rather than on the

aggregates whenever possible. The rebound readings made on large aggregates were significantly higher.

7.3 Prestressing Tendon Corrosion

An investigation was conducted to determine the causes of the tendon failures described in Sect. 7.1. The condition of the 26 inner-row and outer row tendons is summarized in Table 7.2. The location in the model of each tendon listed is shown in Fig. 7.1.

7.3.1 Description of axial tendons

Each tendon was a 1.52-cm-diam LOK-STRESS monostrand consisting of seven wires and having S.E.E.E. anchors attached to both ends. These strands were manufactured in accordance with ASTM A416 and were specified in this case to minimize possible relaxation losses. They have a modulus of elasticity of 193 GPa and a breaking strength of 1,724 MPa.

The tendons were coated with a widely used, commercial corrosion-protection material when received from the manufacturer. A total of 12 tendons, 6 in each row, were instrumented with load cells at the top anchor and foil-type electrical resistance strain gages on one wire of each strand. It was necessary to remove the original protective coating from an approximately 30.5-cm section of the instrumented wire in order to install the gage. These were the only tendons from which any of the original corrosion protection was removed. After the strain gage was installed, the tendon was waterproofed with a commercial wax, using methods recommended by the Portland Cement Association.[10] The specific wax employed is generally recognized as being effective for corrosion protection. The tendons were housed in two-piece telescoping ducts in the manner shown in Fig. 7.10. First the joint at the bottom anchor fitting was sealed with heat-shrinkable Flexite tubing, and the lower duct section was filled with melted wax. Then the upper joint was sealed with Flexite tubing, and the upper duct section was filled with melted wax. The known volume of wax required to fill each tendon assembly was used to indicate whether the duct was completely filled. When properly fitted, the Flexite tubing bulged slightly. As a final step, the lower end of the bottom anchor fitting was sealed with melted max.

Table 7.2. Axial tendon examination of PCRV thermal cylinder model

Tendon No.	Row[a]	Load cell designation	Failure location	Remarks
1	I	ATR-11	Broke near bottom anchor	Failed at time of detensioning[b]
2	I	None	Broke near bottom anchor	Failed at time of detensioning
3	I	None	Broke near bottom anchor	Failed at time of detensioning
4	I	None	Broke near bottom anchor	Failed at time of detensioning
5	I	None	Broke near bottom anchor	Failed at time of detensioning
6	I	None	Broke near bottom anchor	Failed at time of detensioning
7	O	None	Failed at top	Failed at 0.256 MN (57,500 lb)
8	I	CTR-3	Failed near center	Failed at 0.037 MN (8400 lb)
9	O	None	Wire pulled through top anchor [1.27-cm (0.5-in.) wire in anchor)	Stopped at 0.26 MN (60,000 lb) wire slipping in anchor
10	I	None		Failed at time of detensioning
11	I	CTR-1		Failed during test (see load cell data)
12	I	None	Broke near top anchor	Failed at 0.028 MN (6200 lb)
13	I	None		Failed at time of detensioning
14	I	None		Failed at time of detensioning
15	I	None		Failed at time of detensioning
16	I	None		Failed at 0.191 MN (43,000 lb)
17	I	None		Failed at time of detensioning
18	I	None		Failed at 0.102 MN (23,000 lb)
19	I	DTR-9	Failed near top anchor	Failed at 0.267 MN (60,000 lb)
20	I	DTR-7		No indication of failure
21	I	None	Failed near bottom anchor	Failed at 0.254 MN (57,000 lb) (one wire shows cracks)
22	I	None		Failed at time of detensioning
23	I	None		Failed at 0.138 MN (31,000 lb)
24	I	None		Failed at 0.129 MN (29,000 lb)
25	I	BTR-5		Failed during test (see load cell data)
26	I	None		Excessive yielding at 0.145 MN (32,500 lb)
27	I	None		Failed at time of detensioning
28	I	None		Excessive yielding at 0.147 MN (33,000 lb)

[a]I = inner row; O = outer row.

[b]Refers to tendons having failed prior to detensioning.

84

85

ORNL-DWG 73-7191

TOP ANCHOR FITTING

TOP SEAL SHEET

TOP ANCHOR PLATE

UPPER DUCT

SHRINK TUBING SLEEVE

TENDON

WAX FILLED ANNULUS

LOWER DUCT

BOTTOM
ANCHOR PLATE

SHRINK TUBING SLEEVE

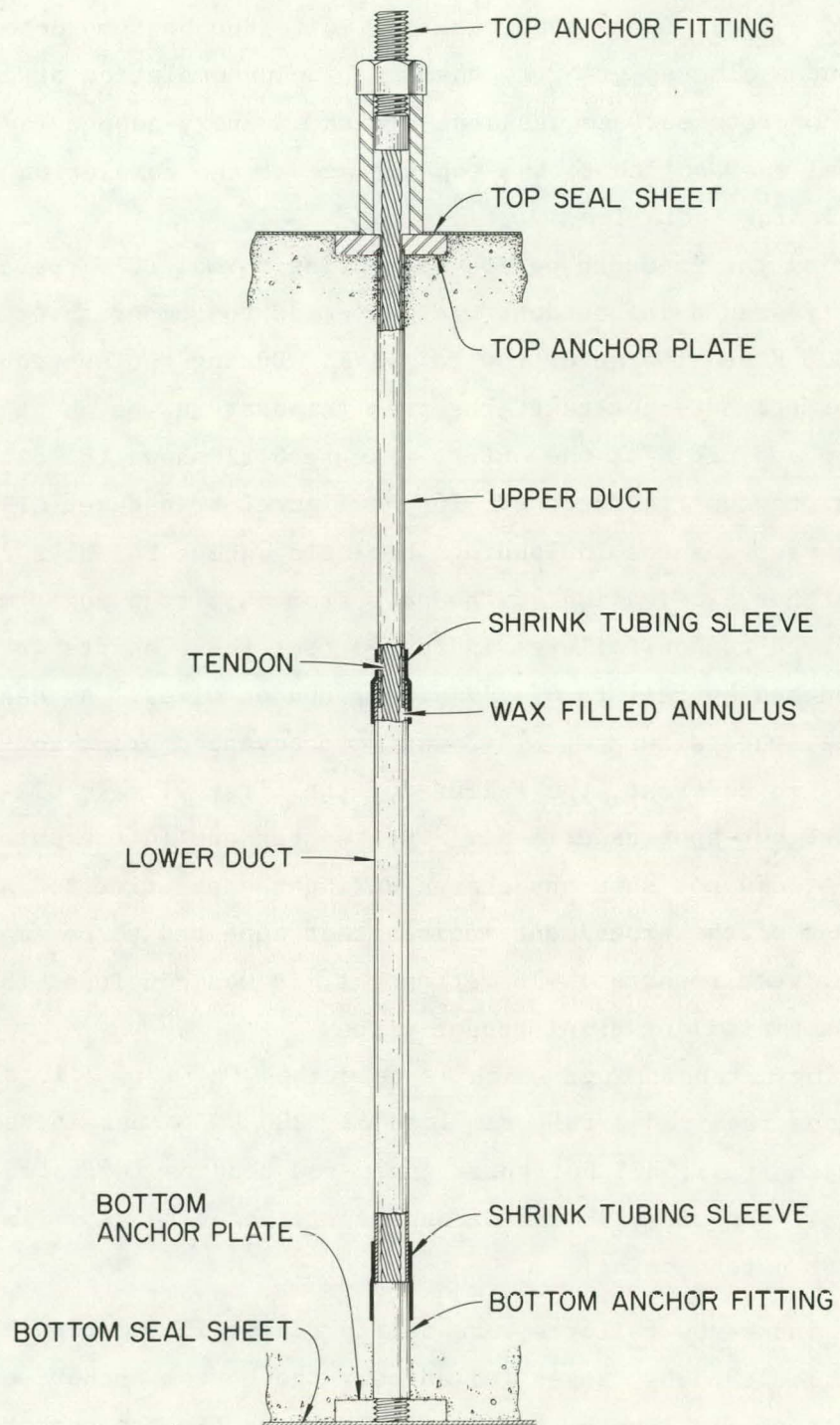BOTTOM ANCHOR FITTING

BOTTOM SEAL SHEET

Fig. 7.10. Axial tendon assembly detail.

The sealed tendon assemblies were positioned in the structure as shown in Fig. 1.3, and the bottom anchor plates were tack welded onto the bottom sheet-metal seal. The assemblies were held in place at the top by a fixture, and a final epoxy seal was applied to the bottom anchor plates and lower tendon sleeves prior to casting. Upon completion of casting, the exposed concrete surface was sealed with an epoxy-copper layer. A final epoxy seal was applied to the top surface at the completion of the tendon posttensioning operation.

During the 15-month period simulating normal PCRV operation, the inner row of stressed axial tendons was subjected to temperatures of approximately 325 K and the outer row to 311 K. During the subsequent 3-month period of the hot-spot test, the peak temperature was about 380 K at the inner row and 328 K at the outer. Figure 6.21 shows the data for four of the axial tendon transducers. In the figure, transducer CTR-3 shows significant step changes in loadings beginning about 245 days from prestressing. Further examination of the data from this transducer made in light of the observed tendon failures indicated that these shifts in load readings were produced by failure of individual tendon wires. As can be seen in Fig. 6.21, the failure of CTR-3 was well advanced prior to the hot-spot heating. In contrast, the failure of the first wire in CTR-1 occurred during the hot-spot experiment. The two tendons in the outer row, CTR-2 and CTR-4, did not show any change during the experiment. Also, during the course of the experiment, noises that appeared to be emanating from the model were reported. In retrospect, it was concluded that these sounds were made by failing axial tendon wires.

During detensioning, which is described in Sect. 7.1, all the outer-row tendons required a full ram load of ∿200 kN to unseat the restraining nut. In contrast, all but three inner-row tendons indicated failure of some or all the wires in the strand by virtue of the low ram pressure required for detensioning.

The inner-row failures were fairly random in location. Of the ten fully failed tendons, seven failed near the bottom anchor, one failed near the middle of its length, and two failed near the top anchor. In contrast, during a selective reloading of outer-row tendon 6, the top anchor fitting,

shown schematically in Fig. 7.10, was pulled almost through the entire length of strand to which it was swaged without inducing wire failure.

7.3.2 Metallurgical and chemical analyses

An example of a typical wire fracture is shown in Fig. 7.11. All the failures contained a flat semielliptical initiation site and, when the net area of the wire was unable to sustain the applied load, a ductile cup-cone fracture. The initiation site in the wire shown in Fig. 7.11 contained sulfur, but this was not necessarily true of all the failures.

The results of a chemical analysis of the as-received protective agents and the wax remaining in the tendon ducts are provided in Table 7.3. It was evident that the wax in the ducts contained large quantities of nitrogen. Although the exact chemical form of the nitrogen was not determined, the wax displayed a strong odor of ammonia when it was initially removed from the ducts. This was true for both inner- and outer-row tendons. The presence of nitrogen has been attributed to the use of an excessive amount of hardener in the epoxy sealer, since hardeners used with epoxy resins contain organic amines which can hydrolyze in the presence of water to produce ammonia. Visual imspection of the polyvinyl fluoride shrink tubing on several of the removed tendons indicated that the tubing was ineffective in preventing ingress of water from the concrete.

An analysis of a quantity of liquid extracted from the tendon ducts showed it to be an aqueous solution containing nitrogen, chlorine, sulfur, and perhaps other substances. The nitrogen appeared to be mostly in the form of ammonia (or perhaps a volatile amine), but in a few cases low levels of nitrate ($\sim$50 ppm) were also present. A complete analysis was not possible owing to the small quantity of liquid present in the ducts.

7.3.3 Corrosion tests

Various ammonium salts, such as nitrate and carbonate, are known to be capable of producing stress-corrosion cracking in steels. To determine whether the steel in question was susceptible to cracking in such environments, several U-bend specimens of the steel were exposed to various solutions that contained certain ammonium salts and the epoxy mixtures.
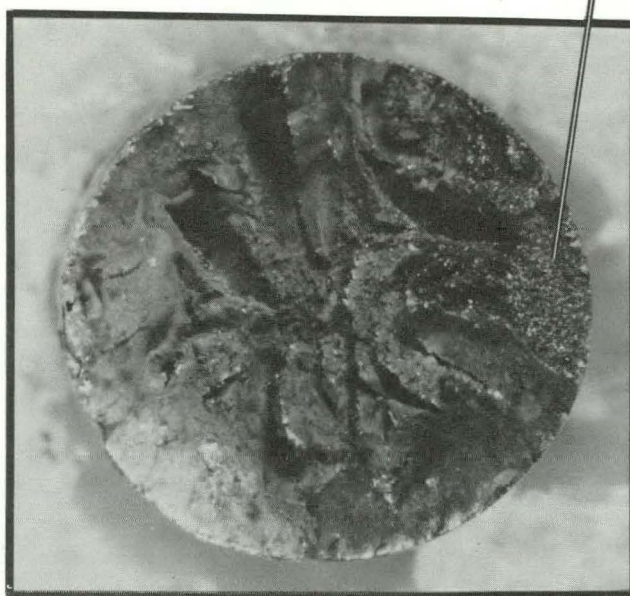
Y-120281
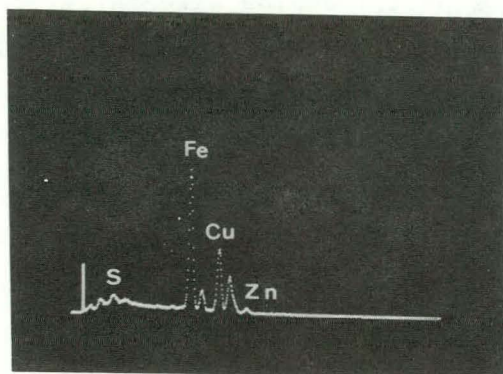
X-RAY ANALYSIS OF FRACTURE SURFACE
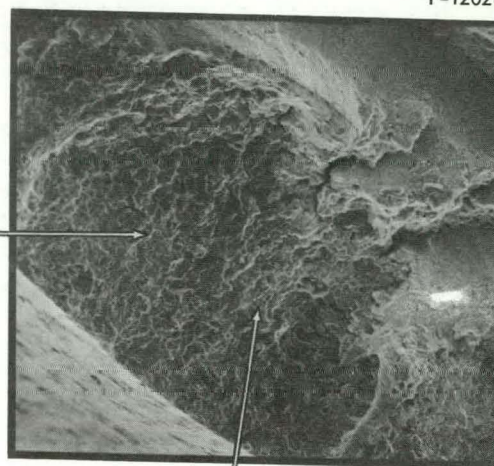
SEM PHOTOGRAPH OF FRACTURE SURFACE

TENDON 1, STRAND 7

Fig. 7.11. Fractographic examination of failure surface in a wire from tendon 1. The flat area in the photomacrograph was viewed and analyzed in the scanning electron microscope. There is a definite indication of sulfur in the flat area of the fracture surface.

The test specimens were made from the center wires of uncracked cir-cumferential tendons taken from the thermal cylinder experiment. The wires were ground to a diameter of 1.5 mm (by centerless grinding), and 76-mm lengths were bent into the small-radius U-shaped specimens shown in Fig. 7.12. The small specimens were placed in 25-ml Pyrex bottles containing 15 ml of test solution, and the bottles were capped and then heated in a small oven at the desired temperature.

Table 7.3 Chemical analysis of the thermal
cylinder axial tendon protective agents

Identification of source of wax	Level of contaminant (ppm)			
	Cl	S	N	H_2O
As-received corrosion-protection material	3.1 2.1 2.4	1900	785	76
As-received commercial wax	3.6 7.6 2.7	3200	200	32
Wax removed from:				
Tendon 19[a]			840	1,900
Tendon 28[a]			6400	25,585
Tendon 44[b]			1000	24,800

[a]Inner-row tendon that contained failed wire(s).

[b]Outer-row tendon that did not contain a failed wire.

No cracks developed in specimens exposed either to an epoxy mixture
(with or without CO_2) or to the water equilibrated with them during expo-
sures that lasted 94 days at 343 K. Similar tests in the same environments
but with 50 ppm nitrate added produced no cracking during a 100-day test at
339 K. Cracking was also absent in specimens exposed to concentrations of
ammonium carbonate solutions under the same conditions, either with or with-
out 50 ppm nitrate added.

Cracking occurred only in 0.2- and 2.0-M ammonium nitrate solutions.
In the 0.2-M solution at 343 K, duplicate specimens cracked in 3 days.
Under the same conditions, the single specimen exposed to the 2.0-M solu-
tion cracked in the interval between 7 and 10 days. A specimen that failed
is shown in Fig. 7.13. Failures in the other two U-bend specimens appeared
to be almost identical to the one shown in the figure. The single specimen
exposed to a saturated solution of ammonium nitrate at 343 K did not crack
during the 94-day test.

The results of the U-bend tests show that the tendon material is
susceptible to stress-corrosion cracking in 0.2- and 2.0-M ammonium
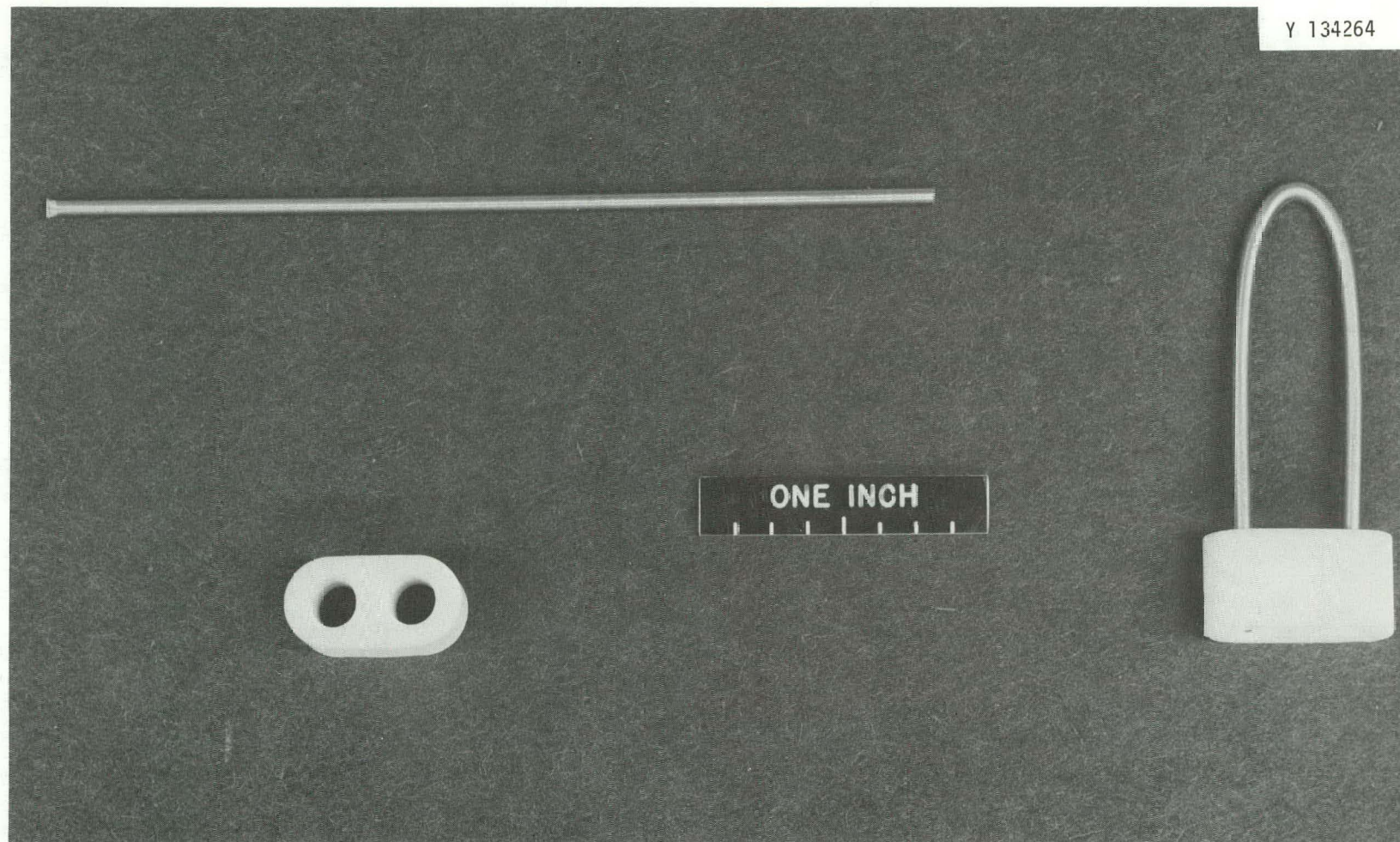nitrate, but not susceptible in very dilute solutions (50 ppm) nor in very

Fig. 7.12. The U-bend specimen used in the stress-corrosion studies.
The 1.5-mm-diam steel test section was ground from a sound area of a wire
removed from a tendon in which individual wires had failed. The wire is
bent into the U configuration, and its ends are placed in the refractory
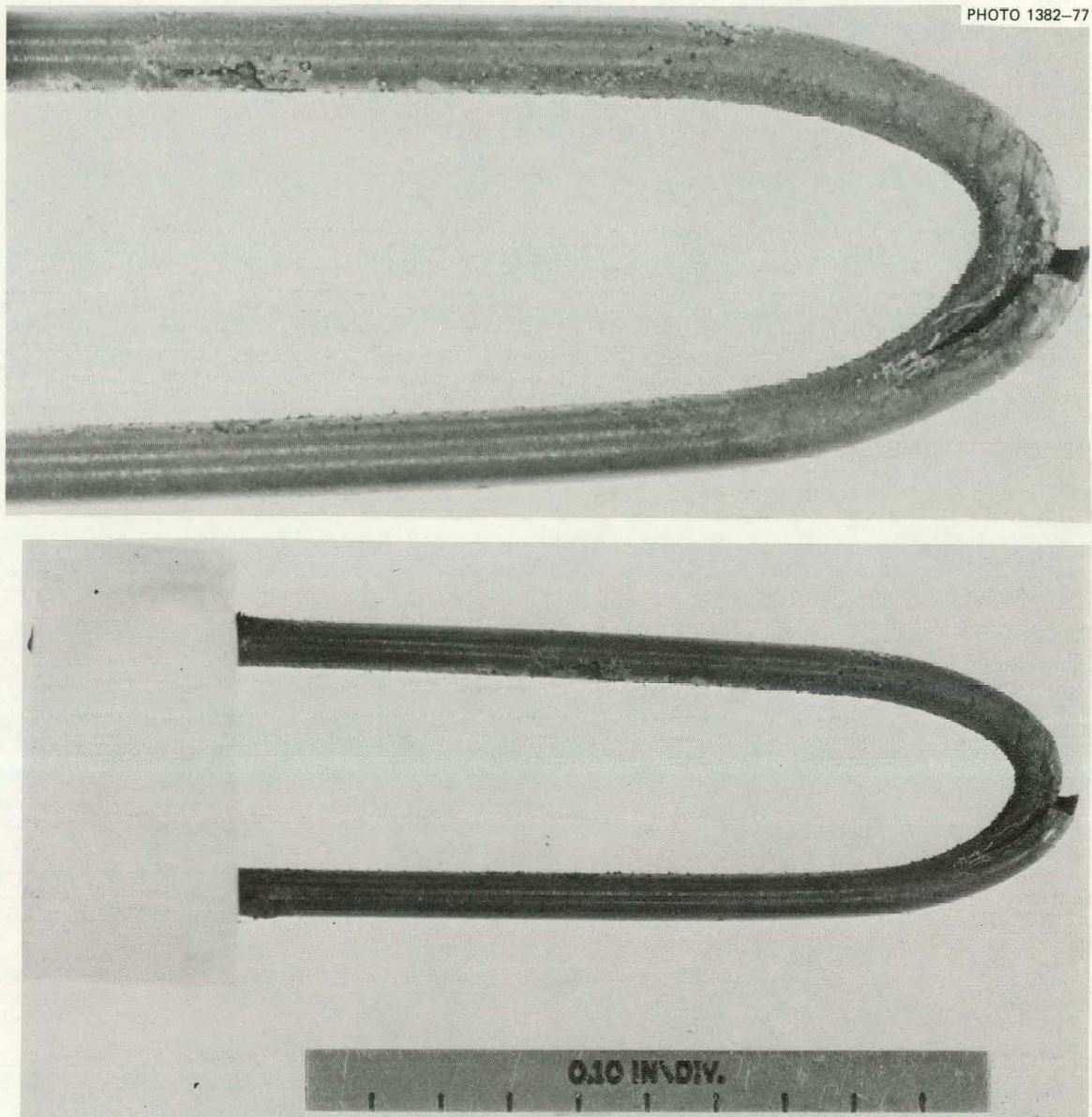retainer. (1 in. = 25.4 mm.)

Fig. 7.13. U-bend stress-corrosion specimen that failed in a 0.2-*M* ammonium nitrate solution in 72 hr at 343 K (1 in. = 25.4 mm). (Original reduced 42.5%)

concentrated solutions (saturated at test temperatures). However, in certain regions along the tendons, higher concentrations of the dilute nitrate solution could have developed, in which case cracking could have occurred. These results do not allow one to conclude unequivocally that ammonium nitrate was responsible for the observed cracking, but neither do they exclude the possibility that cracking resulted from the presence of nitrate in the aqueous environment.

7.3.4 Retension tests

Tests were also conducted to determine whether the slight difference in temperature experienced by the outer (311 K) and the inner (325 K) row of tendons was responsible for the preponderance of failures in the inner row. Two pie-shaped segments were cut from the thermal cylinder model for the tests, one including tendons 15 and 39 and the other tendons 20 and 45 (see Fig. 7.1).

Each concrete segment was outfitted on the outer cylindrical surface with silicone rubber electric strip heaters and on the radial cuts immediately adjacent to the inside circumferential surface with Panelcoil heat exchangers, as shown in Fig. 7.14. Each tendon was equipped with a cali-
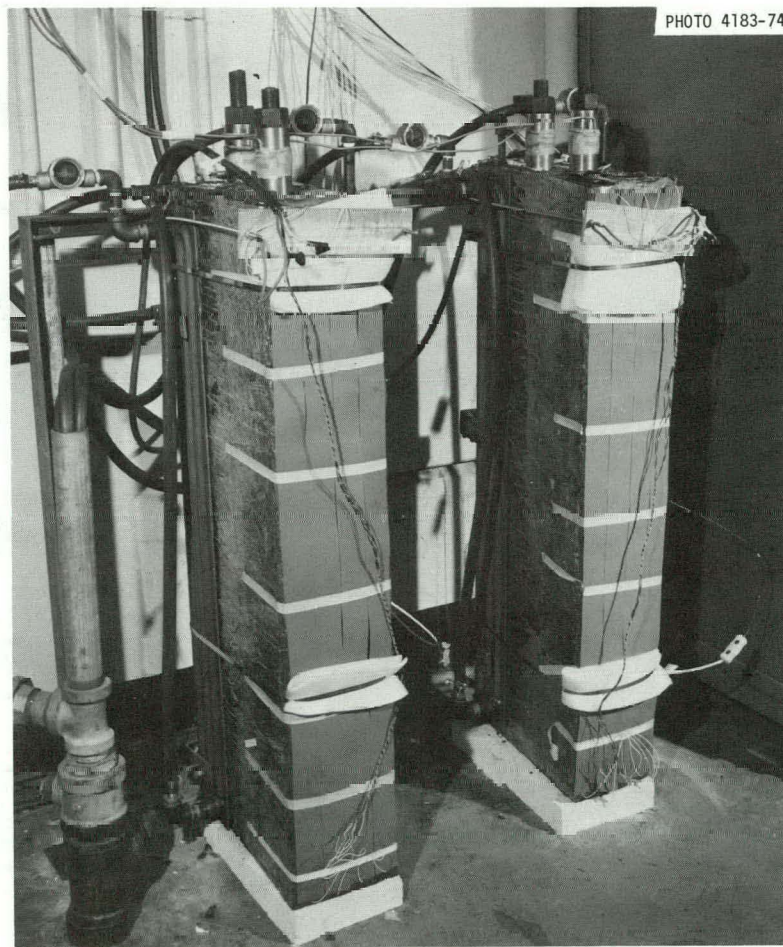

Fig. 7.14. Panelcoils and electric strip heaters installed on segments of thermal cylinder before insulation.

brated load cell, the output of which was continuously recorded by a multipoint recorded. Thermocouples were embedded in the inner and outer cylindrical faces of the segments, and temperatures were also continuously recorded by the multipoint recorder. Heater input was controlled by a manually adjustable Variac voltage control and by a temperature controller.

Tendons 20 and 45 in one segment and tendon 39 in the second segment were subjected to a second tensioning. Tendon 45 was retensioned to the design load of 162.2 kN; tendons 39 and 20 were subjected to reduced loadings of 84.1 kN and 86.7 kN, respectively; and tendon 15 remained unstressed, since it had failed during detensioning of the model. The electric heaters and Panelcoils were then used to impose thermal conditions of 339 K and 297 K on the outside and inside surfaces (a reversal of the thermal crossfall used with the original model). The tendon loads and temperatures of the segments were monitored continuously thereafter for a two-year period during which no significant change in load was detected. Thus, the reversed thermal gradient imposed on the segments had no observable effect. The cause of the preponderance of failures of inner-row tendons, therefore, remains unidentified.

7.3.5 Assessment of wire quality

Studies of randomly selected wires have revealed that the wires in the axial tendons used to prestress the thermal cylinder model were of questionable quality. Locating these defective areas in the axial tendon wires was fortuitous; radiographic examinations of randomly selected wires removed from the circumferential tendons did not reveal any defects, but metallographic examination revealed some hairline cracks. Figures 7.15 and 7.16 are typical of the types of defects observed. These cracks are not detectable by the usual examination standards.

During centerless grinding of the wires used for U-bend stress-corrosion test specimens, one wire separated into two pieces. A metallographic examination of the wire revealed several fissure-like cracks which could serve as locations both for the concentration of contaminants present and for the development of stress concentrations (see Fig. 7.17). Thus, these cracks could have contributed to the failures observed during the thermal cylinder test.
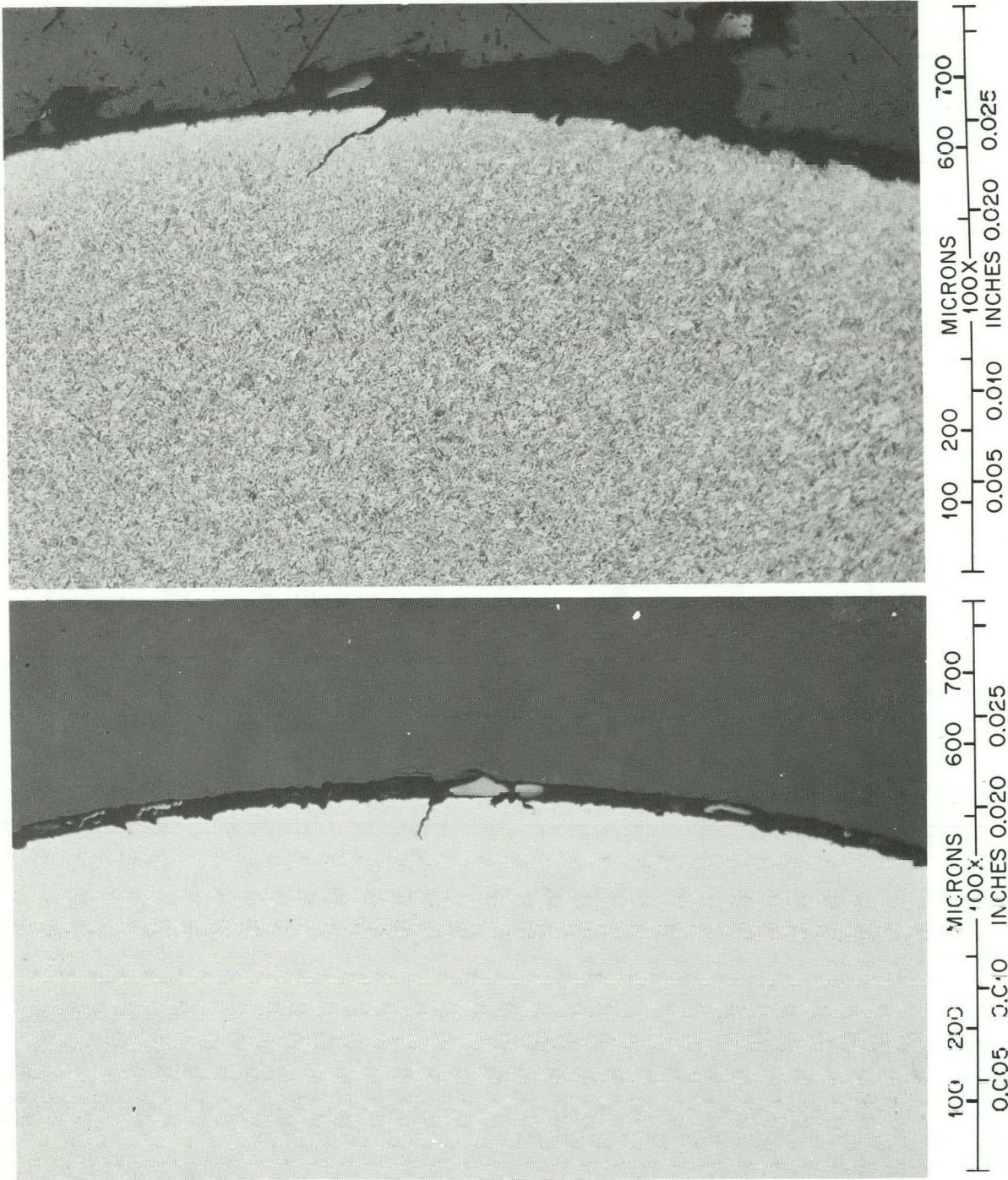
Fig. 7.15. Surface defects in a wire used in the manufacture of tendons (100×). These surface defects could serve as sites for the concentration of contaminants that cause stress-corrosion cracking. (Original reduced 42.5%)

Fig. 7.16. Photomicrograph showing sulfide stringers in the interior of a randomly selected section of circumferential tendons employed in the thermal cylinder test (500×). (Original reduced 43%)
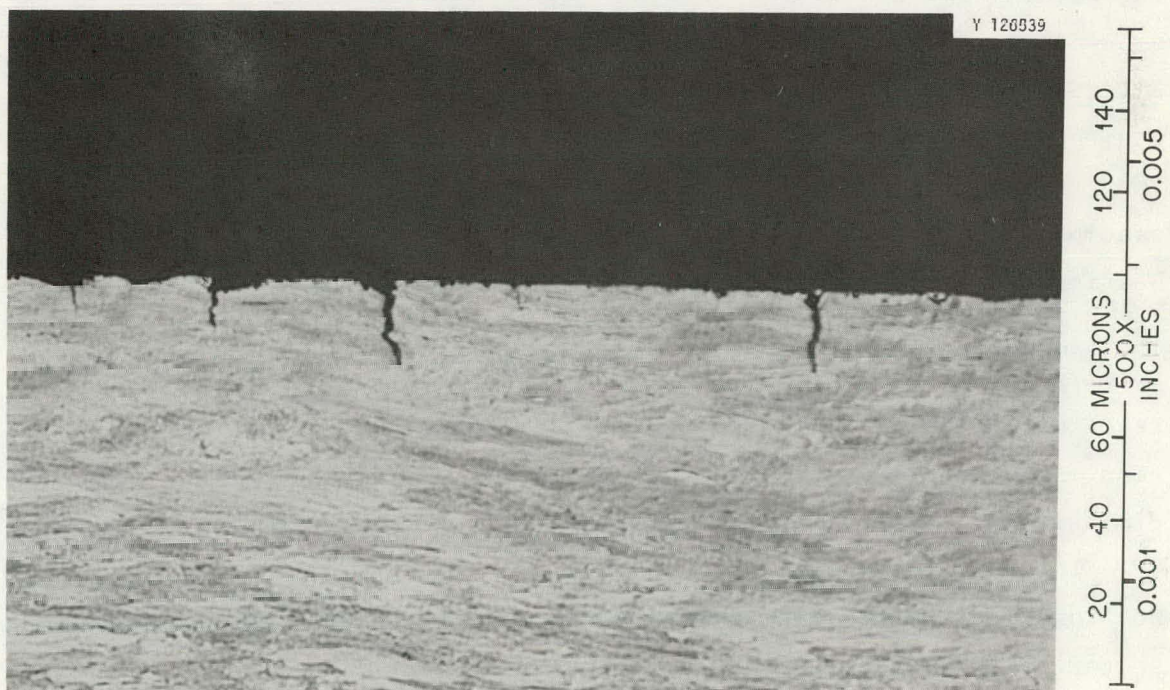

Fig. 7.17. Photomicrograph of a wire that separated during a center-less grinding operation. The cracks, which are perpendicular to the longitudinal axis of the wire, could contribute to premature failure. (Original reduced 43%)

7.4 Correlation of Analytical Results with Model Test Data

The differences between the analytical results obtained from the SAFE/ CRACK finite-element code and the results obtained from embedded strain transducers in the ORNL thermal cylinder model seemed to be excessive when compared with similar results found in the published literature.[11-13] To better judge the accuracy of the experimental results and to identify any trends, it is desirable to compare the results from groups of gages whose readings should be essentially the same. Due to the model design (Fig. 1.3), the effect of end restraints on the strain distribution near the midplane should be negligible. Hence, it is reasonable to ignore differences in the axial position. With the additional assumption that the loading is axisymmetric, the only relevant positional parameter for grouping is the radial position of the gages.

A significant number of gages were located in the neighborhood of three radial positions: (1) 7.6 cm from the inside wall, (2) at midthickness, and (3) 7.6 cm from the outside wall. These positions will be referred to as the inside, middle, and outside positions, respectively. The strain-time histories shown in Figs. 7.18 through 7.26 indicate that a number of gages at each location exhibit similar trends throughout the life of the test but have significant differences in strain magnitudes. It was thought that some of these differences could be attributed to the fact that the circumferential prestressing was not uniformly distributed, as assumed in the axisymmetric analysis, but was locally applied through steel bearing pads. These pads were approximately 20.3 cm wide and had a center-to-center circumferential spacing of 45.7 cm. The effect of this nonuniformity in the loading should be particularly significant for the outer gages but could also be expected to have some effect throughout the thickness, since the thickness of the model wall was of approximately the same dimension as the pad spacing.

In order to investigate the effect of nonuniform loading of the model due to circumferential prestressing, a thin slice from midheight in a sector of the vessel was analyzed, using a radial loading obtained from an analysis of the force transmitted by the prestressing through the bearing pads. Figure 7.27 shows the finite-element mesh, the loading conditions,
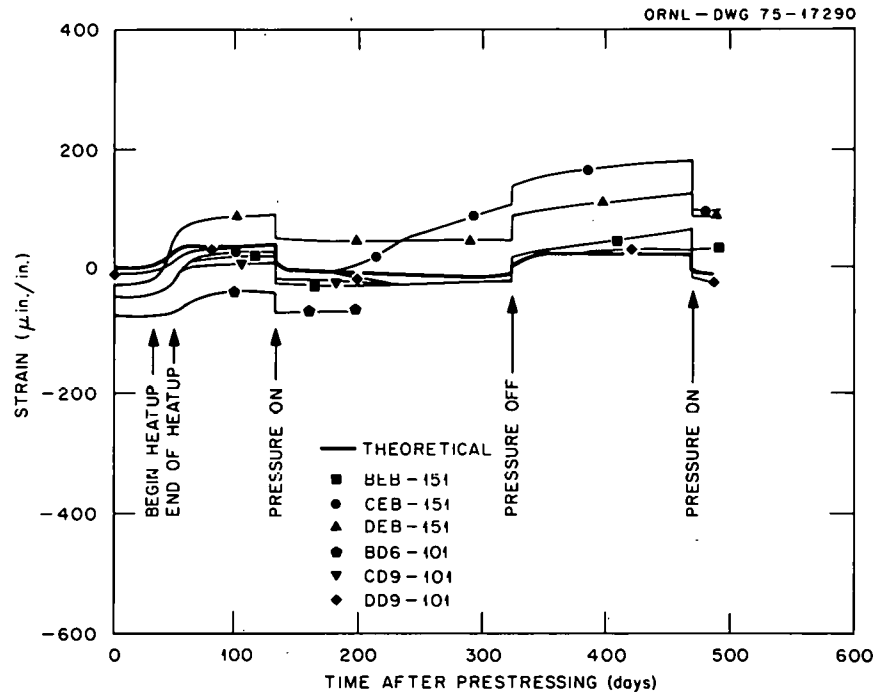
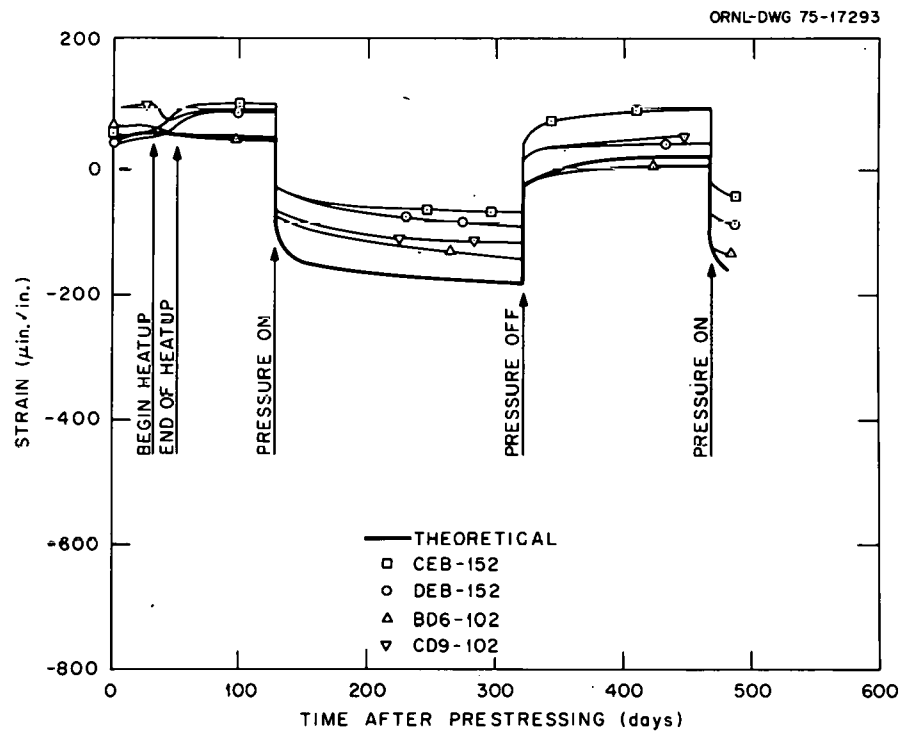Fig. 7.18. Axial strain 76.2 mm (3 in.) from inside wall.

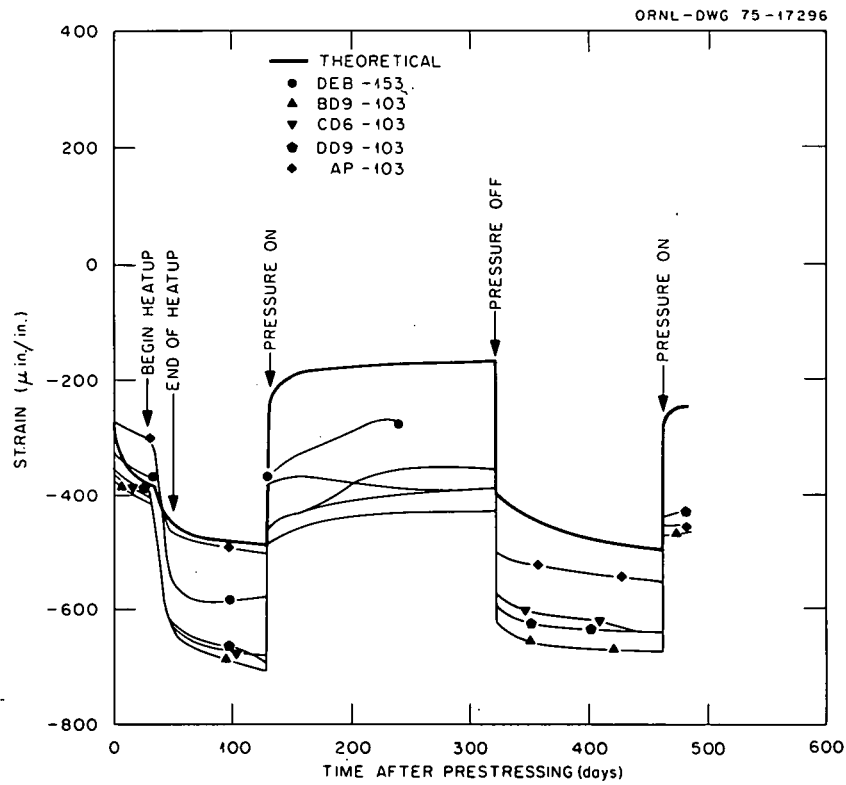Fig. 7.19. Radial strain 76.2 mm (3 in.) from inside wall.

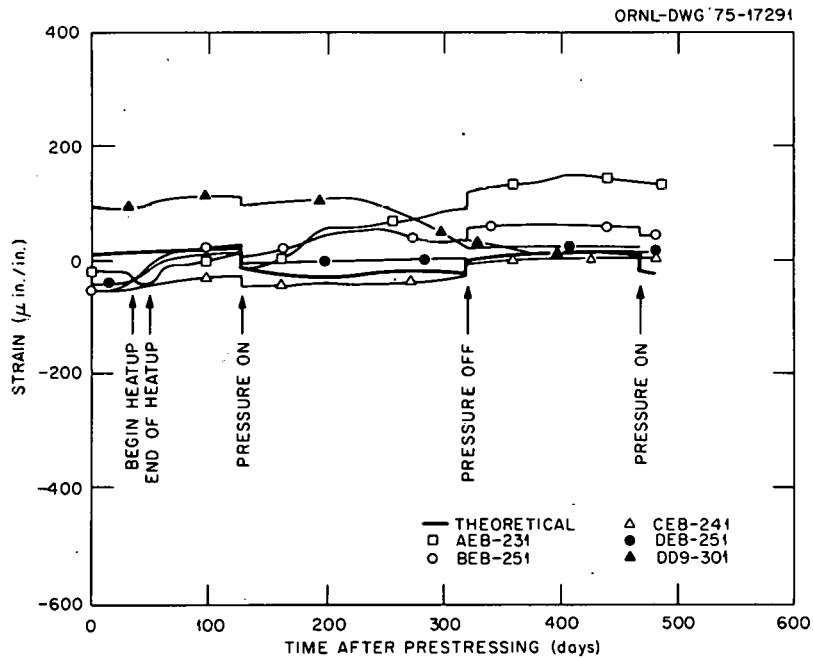Fig. 7.20. Circumferential strain 76.2 mm (3 in.) from inside wall.

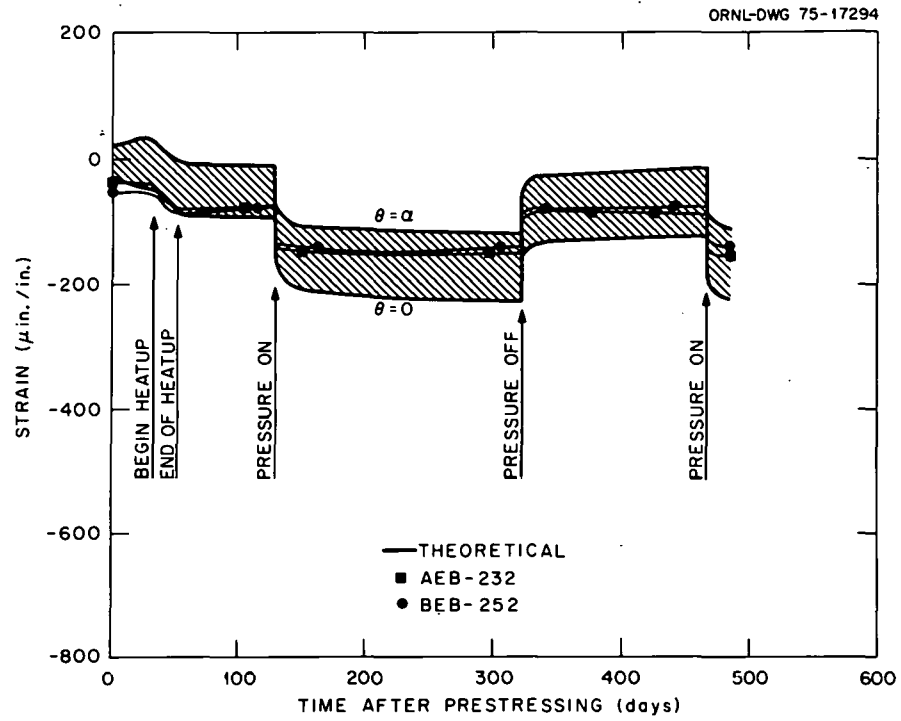Fig. 7.21. Axial strain at midthickness.

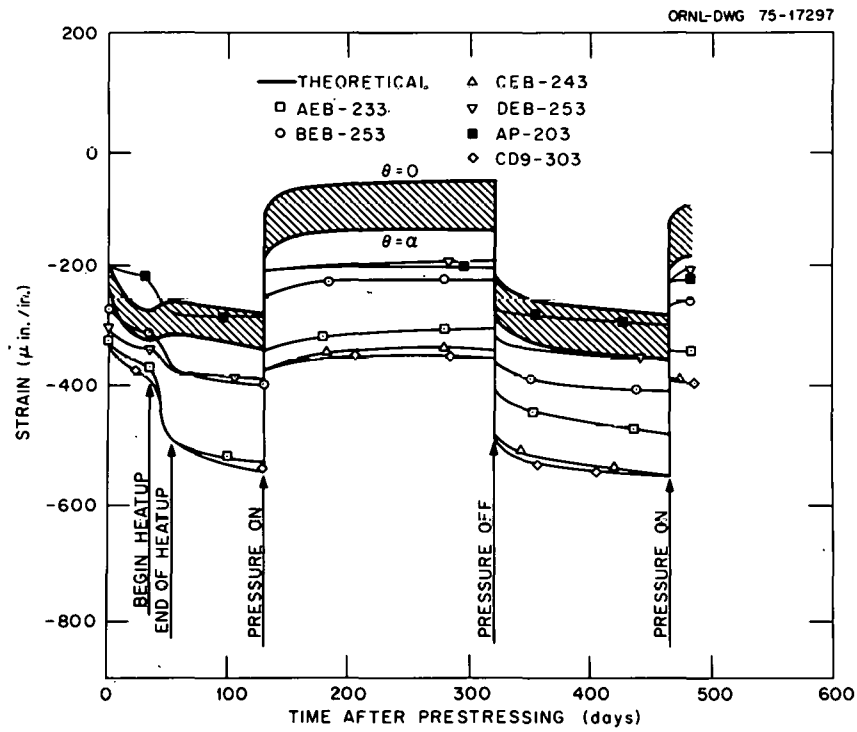Fig. 7.22. Radial strain at midthickness.

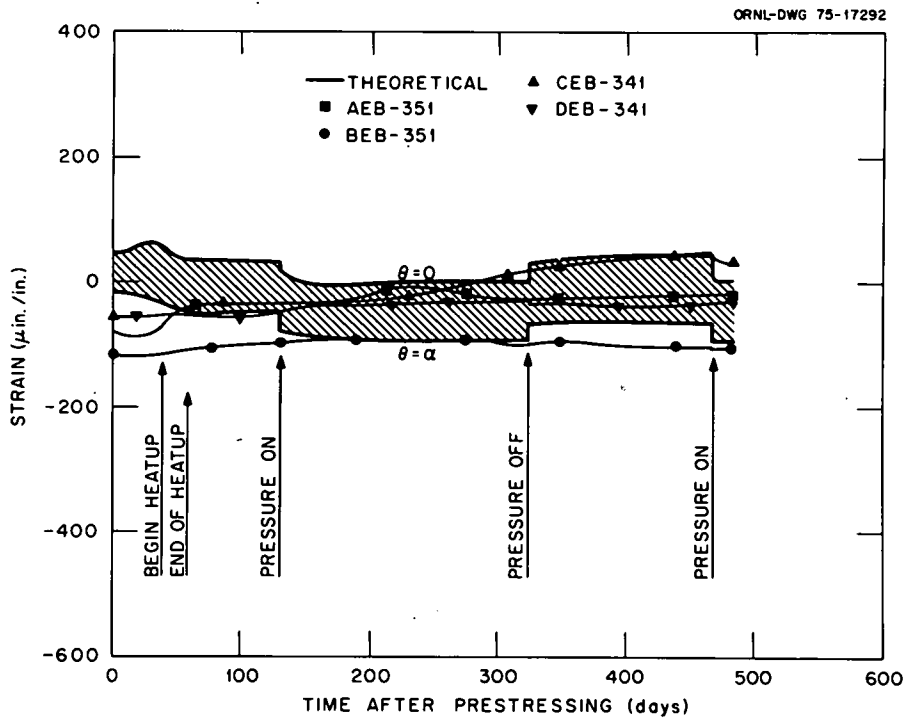Fig. 7.23. Circumferential strain at midthickness.

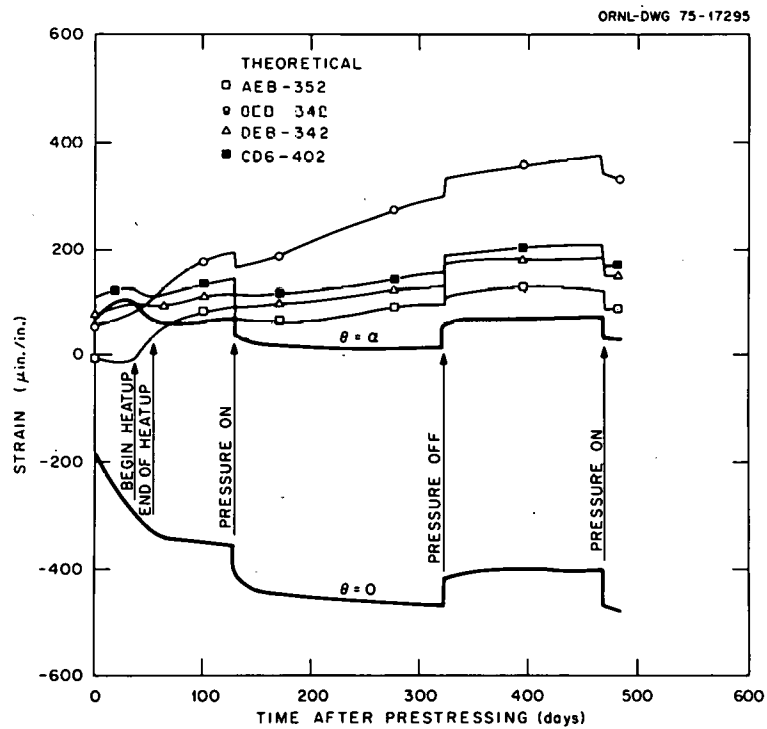Fig. 7.24. Axial strain 76.2 mm (3 in.) from outside wall.

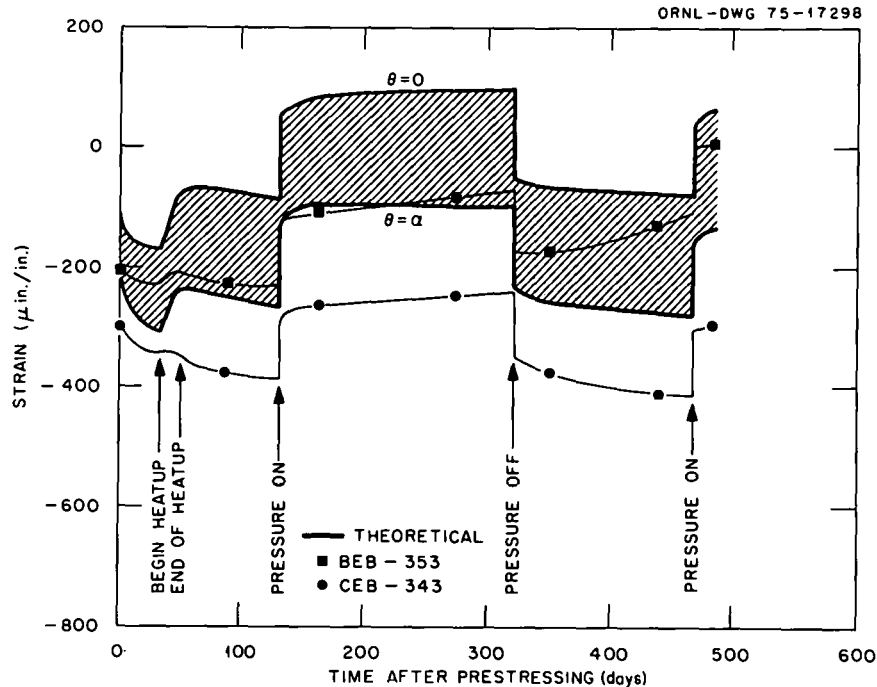Fig. 7.25. Radial strains 76.2 mm (3 in.) from outside wall.

Fig. 7.26. Circumferential strain 76.2 mm (3 in.) from outside wall.

and the boundary conditions imposed in the analysis. In addition, a constant axial stress was applied to simulate the effect of the axial prestressing. The results from this analysis for radial positions along a ray passing through the center of a pad ($\theta = 0$) and for radial positions midway between adjacent pads ($\theta = \alpha$) are shown on the Figs. 7.18 through 7.26. The effect of nonuniformity in loading is significant at the outside position (Figs. 7.24 through 7.26) but insignificant at the inside position (Figs. 7.18 through 7.20). Aside from properly accounting for the positive radial strains measured at the outside positions (Fig. 7.25) and better agreement for the axial results (Figs. 7.18, 7.21, and 7.24), the results from the plane and axisymmetric analyses are essentially the same. Thus, the differences in strain readings within each grouping cannot be explained by the nonuniformity of loading on the outside wall.

The close agreement between the results of the axisymmetric and the plane analyses and the fact that the analytical results lie within the distribution of strain results for most cases (one significant exception being the circumferential strains occurring during vessel heatup) lend a degree of credibility to the accuracy of the analysis. It appears from
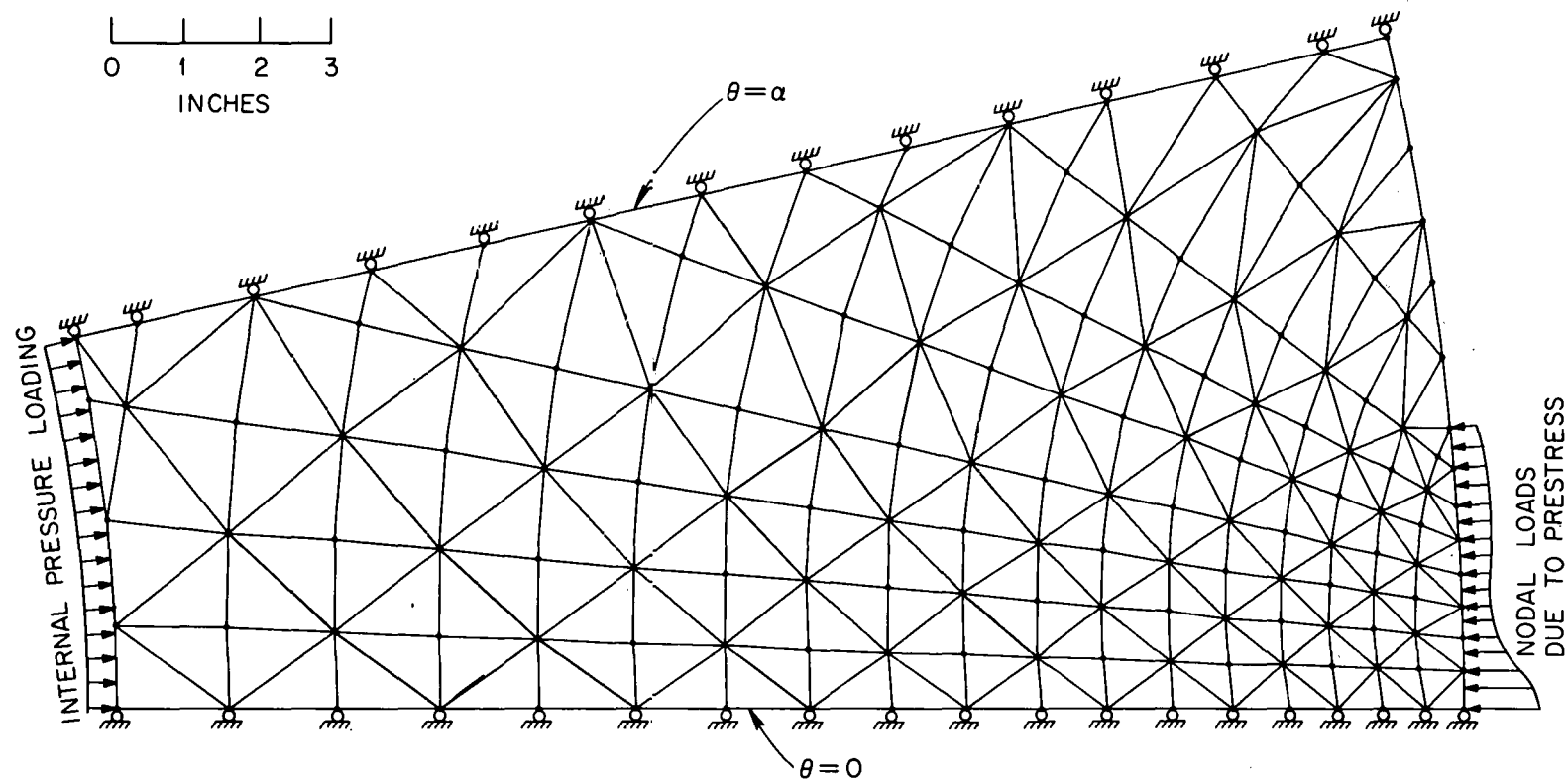
Fig. 7.27. Plane slice at midheight of thermal cylinder (1 in. =
25.4 mm).

the results given in Figs. 7.20 and 7.23 that the algorithm used for calculating creep strains[7] significantly underestimates the strains occurring during vessel heatup. The creep rate of concrete is known to be approximately proportional to the stress and strongly dependent on the temperature; consequently, the effect of errors in the creep calculations will be most pronounced for the higher stress components at locations having the greatest temperature change, that is, for the circumferential strains at the inside and middle locations (Figs. 7.20 and 7.23). It should be noted that if the observed disagreement between calculated and experimental strains during heatup had been due to an incorrect value for the coefficient of thermal expansion, an equal error would have been produced in the axial and radial strains at these locations, but such an error is not evident (Figs. 7.18, 7.19, and 7.21). The axial and radial stresses at these locations are very low; thus, the corresponding creep strains are small, and even a relatively large percentage error in their calculated values will not be significant. It also should be noted that if the analytical results were corrected for the discrepancy during heatup, close agreement between the analytical and experimental results would be obtained for the remaining portions of the test.

To ensure that the discrepancy during heatup was not the result of incorrect coding of the creep algorithm, the algorithm was independently recoded. There was very little difference in the results from the two independent codings, indicating that the error is fundamental to the algorithm and not the result of improper coding. Since the code reproduced the specified isothermal creep curves and the calculated creep during isothermal conditions seemed to agree with the corresponding experimental results for the thermal cylinder, the probable source of error is in the mathematical generalization of the isothermal creep data to the thermal transient case. Although the algorithm implemented in the SAFE/CRACK code is widely used, the results of this study and other published results[11-13] indicate that it underestimates the accumulated creep strain during thermal transient conditions. The effect of this error would probably be less in an actual PCRV than in this test because the heatup is slower, occurs at a later concrete age, and in some cases occurrs after vessel pressurization and hence at lower stress levels.

8. CONCLUSIONS AND RECOMMENDATIONS

8.1 Conclusions

The objectives of the thermal cylinder model test were (1) to provide reliable data for evaluating the present capability of predicting the behavior of a PCRV both over its operating history and when subjected to off-design hot-spot heating; (2) to demonstrate structural behavior under design and off-design operating conditions; and (3) to evaluate the performance of instrumentation representative of the types used to monitor PCRVs. These objectives are closely related and cannot necessarily be evaluated separately, since one cannot assume *a priori* that the gages consistently and accurately monitored existing conditions or that the analysis was entirely correct. We have reached the following conclusions based upon consistent behavior of multiple gages, overall trends seen in analytical and experimental results, and findings of postmortem examinations.

With regard to prestress loadings, good agreement was seen between the applied hydraulic ram loadings and the final loads transferred to the tendons as indicated by the load transducers (Fig. 6.21). Good agreement was also seen between load cell readings and strains measured by the functioning gages attached to individual tendon wires (Fig. 6.20). The axial loadings remained stable until the onset of sudden corrosion failure of individual wires after about 250 days.

Conventional load cells could not be used with the circumferential tendons owing to their unique design; however, strain gages were attached to individual wires of each strand. During posttensioning, these gages indicated strain reversals caused by the initial straightening of the tendons; however, once they were straightened, subsequent readings showed good agreement with applied hydraulic ram loading steps. Thus, the absolute strain values indicated in Fig. 6.22 do not accurately reflect the total applied loading. However, this figure does show that that tendons did not display any significant relaxation during the various applied sustained loadings.

Although the applied axial loadings were affected by tendon corrosion, these loadings were, by design, relatively small when compared with the

applied circumferential tendon loadings (161 kN vs 725.5 kN). Consequently, the observed changes in axial tendon loadings were difficult to detect on the adjacent axial concrete embedment gages.

Comparisons of experimental strain gage data with time-dependent analysis predictions obtained using the SAFE/CRACK finite-element computer program indicated generally good agreement for the normal vessel operating period, although the analysis tended to underestimate heating strains and overestimate mechanical loading strains. The embedded stress cells behaved inconsistently at times; but, generally, they indicated mechanically induced stresses that were lower than the respective calculated values. Significant disagreement was seen between experimental and calculated results for the hot-spot test, thereby indicating the present inability of the analysis to consider abrupt temperature changes.

The postmortem analytical study tended to verify the accuracy of the viscoelastic finite-element algorithm in the SAFE/CRACK code; however, there appears to be a deficiency in the creep algorithm for the thermal transient case; namely, the code predicted cracking where none existed during both the normal operation simulation and the off-design hot-spot heating.

An examination of the sectioned model revealed no cracking, distress, or structural failures that could be attributed to either the simulated operational or hot-spot heating periods. This was true for both the concrete and the steel liner. The only detrimental effect of the hot-spot heating was a significant reduction in the strength of the concrete in a restricted region immediately adjacent to the hot-spot heaters. Readings made using a neutron and gamma-ray backscattering moisture probe showed little if any migration of moisture in the concrete cross section.

The problems encountered with concrete embedment instrumentation were due primarily to a mismatch in gages and readout instrumentation and to insufficient gage evaluation and calibration studies being conducted prior to the experiment. For example, the malfunctioning of the wound-wire resistance gages should have been detected and possibly corrected. Although a large number of the concrete embedment gages provided useful data, it was necessary in many cases to make personal judgments as to whether or not a gage was functioning correctly. Because of the high cost of installing

and monitoring gages of these types in an operating PCRV, it is most important that the instrumentation be both dependable and accurate. It is apparent from this experiment that further work is needed to develop highly reliable instrumentation and techniques for installing these gages that preclude damage during construction.

Since concrete behaves in a viscoelastic manner when subjected to sustained loadings and elevated temperature, it is important to have a means for measuring stress directly in the concrete. Such devices remain to be perfected, although this experiment shows they offer some promise.

The problem of tendon corrosion experienced during the thermal cylinder experiment is probably unique because of the particular combination of materials employed. A similar set of conditions should not occur in a prototype PCRV under normal design conditions. However, epoxy has been used on occasion in the past to repair concrete "honeycombing" in prestressing anchorage regions; and if this practice is employed, it would appear that care should be exercised to ensure that the tendon and tendon duct are fully protected.

8.2 Recommendations

The thermal cylinder experiment was designed to bring together the various tasks of the original ORNL Prestressed Concrete Reactor Vessel Research and Development Program to culminate in a demonstration of capability to predict the time-dependent behavior of a PCRV during its operating lifetime. The data from this experiment comprise a most important part of the verification of PCRV analysis methods and provide an understanding of the behavior of this type of vessel. Although a great deal of useful information was obtained from the experiment, it was undertaken as a best-effort project based on a restricted time schedule and budget and using instrumentation and calibration provided primarily by the manufacturers. Thus, the following recommendations are based on our experiences in conducting the experiment under the aforementioned constraints.

1. A basic study should be conducted to accurately determine calibration factors and evaluate sealing of all concrete embedment instrumentation.

2. Existing commercial stress cells should be evaluated and, if necessary, an improved stress cell capable of operating at least under potential hot-spot temperatures should be perfected.

3. Present finite-element methods should be refined so as to include the capability of accurately predicting crack initiation and propagation in regions where complex states of stress exist.

4. Further studies should be made to determine the accuracy of concrete creep algorithms for thermal transient cases and, if necessary, to develop improved algorithms.

5. A program using much simpler structural models should be undertaken to provide a means for evaluating candidate concrete embedment gages in order to determine their capability to accurately monitor structural response and also for evaluating candidate methods of analysis.

6. Finally, once satisfactory instrumentation has been perfected and the previously listed improvements in analysis methods have been developed, a second thermal cylinder model should be tested to provide what should be the final and ultimate verification of PCRV analysis methods.

REFERENCES

1. G. D. Whitman, *Prestressed Concrete Reactor Vessel Research and Development Program Summary*, ORNL-TM-2179 (Apr. 1, 1968).

2. J. M. Corum and G. C. Robinson, Jr., "Thermal Cylinder Test to Simulate Behavior of Cylindrical Portion of a Prestressed Concrete Vessel," *GCR Prgram Semiannu. Prog. Rep. Mar. 31, 1969*, ORNL-4424, pp. 225–39.

3. J. M. Corum, J. P. Callahan, and M. Richardson, "PCRV Thermal Cylinder Test," *Gas-Cooled Reactor and Thorium Utilization Program Semiannu. Prog. Rep. Sept. 30, 1970*, ORNL-4637, pp. 70–71.

4. B. Bresler, M. Polivka, and V. Bertero, "Concrete Strength Properties as a Function of Temperature," *GCR Program Semiannu. Prog. Rep. Mar. 31, 1969*, ORNL-4424, pp. 164–88.

5. Y. R. Rashid, *Nonlinear Quasi-Static Analyses of Two-Dimensional Concrete Structures*, GA-9994 (Mar. 24, 1970).

6. T. W. Kennedy, *An Evaluation and Summary of a Study of the Long-Term Multiaxial Creep Behavior of Concrete*, ORNL-TM-5300 (December 1975).

7. Y. R. Rashid, "Nonlinear Analysis of Two-Dimensional Problems in Concrete Creep," *Trans. ASME, Ser. E, J. Appl. Mech.* 94, 475–82 (1972).

8. R. F. Denkins, *GCR Program Semiannu. Prog. Rep. Mar. 31, 1969*, ORNL-4424, pp. 127–38.

9. A. M. Neville, *Properties of Concrete*, Wiley, New York, 1963.

10. N. W. Hansen and O. A. Kurvits, "Instrumentation for Structural Testing," *J. PCA Res. Dev. Lab.* 7(2), 33 (May 1965).

11. D. Carlton, J. R. Smith, and G. N. Bellwood, "Prestressing and Proof Pressure Testing of the Wylfa Prestressed Concrete Pressure Vessels and Comparison of Measured Data with Predicted Performance," in *Proceedings of the First International Conference on Structural Mechanics in Reactor Technology, Berlin, 1971.*

12. F. Bremer, "Practice with Model Techniques," *Conference on Model Techniques for Prestressed Concrete Pressure Vessels*, The British Nuclear Society, London, 1969.

13. J. R. Smith, "Problems in Assessing the Correlation Between the Observed and Predicted Behavior of Models," *Conference on Model Techniques for Prestressed Concrete Pressure Vessels*, The British Nuclear Society, London, 1969.

Internal Distribution

1.	S. J. Ball	40.	R. E. MacPherson
2.	Seymour Baron	41.	A. P. Malinauskas
3.	D. E. Bartine	42.	W. R. Martin
4.	A. L. Boch	43.	W. J. McAfee
5-16.	J. P. Callahan	44.	J. G. Merkle
17.	D. A. Canonico	45.	R. K. Nanstad
18.	J. A. Clinard	46.	D. J. Naus
19.	J. A. Conlin	47.	K. J. Notz
20.	J. H. Coobs	48.	C. B. Oland
21.	W. E. Cooper	49.	H. Postma
22.	F. L. Culler	50.	G. C. Robinson
23.	J. M. Corum	51.	J. P. Sanders
24.	F. C. David	52.	M. R. Sheldon
25.	J. R. DiStefano	53.	G. M. Slaughter
26.	W. G. Dodge	54.	G. C. Smith
27.	W. P. Eatherly	55.	J. E. Smith
28.	D. N. Fanning	56.	M. Tobias
29.	G. G. Fee	57.	D. B. Trauger
30.	Uri Gat	58.	J. R. Weir, Jr.
31.	M. J. Goglia	59.	G. D. Whitman
32.	A. G. Grindell	60.	R. P. Wichner
33.	W. L. Greenstreet	61.	W. J. Wilcox
34.	R. C. Gwaltney	62.	ORNL Patent Office
35.	J. F. Harvey	63-64.	Central Research Library
36.	F. J. Homan	65.	Document Reference Section
37.	P. R. Kasten	66-70.	Laboratory Records Department
38.	M. Levenson	71.	Laboratory Records (RC)
39.	A. L. Lotts		

Subcontractors

72. D. W. Goodpasture, Civil Engineering Department, University of Tennessee, Knoxville, Tenn. 37916
73. W. C. Schnobrich, Civil Engineering Department, University of Illinois, Urbana, Ill. 61801
74. M. A. Sozen, Civil Engineering Department, University of Illinois, Urbana, Ill. 61801
75. R. H. Gallagher, Civil Engineering Department, Cornell University, Ithica, N.Y. 14850

External Distribution

76-77. Director, Division of Nuclear Research and Application, Energy
Research and Development Administration, Washington, D.C. 20545
78. Director, Reactor Division, ERDA, ORO
79. Research and Technical Support Division, ERDA, ORO
80-256. For distribution as shown in TID-4500 under category UC-77, Gas-
Cooled Reactor Technology